Chapter 7

CHARM AND BEAUTY IN MEDIA

Conveners: D. Kharzeev, M. P. Lombardo, C. Lourenço, M. Rosati, H. Satz

Authors: S. Datta, O. Kaczmarek, F. Karsch, D. Kharzeev, S. R. Klein, V. Laporta, M. P. Lombardo, C. Lourenço, L. Maiani, P. Petreczky, F. Piccinini, A. D. Polosa, L. Ramello, R. Rapp, V. Riquer, M. Rosati, H. Satz, E. Scomparin, R. Vogt, F. Zantow

1 INTRODUCTION[1]

Quarkonium in media is a topic which is central to the ultrarelativistic heavy ion program. In recent years this subject has been among the focal points of discussion at meetings such as "Quark Matter". ("The Quark Matter" series is traditionally the main forum of the high energy heavy ion community). Indeed, in these collisions — "little bangs" — one hopes to recreate matter as it was at the very beginning of the universe: a hot system with deconfined quarks and gluons and no chiral symmetry breaking.

This fascinating possibility calls for a number of theoretical and phenomenological studies. The QCD phase diagram and the mechanisms of chiral symmetry restoration, screening, and deconfinement at high temperature and baryon density need to be understood. A theory of the initial conditions must be developed and the equilibration of the plasma, if any, must be assessed in real experiments. It is also necessary to identify the thermodynamical region which is being explored and to study nonequilibrium effects. Finally, observables must be defined which provide physical signatures in real experiments.

Quarkonium plays a very important role in these phenomena. Indeed, quarkonium suppression was long ago suggested as a signal of deconfinement [1]. Due to their small size, quarkonia can, in principle, survive the deconfinement phase transition. However, because of colour screening, no bound state can exist at temperatures $T > T_D$ when the screening radius, $1/\mu_D(T)$, becomes smaller than the typical bound-state size [1]. Later it was realized that dramatic changes in the gluon momentum distributions at the deconfinement phase transition result in a sharp increase in the quarkonium dissociation rates [2–4]. Both the magnitude [5] and the energy dependence [6] of charmonium dissociation by gluons result in significant suppression of the $c\bar{c}$ states even for $T < T_D$ but higher than the deconfinement transition temperature, T_c. Moreover, close to T_D the thermal activation mechanism is expected to dominate [7, 8]. The relative importance of gluon dissociation and thermal activation is governed by the ratio of the quarkonium binding energy $\epsilon(T)$ and the temperature T, $X(T) \equiv \epsilon(T)/T$ [9]. At $X(T) \ll 1$ thermal activation dominates while for $X(T) \gg 1$ the dominant mechanism is "ionization" by gluons.

Dissociation due to colour screening was studied using potential models with different parameterizations of the heavy quark potential [10–13] to determine T_D. All these studies predicted that excited charmonium states (χ_c, ψ') will essentially dissolve at T_c while the ground state J/ψ will dissociate at 1.1–1.3 T_c. Some potential models also predicted a strong change in the binding energy, see e.g., Ref. [12]. Recently, charmonium properties were investigated using lattice calculations [14, 15] which indicate that the ground states exist with essentially unchanged properties at temperatures around $1.5T_c$.

Lattice investigations suggest that at low temperatures, $T < 1.5T_c$, screening is not efficient and therefore gluon dissociation may be the appropriate source of quarkonium suppression. One should also keep in mind that non-equilibrium effects in the very early stages of a heavy-ion collision, when the energy density is highest, should be considered for quarkonium suppression. Not much is known about

---

[1] Authors: D. Kharzeev, M. P. Lombardo, C. Lourenço, M. Rosati, H. Satz

these effects. However, they may be an even more important source of quarkonium suppression than a thermalized system, see e.g., Ref. [16].

To use heavy quarkonium as an effective probe of the state of matter in QCD, we should also have good theoretical control over the scattering amplitudes in a hadronic gas.

While addressing the issues outlined above, we will face questions familiar to the heavy quark and the thermodynamics communities. To fully understand the behaviour of quarkonium in media, these two communities should communicate and interact. For further background material and a review of the results as of Summer 2003, see Ref. [17].

The behavior of quarkonium in cold nuclear matter can be used to better understand the nuclear medium. For example, quarkonium can also be used to study nuclear parton distributions, particularly that of the gluon. In addition to hadroproduction studies, quarkonium photoproduction is directly sensitive to the nuclear gluon distribution.

2 QCD IN MEDIA, AND THE LATTICE APPROACH[2]

This section introduces strong interactions 'in media' using the field theory of QCD as the basic theoretical framework. We build on work presented in the 'Introduction to QCD' and 'General Tools' sections of this Yellow Report and briefly discuss basic aspects which are not covered there but are used in the rest of this Chapter.

We first discuss the phases of QCD, i.e., the fate of chiral symmetry and confinement at high temperature and density. We then introduce lattice thermodynamics, the main theoretical tool for studying equilibrium characteristics of the phase diagram. In doing so, deconfinement, screening, and spectral modifications, which are discussed at length later, will be briefly touched upon.

Our main interest is in heavy ion colliders experiments where the baryon density is relatively small. Lattice high density calculations are far less mature then those at high temperature. In particular, no results for heavy quarks have been obtained in the high density regime. Hence we will focus on the physics of QCD at high temperature.

Let us first consider the fate of confinement at high temperature. A sketchy view of the screening mechanism, already at work at $T = 0$, is the recombination of a (heavy) quark and antiquark with pairs generated by the vacuum, $Q\overline{Q} \to \overline{q}Q + q\overline{Q}$. At high temperature it becomes easier to produce light $q\overline{q}$ pairs from the vacuum. Hence it is easier to 'break' the colour string between a (heavy) quark, Q, and antiquark $\overline{Q}$. In other words, we expect colour screening to increase (sharply) at a phase boundary, eventually leading to quark and gluon liberation, the quark gluon plasma. Lattice simulations indicate that enhanced screening occurs at about $T \sim 200$ MeV, in a range accessible to collider experiments (see e.g., [18] for a recent review).

Consider now the fate of chiral symmetry at high temperature obtained by following the behaviour of the chiral condensate $\langle\overline{\psi}\psi\rangle$. One picture of the high T QCD transition can be drawn by using the ferromagnetic analogy of the chiral transition where $\overline{\psi}\psi$ can be thought of as a spin field taking values in real space, but oriented in the chiral sphere. Chiral symmetry breaking occurs when $\langle\overline{\psi}\psi\rangle \neq 0$, corresponding to the ordered phase. By increasing T, disorder increases, and $\langle\overline{\psi}\psi\rangle \to 0$, restoring chiral symmetry. Lattice simulations suggest that chiral symmetry restoration and enhanced screening happen at the same temperature within the numerical accuracy.

These seemingly simple pictures of chiral symmetry restoration and deconfinement at high temperature are complicated by a number of considerations. A finite quark mass breaks the chiral symmetry of the Lagrangian while screening can be rigorously related to deconfinement only at infinite quark mass. Rigorously speaking, the two mechanisms we are concerned with are defined in two opposite limits: zero

---

[2] Author: M. P. Lombardo

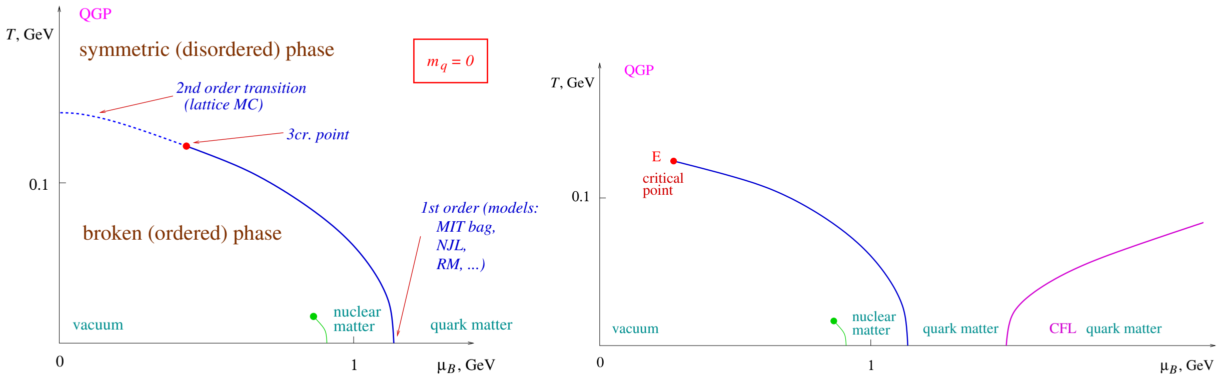

Fig. 7.1: The phase diagram of QCD for two massless flavours (left) and what is expected for realistic values of the quark masses (right). From M. Stephanov [19].

mass for chiral symmetry and infinite mass for confinement. For two (massless) flavours the transition seems to be of second order while the transition with three (massless) flavour turns out to be first order. We have to find out how the two flavour picture morphs with the three flavour one. In addition, it may well be that the $U_A(1)$ symmetry, broken at zero temperature, is effectively restored at high temperature, further complicating the patterns of chiral symmetry. It is also worth mentioning in this brief introduction that, even if the string 'breaks', bound states might well survive, giving rise to complicated, nonperturbative dynamics above the critical temperature, characterising the strongly-interacting quark gluon plasma. In addition to these conceptual difficulties, there are calculational problems since the phenomena we are concerned with are well outside the reach of perturbative calculations.

One goal of our subgroup is to understand how all of these phenomena affect the heavy quark spectrum when the phase boundary in Fig. 7.1 is crossed. Here, we show the phase diagram of QCD in the temperature and chemical potential plane. The diagrams for 'light QCD' (two massless quarks), and for realistic values of the u, d and s masses, were built using symmetry arguments and model calculations. The informal discussion presented here should already suggest that the physics of heavy quark bound states in media is driven by a rich and complex admixture of chiral symmetry restoration and enhanced screening, requiring both lattice and analytic studies. Recent advances will be presented in the next sections.

As a last introductory remark, we review a few basic facts about finite temperature field theory [20] and its formulation on the lattice [21]. In equilibrium field theory, the grand canonical partition function, $Z(V, T, \mu)$ completely determines the thermodynamic state of a system according to:

$$P = T\frac{\partial \ln Z}{\partial V} \qquad (7.1)$$

$$N = T\frac{\partial \ln Z}{\partial \mu} \qquad (7.2)$$

$$S = \frac{\partial [T \ln Z]}{\partial T} \qquad (7.3)$$

$$E = -PV + TS + \mu N \qquad (7.4)$$

while the physical observables $\langle O \rangle$ can be computed as

$$\langle O \rangle = \frac{\mathrm{Tr}(O\hat{\rho})}{Z} \ . \qquad (7.5)$$

In short, the problem is to represent Z for QCD at finite temperature and design a calculational scheme to describe it.

The partition function, Z, is the trace of the density matrix of the system, $\hat{\rho}$, so that

$$\begin{aligned} Z &= \mathrm{Tr}\,\hat{\rho} && (7.6)\\ \hat{\rho} &= \exp[(-H - \mu\hat{N})/T] && (7.7) \end{aligned}$$

where H is the Hamiltonian, T is the temperature and $\hat{N}$ is any conserved number operator. Introducing the integral, $S(\phi, \psi)$, of the Lagrangian density where Te is the temporal extent in Euclidean space,

$$S(\phi, \psi) = \int_0^{Te} dt \int d^3x \mathcal{L}(\phi, \psi) \ , \tag{7.8}$$

and Z is defined as

$$Z = \int d\phi\, d\psi\ \exp[-S(\phi, \psi)] \ . \tag{7.9}$$

Comparing the path integral representation of the partition function, Eq. (7.9), with the statistical mechanics representation, Eq. (7.7), we can identify the finite temporal extent of the Euclidean space, Te, with the reciprocal of the system temperature [20]. The only missing ingredients are the boundary conditions for the fields in Eq. (7.9) which follow from the (anti)commuting properties of the (fermi)bose fields, implying

$$\hat{\phi}(\vec{x}, 0) = \hat{\phi}(\vec{x}, \beta) \tag{7.10}$$

for bosons and

$$\hat{\psi}(\vec{x}, 0) = -\hat{\psi}(\vec{x}, \beta) \tag{7.11}$$

for fermions. Fermions and bosons obey antiperiodic and periodic boundary conditions, respectively, in the time direction.

Finite temperature lattice field theory is then straightforward since temperature comes for free. Because the lattice has a finite extent, $N_t a$, temperature is given by $T = 1/N_t a$. The discretization procedure is the same as at zero temperature and most of the standard lattice techniques, reviewed in the introductory Sections above, carry over to finite temperature. Such a field theoretic approach to finite temperature QCD allows us to put thermodynamics and spectral calculations on the same footing.

3 QCD AT FINITE TEMPERATURE: COLOUR SCREENING AND QUARKONIUM SUPPRESSION[3]

On quite general grounds, it is expected and, in fact, confirmed by lattice simulations that strongly interacting matter undergoes a transition to quark gluon plasma at high temperature and density. One of the most prominent properties of this state of matter is the screening of colour forces between static quarks. The associated screening length (often referred to as the chromoelectric or non-Abelian Debye length) is inversely proportional to the temperature.

Heavy quarkonia, unlike usual (light) hadrons, may exist in the quark gluon plasma due to their relative small sizes. However, above some temperature the screening radius eventually becomes smaller than the typical quarkonia radii, leading to their dissolution. This physical picture was used by Matsui and Satz to propose quarkonium suppression as a signal for deconfinement in heavy ion collisions [1]. In fact, it was found that the J/ψ dissolves above but close to the deconfinement temperature T_c. Estimates of the dissociation temperature based on the screening picture have some shortcomings. It is not clear to what extent many body effects present in the strongly coupled quark gluon plasma can be approximated by modification of the interaction between the two heavy quarks. Unfortunately, it is also not trivial to define the screening radius.

Although a detailed understanding of screening phenomena at large distances is still missing, it is evident that in this regime the temperature is the dominant scale and consequently will control the

---

[3] Section coordinator: P. Petreczky; Authors: S. Datta, O. Kaczmarek, D. Kharzeev, F. Karsch, M. P. Lombardo, P. Petreczky, H. Satz, F. Zantow

running of the QCD coupling, i.e., $g \simeq g(T)$ for $(rT \gg 1,\, T \gg T_c)^4$. However, at short distances, $r \cdot \max(T, T_c) \ll 1$, hard processes dominate the physics of the quark gluon plasma even at high temperature and it is expected that a scale appropriate for this short distance regime will control the running of the QCD coupling, i.e., $g \simeq g(r)$. The interplay between short and large distance length scales plays a crucial role for a quantitative understanding of hard as well as soft processes in dense matter. It will, for instance, determine the range of applicability of perturbative calculations for thermal dilepton rates or the production of jets as well as the analysis of processes that can lead to thermalization of the dense matter produced in heavy ion collisions. Moreover, the short and intermediate distance regime also is most relevant for the discussion of in-medium modifications of heavy quark bound states which are sensitive to thermal modifications of the heavy quark potential as well as the role of quasi-particle excitations in the quark–gluon plasma.

Another powerful tool to study the dissolution of quarkonia states in the plasma is the corresponding meson spectral functions.

The first subsection will be devoted to a general discussion of screening in hot matter and the running coupling and its observable implications. Next, we discuss direct lattice calculations of the spectral functions. These simulations grow extremely expensive at larger quark mass, which require a fine spacing, and b quark physics seems to be out of reach within this approach. It is then natural to consider NRQCD thermodynamics, a new theoretical tool. We will comment on this new possibility at the end.

3.1 Colour screening and running coupling

The simplest way to understand the screening phenomenon is to consider the potential between an arbitrarily heavy (but not static) quark and antiquark in perturbation theory. At zero temperature the potential can be calculated from the Born heavy quark–antiquark scattering amplitude in the non-relativistic limit. In the Born approximation, the potential in momentum space is just the scattering amplitude which, at lowest order in the non-relativistic expansion, is

$$-\frac{4}{3} g^2 D_{00}(k) \tag{7.12}$$

where $D_{00}(k)$ is the propagator in the Coulomb gauge [22]. Using the leading order perturbative form, $D_{00}(k) = 1/k^2$, we recover the Coulomb potential in coordinate space.

Now consider the high temperature plasma phase. Assuming that the heavy quark and antiquark are well defined quasi-particles, the scattering amplitude is

$$-\frac{4}{3} g^2 \frac{1}{k^2 + \Pi_{00}(k)} \, , \tag{7.13}$$

where $\Pi_{00}(k)$ is the medium induced gluon self-energy. At leading order and small momenta, $\Pi_{00}(k)$ is gauge independent and leads to a non-zero mass term in the gluon propagator, $m_D^2 \equiv \lim_{k \to 0} \Pi_{00}(k) = \frac{1}{3} g^2 T^2 (N + \frac{1}{3} N_f)$. Thus we obtain the screened Coulomb potential

$$-\frac{4}{3} \frac{g^2}{4\pi r} \exp(-m_D r) \tag{7.14}$$

as a function of distance r.

Another way to discuss colour screening which is also suitable for nonperturbative (lattice) study, is to consider the partition function in the presence of a static quark–antiquark pair normalized by the

---

[4] We use the deconfinement temperature T_c as a characteristic energy scale rather than a more conventionally used Λ-parameter.

partition function $Z(T)$ of the system without static charges which can be written as [23]

$$\begin{aligned}\frac{Z_{q\bar{q}}(r,T)}{Z(T)} &= \frac{1}{Z(T)}\int DA_\mu D\overline{\psi}D\psi e^{-\int_0^{1/T}d\tau\int d^3x\mathcal{L}_{QCD}(\tau,\vec{x})}W(\vec{r})W^\dagger(0) \\ &= \langle W(\vec{r})W^\dagger(0)\rangle\end{aligned}$$

where the Wilson line or Polyakov loop is defined as

$$W(\vec{x}) = Pe^{ig\int_0^{1/T}d\tau A_0(\tau,\vec{x})} \ .$$

The above partition function contains all colour orientations of the static $Q\overline{Q}$ pair. Using projection operators one can formally define the partition function for colour singlet (1), colour octet (8), and colour average (av) channels as [24, 25]

$$\frac{Z^{(1)}_{q\bar{q}}(r,T)}{Z(T)} = \frac{1}{3}\mathrm{Tr}\langle W(\vec{r})W^\dagger(0)\rangle \tag{7.15}$$

$$\frac{Z^{(8)}_{q\bar{q}}(r,T)}{Z(T)} = \frac{1}{8}\langle \mathrm{Tr}W(r)\mathrm{Tr}W^\dagger(0)\rangle - \frac{1}{24}\mathrm{Tr}\langle W(r)W^\dagger(0)\rangle \tag{7.16}$$

$$\frac{Z^{(\mathrm{av})}_{q\bar{q}}(r,T)}{Z(T)} = \frac{1}{9}\langle \mathrm{Tr}W(r)\mathrm{Tr}W^\dagger(0)\rangle \ . \tag{7.17}$$

Only the colour average partition function is manifestly gauge invariant. To define the singlet and octet partition functions one may replace the Wilson line by dressed gauge invariant Wilson lines [26] or one may fix the Coulomb gauge in Eq. (7.15). These two definitions were shown to be equivalent [26] (see also [27]). Having defined the partition function in the presence of a static quark–antiquark pair, the change in the free energy, F_i, the internal energy, V_i, and the entropy, S_i, of the static quark–antiquark pair relative to a system with no static charges are calculated as

$$F_i(r,T) = -T\ln\left(\frac{Z^{(i)}_{q\bar{q}}(r,T)}{Z(T)}\right) = V_i(r,T) - TS_i(r,T) \tag{7.18}$$

$$V_i(r,T) = T^2\frac{\partial}{\partial T}\ln\left(\frac{Z^{(i)}_{q\bar{q}}(r,T)}{Z(T)}\right) = -T^2\frac{\partial[F_i(r,T)/T]}{\partial T} \tag{7.19}$$

$$S_i(r,T) = -\frac{\partial F_i(r,T)}{\partial T} \quad i = 1, 8, \mathrm{av} \ . \tag{7.20}$$

We concentrate on the colour singlet case in the following. In leading order perturbation theory, F_1 is dominated by 1-gluon exchange and is therefore also given by Eq. (7.14) [23]. For this reason the free energies were (mis)interpreted as potentials. However, F_1 generally contains an r-dependent entropy contribution which starts at order g^3 in perturbation theory so that $V_1 = F_1$ only at leading order.

Recently the colour singlet free and internal energies of static quark antiquark pair have been studied in lattice simulations of SU(3) gauge theory [28, 29]. Below the deconfinement transition temperature, $T < T_c$, $F_1(r,T)$ shows a linear rise with r, as expected in the confined phase. In the plasma phase ($T > T_c$) both $F_1(r,T)$ and $V_1(r,T)$ approach a finite value for $r \to \infty$, indicating the presence of colour screening. The numerical results for F_1 and V_1 in the plasma phase are shown in Fig. 7.2. For small distances, $r < 0.2$ fm, and temperatures close to T_c both F_1 and V_1 coincide with the $T = 0$ potential, as expected since, at small distances, medium effects are negligible and the free energy of the static $Q\overline{Q}$ pair is simply the interaction energy, i.e., the heavy quark potential at zero temperature. In general, however, the free energy and the internal energy show quite different T- and r-dependences.

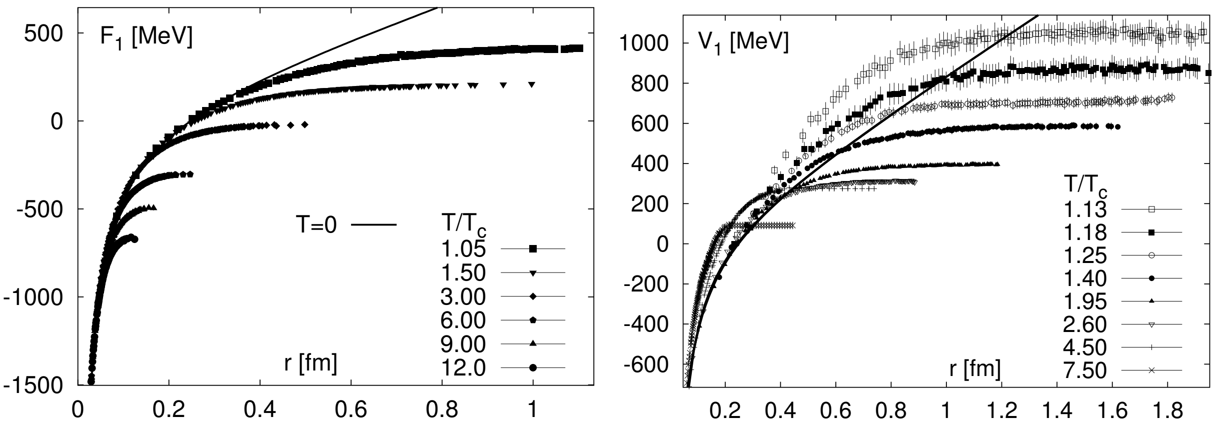

Fig. 7.2: The free energy (left) and the internal energy (right) of static $Q\overline{Q}$ pair in the plasma phase.

The perturbative short and large distance relations for the singlet free energy have recently been used to define a running coupling at finite temperature [30],

$$\alpha_{\rm qq}(r,T) = \frac{3r^2}{4}\frac{{\rm d}F_1(r,T)}{{\rm d}r} \quad . \tag{7.21}$$

In general, however, the definition of a running coupling in QCD is not unique beyond the validity range of 2-loop perturbation theory; aside from the scheme dependence of higher order coefficients in the QCD β-functions it will strongly depend on non-perturbative contributions to the observable used for its definition.

We compare the finite temperature results (symbols) to calculations performed at zero temperature (lines) [31–34] in Fig. 7.3. These numerical results on $\alpha_{\rm qq}$ at distances smaller than 0.1 fm cover also distances substantially smaller than those analyzed so far at $T = 0$. They clearly show the running of the coupling with the dominant length scale r also in the QCD plasma phase. For temperatures below $3T_c$ one finds that $\alpha_{\rm qq}$ agrees with the zero temperature perturbative result in its entire regime of validity, i.e., for $r \lesssim 0.1$ fm. At these temperatures thermal effects only become visible at larger distances and lead, as expected, to a decrease of the coupling relative to its zero temperature value; at distances larger than $r \simeq 0.1$ fm non-perturbative effects clearly dominate the properties of $\alpha_{\rm qq}$. It thus is to be expected (and found) that the properties of a running coupling will strongly depend on the physical observable used to define it [30].

3.2 Real time properties of finite temperature QCD, spectral functions

Most of the dynamic properties of the finite temperature system are incorporated in the spectral functions. The spectral function, $\sigma_H(p_0,\vec{p})$, for a given mesonic channel H in a system at temperature T can be defined through the Fourier transform of the real time two point functions $D^>$ and $D^<$ or equivalently as the imaginary part of the Fourier-transformed retarded correlation function [35],

$$\begin{aligned}
\sigma_H(p_0,\vec{p}) &= \frac{1}{2\pi}(D^>_H(p_0,\vec{p}) - D^>(p_0,\vec{p})) \\
&= \frac{1}{\pi}{\rm Im}D^R_H(p_0,\vec{p}) \\
D^{>(<)}_H(p_0,\vec{p}) &= \int \frac{d^4p}{(2\pi)^4} e^{ip.x} D^{>(<)}_H(x_0,\vec{x}) \qquad (7.22)\\
D^>_H(x_0,\vec{x}) &= \langle J_H(x_0,\vec{x}), J_H(0,\vec{0})\rangle \\
D^<_H(x_0,\vec{x}) &= \langle\langle J_H(0,\vec{0}), J_H(x_0,\vec{x})\rangle \ , x_0 > 0 \ . \qquad (7.23)
\end{aligned}$$

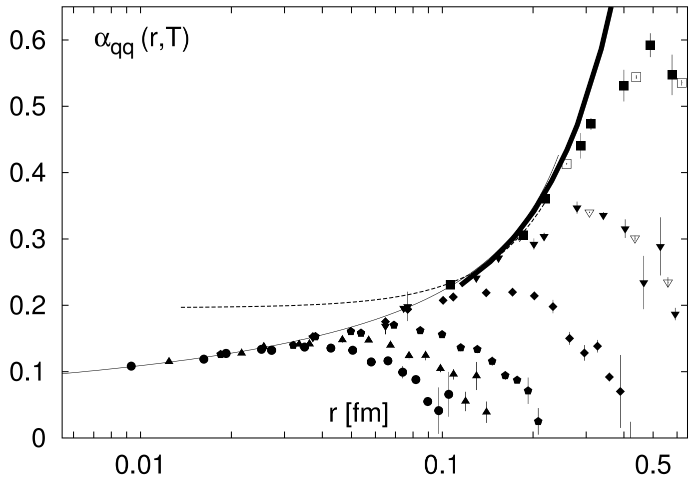

Fig. 7.3: The running coupling in the qq-scheme determined on lattices of size $32^3 \times N_\tau$ with $N_\tau = 4$ (open symbols) and 8 (filled symbols) from derivatives the short distance part of the singlet free energy ($T = 0$: from the force) at different temperatures. The relation of different symbols to the values of the temperature are as in the previous figure (left). The various lines correspond to the string picture (dashed), perturbative (thin) and numerical (thick) studies at zero temperature.

The correlators $D_H^{>(<)}(x_0, \vec{x}\,)$ satisfy the well-known Kubo–Martin–Schwinger (KMS) condition [35]

$$D_H^{>}(x_0, \vec{x}\,) = D^{<}(x_0 + i/T, \vec{x}\,) \ . \tag{7.24}$$

Inserting a complete set of states and using Eq. (7.24), one gets the expansion

$$\begin{aligned} \sigma_H(p_0, \vec{p}) = \frac{(2\pi)^2}{Z} \sum_{m,n} \quad & (e^{-E_n/T} \pm e^{-E_m/T}) |\langle n | J_H(0) | m \rangle|^2 \\ \times \quad & \delta^4(p_\mu - k_\mu^n + k_\mu^m) \end{aligned} \tag{7.25}$$

where e.g., k^n refers to the four-momenta of the state $|n\rangle$.

A stable mesonic state contributes a δ function-like peak to the spectral function,

$$\sigma_H(p_0, \vec{p}) = |\langle 0 | J_H | H \rangle|^2 \epsilon(p_0) \delta(p^2 - m_H^2) \ , \tag{7.26}$$

where m_H is the mass of the state. For an unstable particle, a smoother peak is obtained with a width related to the decay width. For sufficiently small decay widths, a Breit–Wigner form is commonly used. As the temperature increases, the contributions from states in the spectral function changes due to collision broadening, and, at sufficiently high temperatures, these states may be too broad to contribute to the resonance any longer. Such a change in the contributions to the resonance states and eventual ‘disappearance of resonances’ in the thermal spectral function has been studied analytically, for example, in the Nambu–Jona–Lasinio model in Ref. [36]. The spectral function as defined in Eq. (7.25) is directly accessible in high energy heavy ion experiments. For example, the spectral function for the vector current is directly related to the differential thermal cross-section for the production of lepton pairs [37]

$$\frac{dW}{dp_0 d^3p} = \frac{5\alpha^2}{27\pi^2} \frac{1}{p_0^2 (e^{p_0/T} - 1)} \sigma(p_0, \vec{p}) \ . \tag{7.27}$$

Then presence or absence of a bound state in the spectral function will manifest itself in the peak structure of the differential dilepton rate.

In finite temperature lattice calculations, one calculates Euclidean time propagators, usually projected to a given spatial momentum

$$G_H(\tau, \vec{p}) = \int d^3x e^{i\vec{p}.\vec{x}} \langle T_\tau J_H(\tau, \vec{x}) J_H(0, \vec{0}) \rangle_T \tag{7.28}$$

where $\langle ... \rangle_T$ indicates a thermal trace, as in Eq. (7.22), and T_τ refers to ordering in Euclidean time τ. This quantity is the analytical continuation of $D^>(x_0, \vec{p})$

$$G_H(\tau, \vec{p}) = D^>(-i\tau, \vec{p}) \ . \tag{7.29}$$

Using this equation and the KMS condition one can easily show that $G_H(\tau, \vec{p})$ is related to the spectral function, Eq. (7.22), by an integral equation

$$\begin{aligned} G_H(\tau, \vec{p}) &= \int_0^\infty d\omega \sigma(\omega, \vec{p}) K(\omega, \tau) & (7.30) \\ K(\omega, \tau) &= \frac{\cosh(\omega(\tau - 1/2T))}{\sinh(\omega/2T)} \ . & (7.31) \end{aligned}$$

Equation (7.30) lies at the heart of attempts to extract spectral functions and properties of hadrons from correlators calculated in lattice QCD. In what follows, we use Eq. (7.30) to extract the behavior of degenerate heavy meson systems in a thermal medium from finite temperature mesonic correlators. Equation (7.31) is valid only in the continuum. It is not clear in general whether the $G_H(\tau, \vec{p})$ measured on the lattice will satisfy the same spectral representation but it was shown in Ref. [38] that this is the case for the free theory.

3.3 Charmonium at finite temperature: recent results on correlators and spectral functions

Direct investigations of the charmonia temperature modifications, using the Matsubara correlators of suitable operators, have been available over the past 3–4 years. All such studies available at present are based on quenched lattices, that is, they do not include any quark loops, even thermal quark loops (which indicates scattering of thermal quarks off the medium). Excluding such loops may result in exclusion of important physics below T_c since the thermal excitation of pions and meson resonances is considered to be one of the main driving mechanisms of the QCD phase transition. Above the transition, at least for J/ψ dissociation, the existing wisdom is that the thermal gluons are the more relevant degrees of freedom. Therefore, the description of quenched lattices should be at least qualitatively correct.

In the following, the current status of the direct lattice studies on charmonia are summarized. Only the main results are described here. For detailed analysis of the systematics and other effects, please refer to the original papers [39–41]. As already mentioned in the previous section, detailed information about the hadronic properties are contained in the spectral function. In order to study thermal modifications of hadrons, ideally Eq. (7.30) should be inverted to extract $\sigma(\omega, T)$ from the thermal correlators. (In the following, we will only be interested in mesonic states at rest in the heat-bath frame, i.e., $\vec{p} = 0$ in Eq. (7.30), and will omit the $\vec{p}$ index altogether.) However, such an inversion is a notoriously ill-defined problem, since the continuous function, $\sigma(\omega, T)$ must be extracted from the correlators at a discrete number of points. Progress in solving this problem became possible with the introduction of Bayesian techniques in lattice data analysis [42]. In the Maximum Entropy Method (MEM), one can determine the most probable spectral function which describes the data, subject to known constraints like positivity, asymptotic behavior, etc. [43]. At temperatures a few times T_c or higher, however, as we will see below, it is tricky to extract the spectral function even with these techniques.

We begin with the low temperature phase where the larger extent of the temporal direction makes it easier to extract the spectral functions. In Fig. 7.4 we show the spectral functions in the hadronic phase for the currents J_H in different representations. Figure 7.4(a) shows the spectral functions obtained at

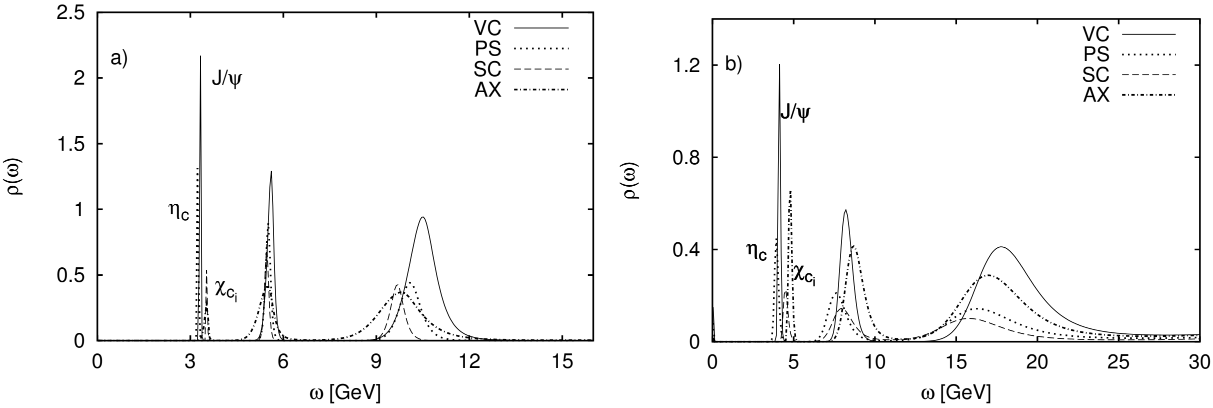

Fig. 7.4: Spectral functions for the vector, pseudos-calar, scalar and axial vector operators [39]. (a) Lattices at 0.75 T_c with $a = 0.04$ fm spacing and (b) at 0.9 T_c and $a = 0.02$ fm. The ground state peaks correspond to J/ψ, η_c, χ_{c_0} and χ_{c_1}, respectively. The label χ_{c_i} is used because the χ_{c_0} and χ_{c_1} are difficult to resolve on the figure.

0.75 T_c on lattices with 0.04 fm spacing. The peaks at low ω correspond to the ground state J/ψ (VC), η_c (PS), χ_{c_0} (SC) and χ_{c_1} (AX) respectively. Note that we do not discuss the $2S$ and $2P$ states because these are indistinguishable from lattice artifacts. The properties of the lowest states are reproduced quite well by Fig. 7.4 since the peak position and the integrated width of the peak are in reasonable agreement with the mass and residue obtained from a fit. Figure 7.4(b) shows spectral functions obtained from lattices with 0.02 fm spacing at $T = 0.9T_c$. A comparison of the two figures helps explain the nature of the peaks at higher ω, since they can be seen to scale approximately as the inverse lattice spacing and therefore are probably dominated by lattice artifacts [39, 44]. It is interesting to note that even at very high ω the structure of the spectral function is quite different from the free theory.

It is possible to get a first idea of the temperature modification of the charmonia above T_c by looking at the Matsubara correlators measured at these temperatures. To factor out the trivial temperature dependence of the kernel (see Eq. (7.31)), one can construct 'model correlators' by using the spectral function from the hadron phase (Fig. 7.4). The measured correlators, $G(\tau, T)$, are then compared with these reconstructed correlators using Eq. (7.31):

$$G_{\rm recon}(\tau, T) = \int_0^\infty d\omega \sigma(\omega, T^*) \frac{\cosh(\omega(\tau - 1/2T))}{\sinh(\omega/2T)}. \tag{7.32}$$

Here T^* refers to a temperature below T_c. Figure 7.5 shows such a comparison for the $1S$ and $1P$ channels in two figures from Ref. [39]. While the comparison at 1.1 T_c uses the spectral function constructed at $T^* = 0.75T_c$, Fig. 7.4(a), the other temperatures use the spectral functions shown in Fig. 7.4(b), i.e., $T^* = 0.9T_c$. The figure clearly shows that the $1S$ states are not strongly affected by the deconfinement transition. For the η_c we see no statistically significant change up to temperatures of 1.5 T_c and only very modest changes at 2.25 T_c. For the J/ψ, the ratio $G(\tau, T)/G_{\rm recon}(\tau, T)$ shows no significant deviations from unity at short Euclidean time, τ, a little above T_c, while some small but significant deviations are seen as one goes to higher temperatures. For the $1P$ channels, large temperature modifications of the correlator relative to the reconstructed correlator are seen when crossing T_c, indicating that the $1S$ states undergo only very modest modifications up to 1.5–2 T_c while the $1P$ states suffer more serious modifications.

In order to further understand the nature of thermal modifications of the states, it is necessary to extract the spectral function directly from the correlators. Three groups have presented results for spectral functions for the pseudo-scalar and vector charmonium states using the MEM. Since the extraction becomes tricky at high temperatures and there are some differences in the results, it is useful to keep in

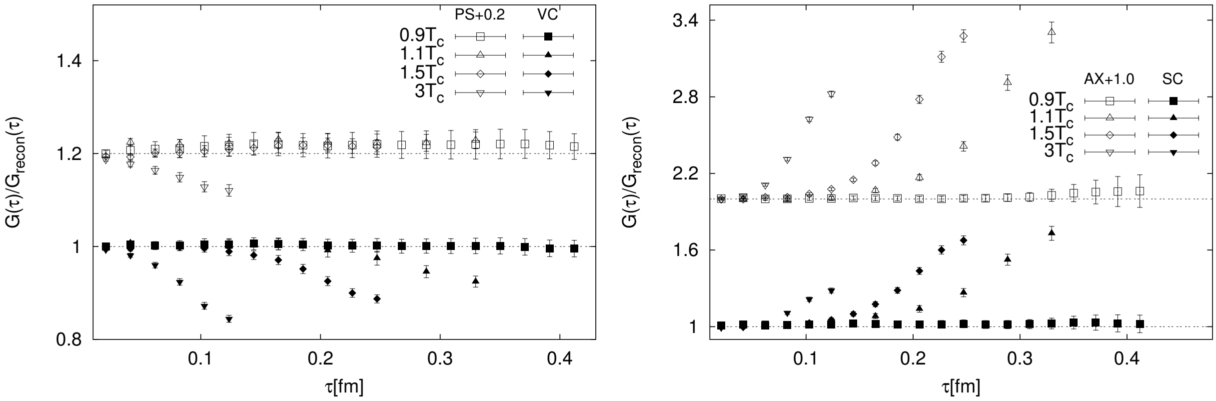

Fig. 7.5: G/G_{recon} as a function of Euclidean time for different temperatures for vector and pseudo-scalar channels (top) and in the scalar and axial vector channels (bottom). The figures above mix two sets of data in Ref. [39] with different lattice spacings and slightly different quark masses, with the data at 1.1 T_c using $T^* = 0.75\ T_c$ and the others using $T^* = 0.9\ T_c$. The data for the pseudo-scalar and axial vector channels have been shifted by a constant for better visualization.

mind the initial differences between them. While all three work within the quenched approximation and use Wilson-type valence fermions, some differences exist in their approaches. The Bielefeld group uses very fine isotropic lattices with the nonperturbatively improved clover action for the valence fermions. Asakawa and Hatsuda use space–time anisotropic lattices, to allow more data points in the temporal direction and use the unimproved Wilson action for the fermions. Umeda *et al.* also use anisotropic lattices but use the tadpole-improved Fermilab action. They also use smeared operators while the others use point operators.

As Fig. 7.4 reveals, the structure of the spectral function at high ω, for the interacting theory on lattice, is considerably different from the free spectral function [44]. The Bielefeld group uses this high energy structure as part of the prior information when extracting the spectral function. The default spectral function above T_c, in their analysis, uses the high energy part of Fig. 7.4, continuously matched to $m_1\omega^2$ at lower ω where m_1 is defined to match the spectral functions at temperatures below T_c. The spectral functions for the $1S$ states, obtained with this default model and the MEM analysis of Bryan [45], are shown in Fig. 7.6. The error bars shown in the figure are standard deviations of the spectral functions averaged over the ω interval indicated by the horizontal error band (see [43], Eq. (5.13)). We see that, up to 1.5 T_c the $1S$ states persist as bound states with no significant weakening. There is also no significant change in mass on crossing T_c. At 2.25 T_c, while the peak position is still not significantly changed, a depletion of the peak strength, i.e., the area under the peak, is seen. Finally, at 3 T_c no statistically significant peak is seen.

Figure 7.6 suggests that in a gluonic plasma the $1S$ charmonia survive as bound states till $\geq 2T_c$, with no significant weakening up to $\approx 1.5\,T_c$ and then a gradual weakening, perhaps due to collision broadening. Since these results are for point operators, the results for the vector current, Fig. 7.6(b), will be directly connected to the thermal dilepton rate. Further results for point operators come from Asakawa and Hatsuda who use the free continuum asymptotic form of the spectral function, $\approx m_1\omega^2$, as their default model. Their latest results [46] are shown in Fig. 7.7. They find a sharp bound state, with little significant thermal modification, up to 1.62 T_c, in complete agreement with Fig. 7.4 up to 1.5 T_c. On going to higher temperatures, however, their results seem to suggest a sharp disappearance of the bound states at some temperature, with no statistically significant peak being seen at 1.9 T_c [40] and, in preliminary results, already at 1.7 T_c [46]. While the exact dissolution temperature is probably not expected to match the Bielefeld group, since the Bielefeld group uses a quark mass somewhat heavier than

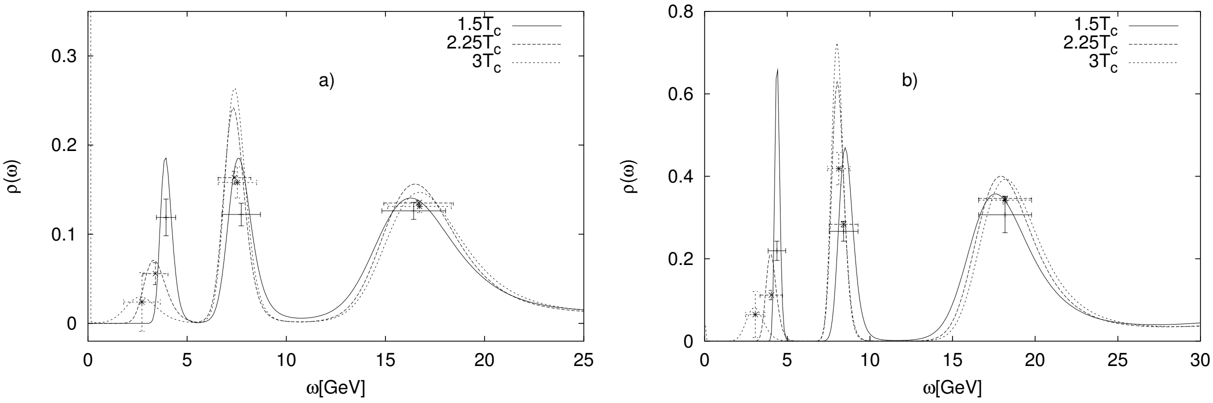

Fig. 7.6: Spectral functions above deconfinement for (a) pseudo-scalar and (b) vector channels [39]. Here lattice spacing $a \approx 0.02$ fm and $m_{J/\psi} \approx 3.6$ GeV.

the charm, if further analysis supports the dissolution at 1.7 T_c then it will clearly suggest a qualitatively different picture from the gradual dissolution shown in Fig. 7.6, and possibly suggest a drastic change in the properties of the plasma between 1.6 and 1.7 T_c.

Unlike the two previous groups, Umeda *et al.* use smeared operators with a smearing function of the form $w(\vec{x}\,) = \exp(-a|\vec{x}\,|^b)$ where the parameters a and b are chosen to optimize the overlap with the ground state. While use of a smeared operator has the advantage of a good overlap with the ground state, so that it may be possible to extract the properties of J/ψ and η_c more reliably, it has two disadvantages. First, bound state dissolution must be carefully handled since smearing always mimics a bound state. Second, the direct connection of the vector current correlator to the dilepton rate, Eq. (7.27, is lost. The first problem can be dealt with by comparing results using a different level of smearing [41].

Figure 7.8 shows their results for the $1S$ spectral functions. Evidence for the existence of a bound state above T_c is found for the $1S$ states, in agreement with results of other groups using point operators. No dramatic change between 1.4 T_c and 1.75 T_c is indicated in the properties of the peak. In addition, Umeda *et al.* [41, 46] attempted a constrained fit of the correlators to obtain more accurate information on the ground state properties such as thermal modifications of the mass and width. This analysis with extended operators indicate that the masses of ground state charmonia do not change significantly up to temperatures 1.7 T_c. These studies also indicate a non-zero thermal width which increases with temperature. The precise determination of the width, however, appears to be difficult.

We now summarize what direct lattice studies have told us about the properties of the $1S$ states in equilibrium with a plasma. The studies all agree that the J/ψ and the η_c survive the deconfinement transition with little significant change in their properties. At least up to temperatures $\approx$ 1.5 T_c such states exist as bound states in the equilibrated plasma without significant weakening of the state. Here, it may be worthwhile to also mention earlier results from Umeda *et al.* for these states [47]. In this study, where they looked at the fall-off of the $c\bar{c}$ spatial correlation, Umeda *et al.* previously concluded that the $1S$ states survive as bound states, up to temperatures of 1.5 T_c, in a gluonic plasma. Another important fact revealed by the recent studies is that no significant $1S$ state mass reduction is seen above T_c. If, as was the prevailing wisdom, these states become Coulombic above T_c, one may have expected a significant mass reduction which is not seen by any of the groups. Beyond 1.5 T_c there seems to be some disagreement between the different groups: while Ref. [39] and preliminary results from Umeda *et al.* suggest a gradual disappearance of the state, perhaps due to collision broadening, preliminary results from Asakawa and Hatsuda suggest a sharp cutoff temperature below 1.7 T_c, beyond which the gluonic plasma cannot support these bound states.

Results for the orbitally excited χ_c states are available so far only from the Bielefeld group. As was

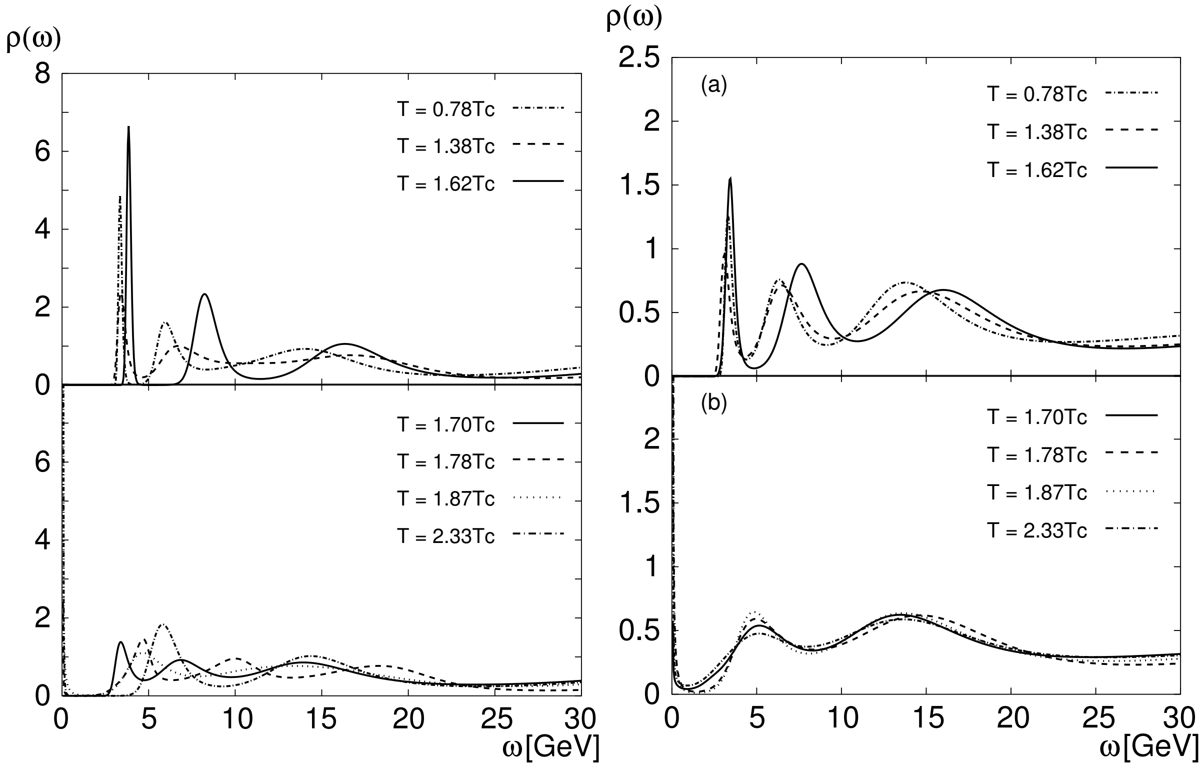

Fig. 7.7: Spectral functions above and below deconfinement for pseudo-scalar (left) and vector (right) channels, for anisotropic lattices with $a_\tau \approx 0.0125$ fm, as found by Asakawa & Hatsuda [40,46]. (a) Temperatures ≤ 1.62 T_c, where a statistically significant ground state is seen. (b) Temperatures $\geq 1.70\,T_c$ where the ground state of (a) is not seen any more. The peak at a slightly higher temperature is not statistically significant.

shown in Fig. 7.5, the behavior of these states is considerably different from that of the $1S$ states since the correlators above T_c differ substantially from the ones reconstructed from the spectral function below T_c, suggesting serious modification of these states due to deconfinement. The spectral functions can be extracted from the correlators even though they are more noisy, making such an extraction somewhat more difficult [39]. Figure 7.9(a) shows the spectral functions for the scalar channel. As before, as part of the prior guess we provided the high ω structure of the lattice spectral function in the interacting theory, as obtained below T_c. The figure shows that the χ_{c_0} peak below T_c is not present already at 1.1 T_c. Figure 7.9(b) shows a similar result for the axial vector channel, indicating these states suffer serious system modification, possibly dissolution, already just above T_c.

3.4 Theory perspectives: NRQCD at $T > 0$

All studies of the charmonium spectral functions mentioned above were done either using relativistic Wilson fermions or Fermilab fermions. In both formulations the so-called Wilson term is introduced to remove the doublers. This, however, strongly distorts the quark dispersion relation on the lattice leading to the artifact peaks in the lattice spectral function. For heavy quarks an additional large discretization error of order $m_q a$ appears where m_q is the heavy quark mass, making bottomonium studies with relativistic actions very difficult although the Fermilab formalism can help to a certain extent. A useful alternative, at least close to T_c, where the condition $m_q \gg T$ necessary for the approach to be valid is satisfied, could be to employ NRQCD at $T > 0$. In this formulation, the scale related to m_q is integrated out so that this formulation has the advantage of being doubler free. Furthermore, since the spectral functions scale as $\sqrt{\omega}$ instead of the ω^2 behavior of the relativistic formulation, the high energy part of the spectral functions contribute less to the meson correlator. This can simplify the reconstruction of meson

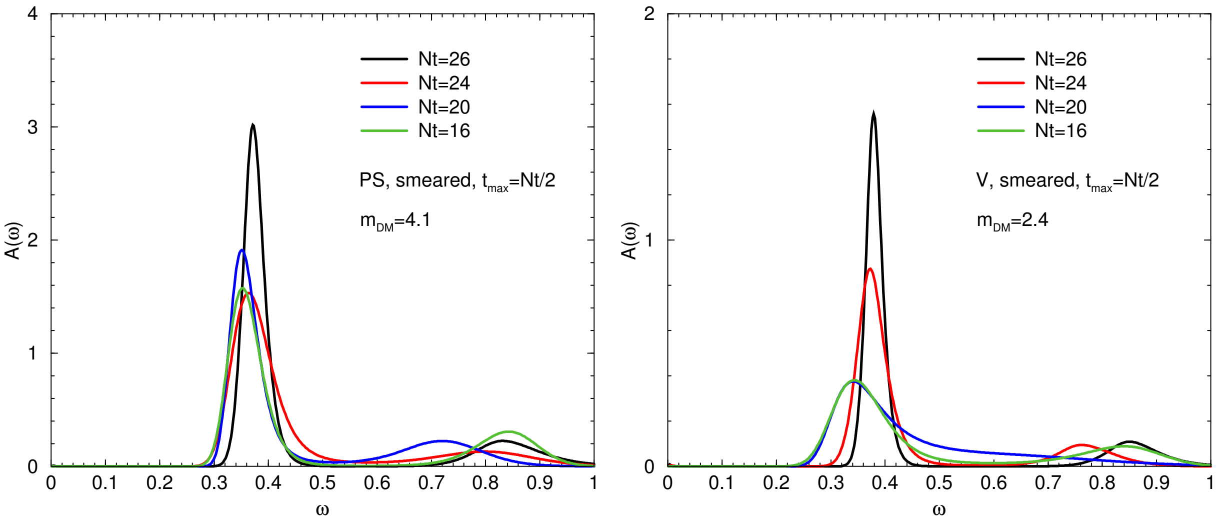

Fig. 7.8: Spectral functions above deconfinement for pseudo-scalar (left) and vector (right) channels, for anisotropic lattices with $a_\tau \approx 0.025$ fm and smeared operators (Umeda *et al.* [41, 46]). The decreasing Nt correspond to $T/T_c \approx 1.08$, 1.17, 1.4 and 1.75, respectively.

properties, related to the low energy part of the vector spectral function. Some preliminary studies of the charmonium spectral function in NRQCD at zero temperature were presented in Ref. [48].

4 J/ψ ABSORPTION IN HEAVY-ION COLLISIONS AT FINITE TEMPERATURE[5]

4.1 Cross-section calculations

Since the original paper by Matsui and Satz [1] on J/ψ suppression in heavy-ion collisions, a number of studies on J/ψ absorption in nuclear matter have been proposed to suggest other mechanisms than the quark gluon plasma screening of the $c\bar{c}$ potential. We will use the words “suppression” and “absorption” to distinguish between the plasma and non-plasma mechanisms responsible for the observed reduced yield of J/ψ particles in heavy ions collisions.

According to Ref. [1], one should observe very few J/ψ in heavy-ion collisions because plasma formation could weaken the effectiveness of the quarkonium potential and prevent J/ψ formation. But what if no plasma phase is generated? The J/ψ can be produced in the early stages of the collision since the energy is high enough to produce them. Their destiny is then related to the interactions they will experience with the nuclear medium (the nuclear thickness the J/ψ must traverse during the intepenetration of the two colliding nuclei) and with the hadron gas (a possible state excited from vacuum left behind in the collision region by the two receding nuclei, assuming zero baryon number).

The $J/\psi N$ cross-section, $\sigma_{\rm abs}$, extracted from data is $\sigma_{\rm abs} = 4.3 \pm 0.6$ mb [49]. The exponential absorption factor for the J/ψ in nuclear matter is $\propto \exp(-x/\lambda)$, where x is the distance traveled and λ is the mean free path, given by

$$\lambda \approx 1/(\rho_A \sigma_{\rm abs}), \tag{7.33}$$

where ρ_A is the nuclear density. Nuclear absorption alone cannot explain the anomalous J/ψ suppression described as a function of length in Ref. [50]. This argument has been used in favor of a plasma interpretation. On the other hand, nuclear absorption does not take into account interactions with all hadrons ($\pi, \eta, K, \rho, \omega, K^*, \phi$...) that can be excited from vacuum when very high energy densities are reached, as in heavy-ion collisions. Each of these particles is presumably able to interact with the J/ψ,

---

[5] Section coordinator: A. D. Polosa; Authors: V. Laporta, L. Maiani, F. Piccinini, A. D. Polosa, V. Riquer

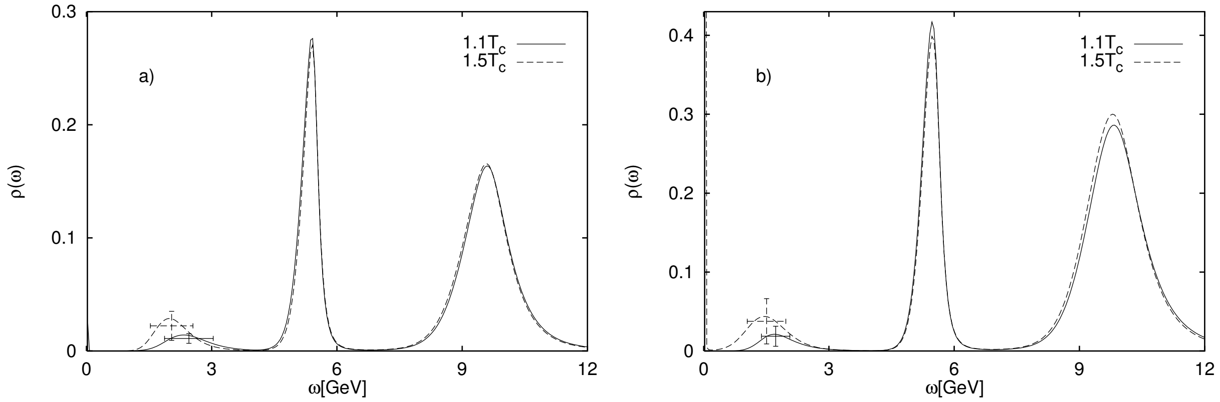

Fig. 7.9: Spectral functions for (a) scalar and (b) axial vector states above deconfinement, reconstructed from Matsubara correlators measured on lattices of ≈ 0.04 fm spacing [39].

reshuffling its $c\bar{c}$ content into an open charm final state such as $D^{(*)}_{(s)} D^{(*)}_{(s)}$. Can such interactions provide an explanation of the anomalous suppression?

The description of these interactions is difficult because they cannot be derived from first principles or extracted from independent experimental information. One has to resort to models of their dynamics [51–58].

Dissociation of the J/ψ by hadrons has been considered in several approaches, with rather different predictions for energy dependence and magnitude of the cross-sections near threshold. Basically, earlier calculations in the literature can be grouped into four classes:

- perturbative QCD based calculations (pQCD);
- quark interchange models;
- QCD sum rule calculations;
- meson exchange models.

The idea behind the pQCD method is that the interaction between heavy quark bound states and light hadrons can be described perturbatively when the heavy quark mass is sufficiently large. The small size of the heavy quark bound state allows for a multipole expansion of its interaction with external gluons where the colour-dipole interaction dominates at long range. Using pQCD, Peskin and Bhanot and later Kharzeev and Satz [52] estimated the scattering cross-sections of J/ψ with light hadrons, finding very low values, less than 0.1 mb at about $\sqrt{s} = 5$ GeV. The pQCD result was further improved by including finite target mass corrections and relativistic phase space corrections [53]. However, the collisions between mesons and the J/ψ in heavy-ion reactions occur at low energy where the application of pQCD is questionable.

In the case of quark interchange models, the J/ψ dissociation cross-section is calculated in terms of non-perturbative quark exchanges between the J/ψ and light hadrons using explicit non-relativistic quark model wave functions for the initial and final hadrons. The largest contributions to the cross-section come from the energy region just a few hundred MeV above threshold since the overlap integrals are damped by the external meson wave functions at higher momenta. The first calculation in this framework was performed by Martins, Blaschke and Quack [54], finding a J/ψ dissociation cross-section by pions of ≈ 7 mb at about 1 GeV above threshold. Subsequently, similar calculations have been carried out with different treatments of the confining interaction, obtaining lower cross-sections (of the order of 1.5 mb at $\sqrt{s} \approx 4$ GeV) and have been extended to $\rho J/\psi$ and $N J/\psi$ interactions [55].

Another independent approach is given by the QCD sum rules [56]. This method relates the scattering amplitude to a sum of operator vacuum-expectation-values (VEVs). It gives a model independent

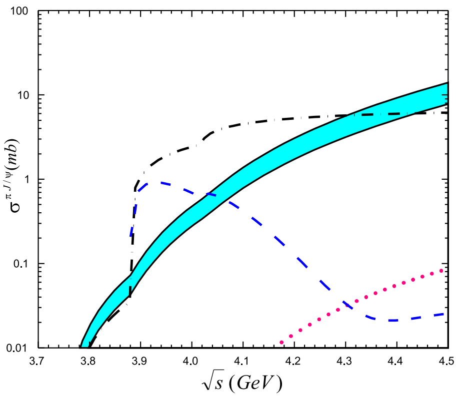

Fig. 7.10: The J/ψ-hadron cross-sections calculated with QCD sum rules (band), short-distance QCD (dotted line), meson-exchange models (dot–dashed lines) and the non-relativistic constituent quark model (dashed line) [60].

result provided that the set of selected operators dominates the scattering amplitude in the chosen kinematic regime and that their VEVs are known experimentally. QCD sum rule calculations for the reaction $\pi + J/\psi \rightarrow D^{(*)}\overline{D}^{(*)}$ give cross-sections at the mb level in the near-threshold region.

Finally, the meson-exchange model [57], is based on hadronic effective Lagrangians. Vector mesons are treated as gauge bosons mediating the interactions between pseudoscalar mesons. An SU(4)-invariant effective meson Lagrangian is assumed. One starts from a free Lagrangian of the form $\mathcal{L}_0 = \mathrm{Tr}(\partial_\mu P^\dagger \partial^\mu P) - 1/2\mathrm{Tr}(F^\dagger_{\mu\nu} F^{\mu\nu})$ and derives the couplings between pseudoscalar and vector mesons with the minimal substitution

$$\begin{aligned} \partial_\mu P &\rightarrow \partial_\mu P - i/2g[V_\mu, P] \\ F_{\mu\nu} &\rightarrow \partial_\mu V_\nu - \partial_\nu V_\mu - i/2g[V_\mu, V_\nu] \;, \end{aligned} \tag{7.34}$$

giving rise to three-vector meson couplings and four-point couplings. The values of the couplings are obtained from experimental results via Vector Meson Dominance and SU(4) relations, although the assumption of SU(4) symmetry is rather questionable. The most studied channels are: $\pi J/\psi$, $\rho J/\psi$, $K J/\psi$ and $K^* J/\psi$ where quite large cross-sections, of the order of $1 - 10$ mb, have been obtained [58]. Since the exchanged mesons are not pointlike, several studies have introduced form factors at the interaction vertices at the price of introducing additional unknown or poorly known parameters. A strong dependence on the shape and cutoff values of the form factors is found. Some authors calculate the interaction vertices and form factors with the help of sum rules [59]. The state of the art of these calculations, including an uncertainty band, is summarized in Fig. 7.10 [60]. For a nice review of these topics see Ref. [61].

With the exception of pQCD, these approaches, each subject to different limitations, give cross-sections on the order of mb, in particular for initial π's and ρ's. This is a clear indication that the picture of J/ψ absorption by nuclear matter as the only alternative mechanism to plasma suppression is incomplete and that interactions with *comoving particles* in the hadron gas have to be taken into account. We will not attempt to further review existing approaches. We instead focus on some more recent calculations which do not fall in the four classes described above. The $(\pi, \eta, K, \rho, \omega, K^*, \phi) J/\psi \rightarrow D^{(*)}_{(s)} D^{(*)}_{(s)}$ cross-sections have recently been evaluated [63], based on the Constituent Quark Model (CQM). The CQM was originally devised to compute exclusive heavy-light meson decays and was tested on a large number of such processes [65]. The CQM is based on an effective Lagrangian which incorporates the heavy quark spin-flavour symmetries and chiral symmetry in the light sector. In particular, it contains effective vertices between a heavy meson and its constituent quarks, as shown on the left-hand side of Fig. 7.11, which occur when applying bosonization techniques to the Nambu–Jona–Lasinio interaction terms of

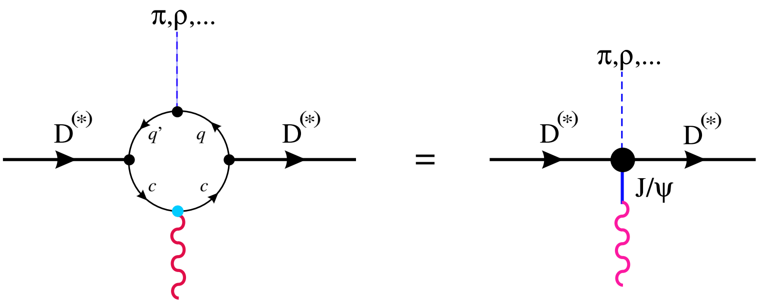

Fig. 7.11: Basic diagrammatic equation to compute the couplings g_3 and g_4.

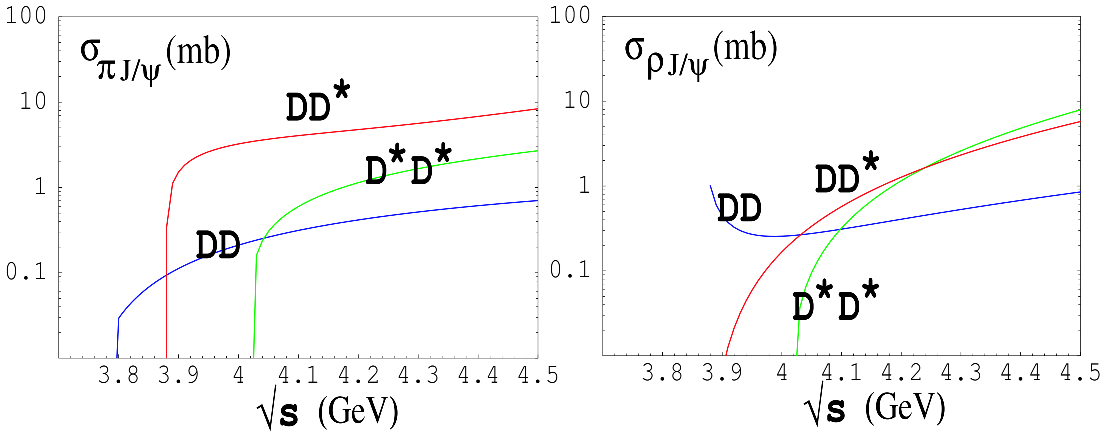

Fig. 7.12: Cross-sections in CQM model. On the left-hand side, the cross-sections $\pi J/\psi \to D^{(*)}D^{(*)}$ modulated by a form factor (ff) directly derived from the model [67] are shown. The case of $\rho J/\psi$ interactions is technically more complicated and it does not seem feasible to extract the dependency on E_ρ of these cross-sections in the form of a polar ff. If we compute physical quantities such as the mean free paths determined by the inverse of thermal averages, $\langle \rho^{(\rho)}\sigma \rangle_T$, where $\rho^{(\rho)}$ is the ρ number density, the Boltzmann factor will serve as an exponential ff cutting high energy tails faster than any polar ff.

heavy and light quark fields [66]. On this basis, we believe that the CQM is a more solid approach than effective Lagrangian methods, often based on SU(4) symmetry.

We compute the effective trilinear, $g_3 = (\pi, \eta, K, \rho, ...)D^{(*)}_{(s)}D^{(*)}_{(s)}$, or $g_3 = J/\psi D^{(*)}_{(s)}D^{(*)}_{(s)}$ and quadrilinear, $g_4 = (\pi, \eta, K, \rho, ...)J/\psi D^{(*)}_{(s)}D^{(*)}_{(s)}$, couplings. In Fig. 7.11 we show the diagrammatic equation which has to be solved in order to obtain $g_4(g_3)$ in the various cases. The right-hand side represents the effective four-linear coupling to be used in the cross-section calculation. To obtain the trilinear couplings we suppress either the J/ψ or one of the dashed lines representing the light resonances. The effective interaction at the meson level (right-hand side) is modeled as an interaction at the quark-meson level (left-hand side of Fig. 7.11).

The J/ψ is introduced using a Vector Meson Dominance (VMD) ansatz. In the effective loop on the left-hand side of Fig. 7.11 we have a vector current insertion on the heavy quark line c while on the right-hand side the J/ψ is assumed to dominate the tower of $J^{PC} = 1^{--}$ $c\bar{c}$ states mixing with the vector current, for more details see Refs. [17, 67]. Similarly, vector particles coupled to the light quark component of heavy mesons such as ρ and ω when $q = (u, d)$ and K^*, ϕ, when one or both light quarks are strange, are also taken into account using VMD arguments. The pion and other pseudoscalar fields have a derivative coupling to the light quarks of the Georgi–Manohar kind [68]. The final results for $\sigma_{\pi J/\psi}$ and $\sigma_{\rho J/\psi}$ are displayed in Fig. 7.12.

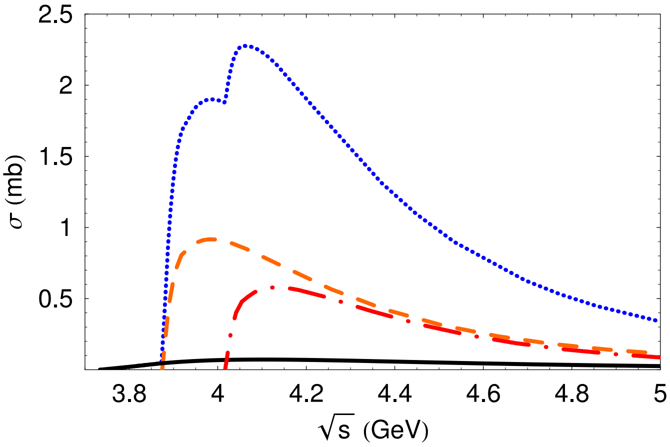

Fig. 7.13: The total cross-section (dotted line) together with the contributions coming from the $J/\psi + \pi \to D + \overline{D}$ (solid line), $J/\psi + \pi \to D^* + \overline{D}$ (dashed line) and $J/\psi + \pi \to D^* + \overline{D^*}$ (dot–dashed line) processes are shown.

The authors of Ref. [69] employ a relativistic quark model [70] to calculate amplitudes and cross-sections for the same processes discussed above with only pions in the initial state. Their model is based on an effective Lagrangian which describes the coupling of hadrons H to their constituent quarks, q_1 and $\overline{q}_2$, given by:

$$\mathcal{L}_{\rm int}(x) = g_H H(x) \int dx_1 \int dx_2 F_H(x, x_1, x_2) \overline{q}_2(x_2) \Gamma_H \lambda_H q_1(x_1) \; + \text{h.c.}\,. \tag{7.35}$$

Here, λ_H and Γ_H are the Gell-Mann and Dirac matrices which describe the flavour and spin quantum numbers of the meson field $H(x)$. The vertex function F_H is given by:

$$F_H(x, x_1, x_2) = \delta\left(x - \frac{m_1}{m_1+m_2} x_1 - \frac{m_2}{m_1+m_2} x_2\right) \Phi_H\left((x_1 - x_2)^2\right), \tag{7.36}$$

where Φ_H is the correlation function of two constituent quarks of mass m_1 and m_2. Moreover, for Φ_H, in momentum space, they chose the form $\tilde{\Phi}_H(k_E^2) \doteq \exp(-k_E^2/\Lambda_H^2)$, where k_E is a Euclidean momentum [71]. The coupling g_H is determined by the compositeness condition discussed in Ref. [69]. By using the corresponding Feynman rules, the S-matrix elements describing hadronic interactions are obtained in terms of a set of quark diagrams.

In this approach, the dissociation processes are described by box and resonance diagrams. The details of the cross-section calculations can be found in Ref. [69]; here we show the numerical results for the cross-sections as a function of $\sqrt{s}$.

In Fig. 7.13 the continuous line represents the $J/\psi + \pi \to D + \overline{D}$ cross-section while the dashed and the dot–dashed lines are for $J/\psi + \pi \to D^* + \overline{D}$ and $J/\psi + \pi \to D^* + \overline{D^*}$, respectively. The dotted line shows the total cross-section as a function of $\sqrt{s}$. One can see that the maximum is about 2.3 mb at $\sqrt{s} \approx 4.1$ GeV. This value turns out to be smaller than the previous one, but still in the millibarn range.

To make a realistic computation of the effect of the interactions with the hadronic gas, several things have to be considered.

1. There is a temperature dependence of absorption in the hadron gas due to the energy dependence of the cross-sections and to the fact that, as the temperature varies, the particle content and the characteristics of the hadron gas change. One should calculate thermal averages $\langle \rho\sigma \rangle_T \approx 1/\lambda$. This can be done, e.g., by simply using the Bose distribution with zero chemical potential in an ideal gas approximation [62, 63].

2. There is a problem of convergence. Including heavier resonances, on one hand, is disfavored because of the Boltzmann factor $\exp(-M/T)$. On the other hand, heavier resonances, h, integrate more cross-section at low momentum in the $hJ/\psi \rightarrow D\overline{D}$ channel and have large spin multiplicities. The lowest lying vector meson nonet, for instance, has a charge-spin multiplicity 9 times larger than that of pions. It is difficult to asses a priori the relative weight of these two effects.
3. Some arguments indicate that there may be a limiting temperature of hadronic matter: the Hagedorn temperature, $T_H \simeq 177$ MeV, [64]. To be credible, a purely hadronic interpretation of J/ψ absorption should be for temperatures $T \leq T_H$.
4. The SPS collaboration NA50 studies the J/ψ yield as a function of the collision centrality. At a certain centrality there is some evidence of a discontinuous breakdown in the J/ψ yield [73–75]. Can such a discontinuity be explained by some hadronic absorption mechanism where cross-sections are expected to be mainly smooth polynomials?

Studying absorption versus suppression is like estimating the background to a weak signal. The shape and size of the background can be crucial in assessing the reliability of the signal.

4.2 Comparison with data

As stated earlier, nuclear absorption can be taken into account by the factor $\exp(-\rho_A \sigma_{\text{abs}} L)$, where ρ_A is the nuclear density and L the path length the J/ψ's traverse during the intepenetration of the two colliding nuclei.

To compute the effect of the hadron gas also requires modeling the fireball produced by the two receding nuclei. We will briefly describe the working hypotheses adopted in two recent papers [62, 63].

1. The fireball is a zero baryon density region of approximately spherical shape which the J/ψ has to escape to be detected.
2. The fireball thermalizes as a hadron gas at temperature T soon after its formation. Primary collisions give rise mostly to pions with an average energy of about 300 MeV and a density of few/(fm^3) and interaction cross-sections of about 10 mb. These parameters lead [72] to mean free paths of a fraction of a fermi, much shorter than the linear dimensions of the fireball, $\approx 5 - 10$ fm.
3. The hadron gas is at zero chemical potential. This is an especially reasonable hypothesis for pions.
4. We calculate the thermal averages $\langle \rho\sigma \rangle_T$ using an ideal gas at temperature T. Interactions can be taken into account by allowing higher and higher resonances in the gas.
5. The NA50 data [73–75] can be plotted as a function of collision centrality. The more central the collision, the larger the average size of the fireball and the higher the energy density.

We take both nuclear and hadronic absorption into account by the convolution of two exponentials, $\exp[-L(l)/\lambda] \exp[-l/\lambda(T)]$ where $\lambda(T)$ is the mean free path of the J/ψ through the hadron gas, $l = 2R_A - b$, R_A is the nuclear radius and b is the impact parameter. The first exponential is for nuclear absorption while the second takes the thermal mean free path through a hadron gas into account. One can introduce such a dependence on l by assuming that the energy density, ϵ, depends on the number of nucleons divided by the effective surface area of the nuclear interaction as a function of b [72]. Using the energy–temperature relation appropriate to the hadron gas, one can determine the temperature profile as function of centrality and the corresponding absorption profile.

In Fig. 7.14 (a) and (b) we show the calculated absorption (nuclear + hadron gas) superimposed on the NA50 data [73–75]. The boxes show the Pb+Pb data while the stars give the S+U data. The temperatures indicated on the curves are the temperatures at low centrality (the first three points from the left). The hadron gas picture is more reliable in more peripheral collisions.

It is very interesting to note that the estimated temperatures are in the same region as the temperature expected for the phase transition and close to the temperatures measured at freeze-out from various hadron abundances. The curve labeled with $T = 175$ MeV, where T varies from 175 to about 195 MeV,

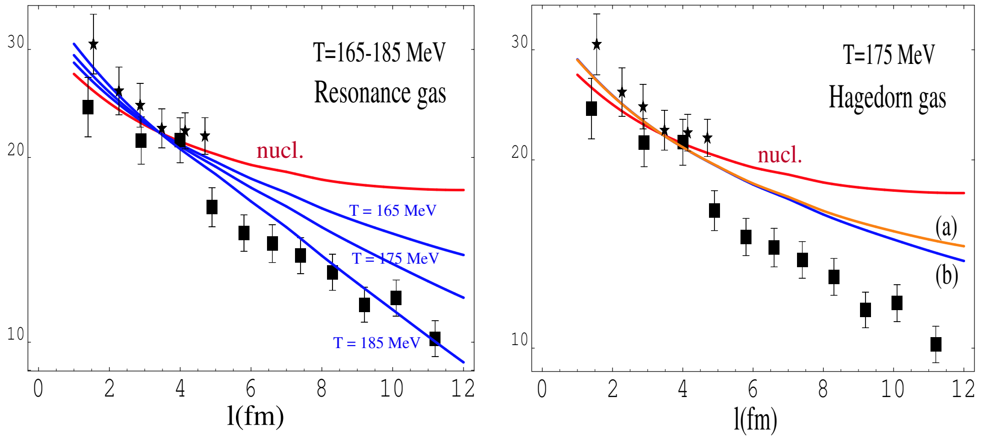

Fig. 7.14: Left-hand side: The exponential attenuation model compared to Pb+Pb (boxes) and S+U (stars) J/ψ normalized to Drell–Yan for three different values of the initial temperature in the hadron gas. The curve labeled as "nucl." includes only nuclear absorption effects. The other curves include both hadron gas and nuclear attenuation. Right-hand side: Same but for a Hagedorn gas. The curves labeled (a) and (b) show that there is no significant centrality dependence of the temperature since (one of the two curves shown has the geometrical effect switched off)

fits the data for low centrality but still falls short of reproducing the observed drop in J/ψ production above $l = 5$ fm. The curve with $T = 185$ MeV fits the low centrality data and agrees relatively well with the data in central collisions. However the temperature rises to 200 MeV at $l \simeq 11$ fm, likely too high for a hadron gas (see below).

The increase in temperature due to the increase in energy density that we find for the resonance gas is less pronounced than in the case of a pure pion gas in Ref. [62] because the number of degrees of freedom in the resonance gas increases appreciably with temperature. The extra energy density has to be shared among more and more degrees of freedom and the temperature increases less than with a fixed $\epsilon = CT^4$ power law. This behaviour begins to reproduce that expected from a Hagedorn gas with an exponentially increasing resonance density per unit mass interval [64, 76, 77].

The extrapolation to increasing centrality using the energy–temperature relation of the Hagedorn gas is shown in Fig. 7.14 (b) with $T = 175$ MeV. The result is quite spectacular. The sharp rise of the degrees of freedom due to the vicinity of the Hagedorn temperature makes the temperature of the gas nearly constant so that the dissociation curve cannot become harder and the prediction falls far short of explaining the drop observed by NA50. The simplest interpretation of Fig. 7.14 (b) is that with increasing centrality, more energy goes into the excitation of more and more thermodynamical degrees of freedom, leading to the final transition to the quark–gluon plasma. The curve shown represents the limiting absorption from the Hadron gas so that anything harder would be due to the dissociation of the J/ψ in the quark–gluon plasma.

Some words of caution are in order. In the framework of our calculation, it is certainly reasonable to expect the relevant insertions in the quark loop of Fig. 7.11 to correspond to the Dirac matrices S, P, A, V, and T where the latter are dominated by the lowest $q\bar{q}$, S-wave states we have been considering. On the other hand, we cannot exclude that decreasing couplings of the higher resonances may eventually resum up to a significant effect which would change the picture obtained by truncating the cross-section to include only the lowest states.

However, in all cases where this happens, such as in deep inelastic lepton–hadron scattering, the final result reproduces what happens for free quarks and gluons. In our case, this would mean going above the Hagedorn temperature into the quark and gluon gas, precisely what Fig. 7.14 (b) seems to tell us.

5 SHADOWING AND ABSORPTION EFFECTS ON J/ψ PRODUCTION IN D+AU COLLISIONS[6]

The nuclear quark and antiquark distributions have been probed through deep inelastic scattering (DIS) of leptons and neutrinos from nuclei. These experiments showed that parton densities in free protons are modified when bound in the nucleus [78]. This modification, referred to collectively as shadowing, depends on the parton momentum fraction x and the square of the momentum transfer, Q^2. Thus, in addition to the already aforementioned nuclear absorption and secondary hadronic scattering effects, initial state shadowing can also play a role, especially as the energy increases, simultaneously decreasing the values of parton momentum fraction, x, probed in the collision.

Most models of shadowing predict that the modification should vary depending on position within the nucleus [79] but DIS experiments are typically insensitive to this position dependence. However, some spatial inhomogeneity has been observed in νN scattering [80]. Here we discuss the combined effects of shadowing and absorption both in minimum bias d+Au collisions at RHIC and as a function of centrality.

Our calculations employ the colour evaporation model (CEM) which treats all charmonium production identically to $c\overline{c}$ production below the $D\overline{D}$ threshold, neglecting colour and spin. The leading order (LO) rapidity distributions of J/ψ's produced in dA collisions at impact parameter b is

$$\begin{aligned}\frac{d\sigma_{\mathrm{dA}}}{dyd^2bd^2r} &= 2F_{J/\psi}K_{\mathrm{th}}\int dz\,dz'\int_{2m_c}^{2m_D}MdM\left\{F_g^d(x_1,Q^2,\vec{r},z)F_g^A(x_2,Q^2,\vec{b}-\vec{r},z')\frac{\sigma_{gg}(Q^2)}{M^2}\right. \qquad (7.37)\\ &+\left.\sum_{q=u,d,s}[F_q^d(x_1,Q^2,\vec{r},z)F_{\overline{q}}^A(x_2,Q^2,\vec{b}-\vec{r},z')+F_{\overline{q}}^d(x_1,Q^2,\vec{r},z)F_q^A(x_2,Q^2,\vec{b}-\vec{r},z')]\frac{\sigma_{q\overline{q}}(Q^2)}{M^2}\right\}.\end{aligned}$$

The partonic cross-sections are given in Ref. [81], $M^2 = x_1x_2S_{NN}$ and $x_{1,2} = (M/\sqrt{S_{NN}})\exp(\pm y) \approx (m_{J/\psi}/\sqrt{S_{NN}})\exp(\pm y)$ where $m_{J/\psi}$ is the J/ψ mass. The fraction of $c\overline{c}$ pairs below the $D\overline{D}$ threshold that become J/ψ's, $F_{J/\psi}$, is fixed at next-to-leading order (NLO) [82]. Both this fraction and the theoretical K factor, K_{th}, drop out of the ratios. We use $m_c = 1.2$ GeV and $Q = 2m_c$ [82].

We assume that the nuclear parton densities, F_i^A, are the product of the nucleon density in the nucleus, $\rho_A(s)$, the nucleon parton density, $f_i^N(x,Q^2)$, and a shadowing ratio, $S^j_{\mathrm{P,S}}(A,x,Q^2,\vec{r},z)$, where $\vec{r}$ and z are the transverse and longitudinal location of the parton in position space. The first subscript, P, refers to the choice of shadowing parameterization, while the second, S, refers to the spatial dependence. Most available shadowing parameterizations ignore effects in deuterium. However, we take the proton and neutron numbers of both nuclei into account. Thus,

$$\begin{aligned}F_i^d(x,Q^2,\vec{r},z) &= \rho_d(s)f_i^N(x,Q^2) \qquad (7.38)\\ F_j^A(x,Q^2,\vec{b}-\vec{r},z') &= \rho_A(s')S^j_{\mathrm{P,S}}(A,x,Q^2,\vec{b}-\vec{r},z')f_j^N(x,Q^2)\ , \qquad (7.39)\end{aligned}$$

where $s = \sqrt{r^2+z^2}$ and $s' = \sqrt{|\vec{b}-\vec{r}|^2+z'^2}$. With no nuclear modifications, $S^j_{\mathrm{P,S}}(A,x,Q^2,\vec{r},z) \equiv 1$. The nucleon densities of the heavy nucleus are assumed to be Woods–Saxon distributions with $R_{\mathrm{Au}} = 6.38$ fm and $R_{\mathrm{Pb}} = 6.62$ fm [83]. We use the Hulthen wave function [84] to calculate the deuteron density distribution. The densities are normalized so that $\int d^2r dz \rho_A(s) = A$. We employ the MRST LO parton densities [85] for the free nucleon.

We have chosen shadowing parameterizations developed by two groups which cover extremes of gluon shadowing at low x. The Eskola *et al.* parameterization, EKS98, is based on the GRV LO [86] parton densities. Valence quark shadowing is identical for u and d quarks. Likewise, the shadowing of $\overline{u}$, $\overline{d}$ and $\overline{s}$ quarks are identical at Q_0^2. Shadowing of the heavier flavour sea, $\overline{s}$ and higher, is, however, calculated and evolved separately at $Q^2 > Q_0^2$. The shadowing ratios for each parton type are evolved to

---

[6] Author: R. Vogt

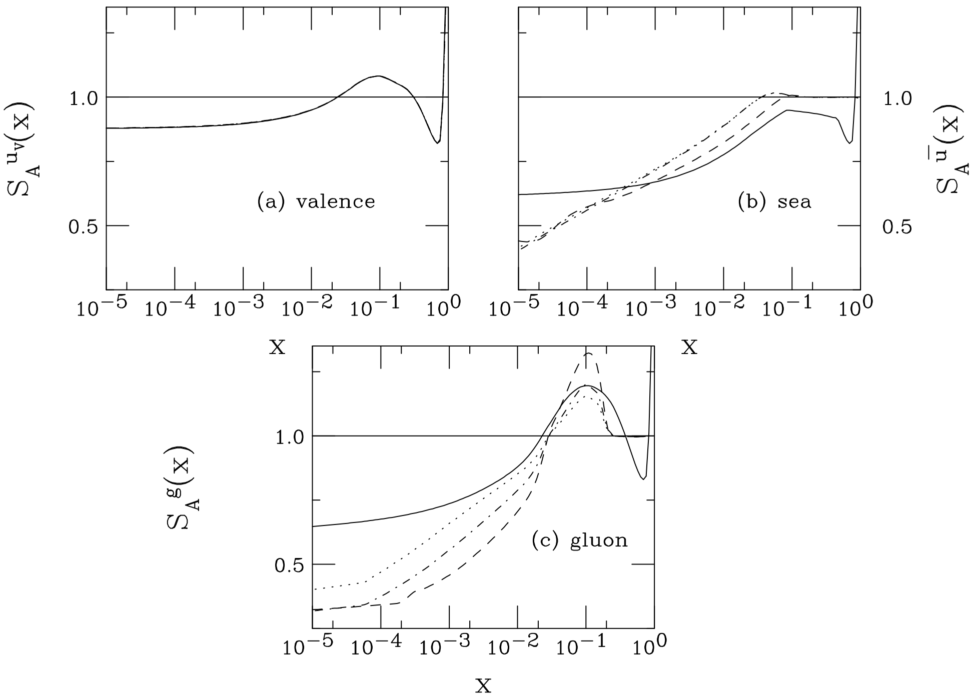

Fig. 7.15: The shadowing parameterizations are compared at the scale $\mu = 2m_c = 2.4$ GeV. The solid curves are EKS98, the dashed, FGSo, dot–dashed, FGSh, and dotted, FGSl.

LO for $1.5 < Q < 100$ GeV and are valid for $x \geq 10^{-6}$ [87, 88]. Interpolation in nuclear mass number allows results to be obtained for any input A. The parameterizations by Frankfurt, Guzey and Strikman (FGSo, the original parameterization, along with FGSh and FGSl for high and low gluon shadowing) combine Gribov theory with hard diffraction [89]. They are based on the CTEQ5M [90] parton densities and evolve each parton species separately to NLO for $4 < Q^2 < 10^4$ GeV. Although the x range is $10^{-5} < x < 0.95$, the sea quark and gluon ratios are unity for $x > 0.2$. The EKS98 valence quark shadowing ratios are used as input since Gribov theory does not predict valence shadowing. The FGSo parameterization is available for four different values of A: 16, 40, 110 and 206 while FGSh and FGSl also include $A = 197$. We use $A = 206$ for the gold nucleus with FGSo and $A = 197$ for the other parameterizations.

Figure 7.15 compares the four homogeneous ratios, $S_{\rm EKS98}$ and $S_{\rm FGS}$ for $Q = 2m_c$. The FGSo calculation predicts far more shadowing at small x and larger antishadowing at $x \sim 0.1$. The difference is especially large for gluons. At very low x, the gluon ratios for FGSo and FGSh are quite similar but, in the intermediate x regime, the FGSh parameterization drops off more smoothly. On the other hand, the FGSl parameterization levels off at a higher value of S_P^i than the other two FGS parameterizations. In the antishadowing regime, FGSh and FGSl are rather similar to the EKS98 result.

We now turn to the spatial dependence of the shadowing. We show results for a parameterization proportional to the parton path length through the nucleus [91],

$$S_\rho^j(A,x,Q^2,\vec{r},z) = 1 + N_\rho(S^j(A,x,Q^2) - 1)\frac{\int dz\rho_A(\vec{r},z)}{\int dz\rho_A(0,z)} \; . \tag{7.40}$$

where N_ρ is chosen so that $(1/A)\int d^2r dz \rho_A(s) S_\rho^j(A,x,\mu^2,\vec{b},z) = S^j(A,x,\mu^2)$. When $s \gg R_A$, the nucleons behave as free particles while in the centre of the nucleus, the modifications are larger than the average value S^j. The normalization requires $(1/A)\int d^2r dz \rho_A(s) S_{{\rm P},\rho}^j = S_{\rm P}^j$. While there are three homogeneous FGS parameterizations, only two inhomogeneous parameterizations are provided. No spatial dependence is given for FGSo, the case with the strongest gluon shadowing. We have checked the available dependencies against those calculated using $S^j_{\rm FGSo,WS}$ and $S^j_{\rm FGSo,\rho}$ and found that, at similar values of the homogeneous shadowing ratios, $S^j_{\rm FGSo,\rho}$ is quite compatible with the available FGS inhomogeneous parameterizations. Therefore, to characterize the spatial dependence of FGSo and EKS98, we use $S^j_{\rm P,\rho}$ while the given inhomogeneous parameterizations are used for FGSh and FGSl.

To implement nuclear absorption on J/ψ production in dA collisions, the production cross-section in Eq. (7.37) is weighted by the survival probability, $S^{\rm abs}$, so that

$$S^{\rm abs}(\vec{b}-\vec{s},z') = \exp\left\{-\int_{z'}^{\infty} dz''\rho_A(\vec{b}-\vec{s},z'')\sigma_{\rm abs}(z''-z')\right\} \ . \tag{7.41}$$

where z' is the longitudinal production point, as in Eq. (7.39), and z'' is the point at which the state is absorbed. If shadowing is not considered and $S^{\rm abs} = 1$, $\sigma_{{\rm d}A} = 2A\sigma_{pN}$. For $S^{\rm abs} \neq 1$, $\sigma_{{\rm d}A} = 2A^\alpha\sigma_{pN}$. The nucleon absorption cross-section, $\sigma_{\rm abs}$, depends on where the state is produced and how far it travels through nuclear matter. The effective A dependence is obtained from Eqs. (7.37) and (7.41) by integrating over z', z, and b. The contribution to the full A dependence in $\alpha(x_F)$ from absorption alone is only constant if $\sigma_{\rm abs}$ is constant and independent of the production mechanism [92]. The observed J/ψ yield includes feed down from χ_{cJ} and ψ' decays, giving

$$S^{\rm abs}_{J/\psi}(\vec{b}-\vec{s},z') = 0.58S^{\rm abs}_{J/\psi,\,{\rm dir}}(\vec{b}-\vec{s},z') + 0.3S^{\rm abs}_{\chi_{cJ}}(\vec{b}-\vec{s},z') + 0.12S^{\rm abs}_{\psi'}(\vec{b}-\vec{s},z') \ . \tag{7.42}$$

In colour singlet production, the final state absorption cross-section depends on the size of the $c\overline{c}$ pair as it traverses the nucleus, allowing absorption to be effective only while the cross-section is growing toward its asymptotic size inside the target. On the other hand, if the $c\overline{c}$ is only produced as a colour octet, hadronization will occur only after the pair has traversed the target except at very backward rapidity. We have considered a constant octet cross-section, as well as one that reverts to a colour singlet at backward rapidities. For singlets, $S^{\rm abs}_{J/\psi,\,{\rm dir}} \neq S^{\rm abs}_{\chi_{cJ}} \neq S^{\rm abs}_{\psi'}$ but, with octets, one assumes that $S^{\rm abs}_{J/\psi,\,{\rm dir}} = S^{\rm abs}_{\chi_{cJ}} = S^{\rm abs}_{\psi'}$. As can be seen in Fig. 7.16, the difference between the constant and growing octet assumptions is quite small at large $\sqrt{S}$ with only a small singlet effect at $y < -2$. Singlet absorption is also important only at similar rapidities and is otherwise not different from shadowing alone. Finally, we have also considered a combination of octet and singlet absorption in the context of the NRQCD model, see Ref. [92] for more details. The combination of nonperturbative singlet and octet parameters changes the shape of the shadowing ratio slightly. The results are shown integrated over impact parameter for the EKS98 shadowing parameterization since it gives good agreement with the trend of the PHENIX data shown later in this chapter.

Several values of the asymptotic absorption cross-section, $\sigma_{\rm abs} = 1$, 3 and 5 mb, corresponding to $\alpha = 0.98$, 0.95 and 0.92 respectively for absorption alone in e.g., beryllium and tungsten targets are shown in Fig. 7.16. These values of $\sigma_{\rm abs}$ are somewhat smaller than those obtained for the sharp sphere approximation where the relation between $\sigma_{\rm abs}$ and α can be calculated analytically: $\sigma_{\rm abs} = 16\pi r_0^2(1-\alpha)/9$. The diffuse surface of a real nucleus and the longer range of the density distribution results in a smaller value of $\sigma_{\rm abs}$ than that found for a sharp sphere nucleus.

The right-hand side of Fig. 7.16 compares the EKS98 parameterization and $\sigma_{\rm abs} = 3$ mb with the FGS parameterizations at the same value of $\sigma_{\rm abs}$. In the region that PHENIX can measure, the EKS98 and FGSl results are essentially indistinguishable. The FGSh result lies between the FGSo and EKS98 results at forward rapidity but is also quite similar to FGSh at negative rapidity.

In central collisions, the inhomogeneous shadowing is stronger than the homogeneous result. The stronger the homogeneous shadowing, the larger the inhomogeneity. In peripheral collisions, the inhomogenous effects are somewhat weaker than the homogenous results but some shadowing is still present. Shadowing persists in part because the density in a heavy nucleus is large and approximately constant except close to the surface and partly because the deuteron wave function has a long tail. We also expect

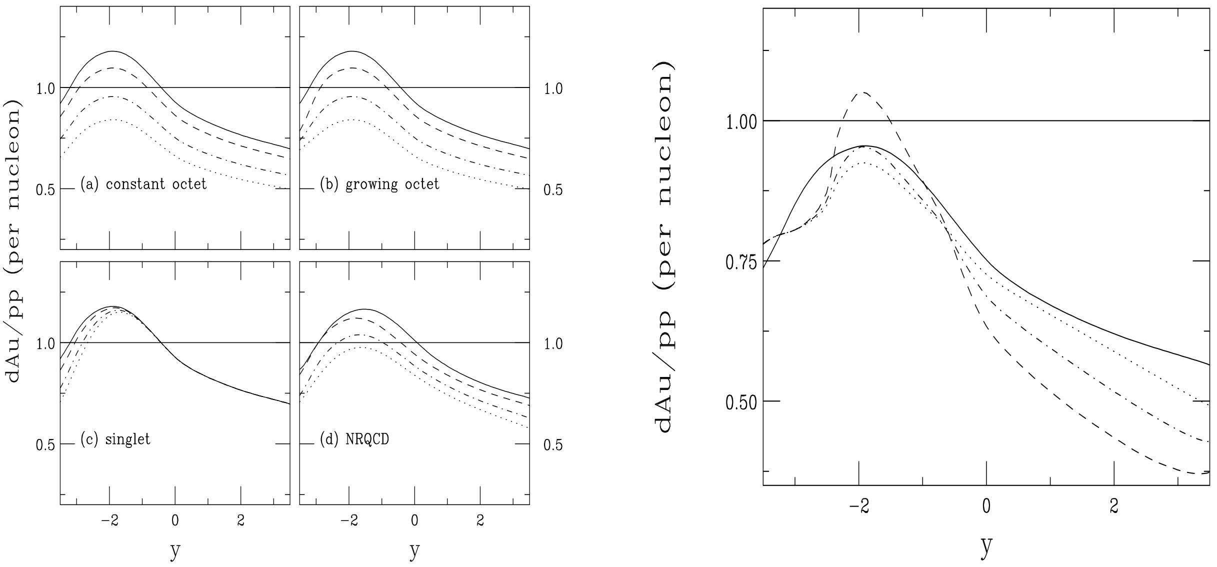

Fig. 7.16: Left-hand side: The J/ψ dAu/*pp* ratio with EKS98 at 200 GeV as a function of rapidity for (a) constant octet, (b) growing octet, (c) singlet, all calculated in the CEM and (d) NRQCD. For (a)–(c), the curves are no absorption (solid), $\sigma_{\rm abs} = 1$ (dashed), 3 (dot–dashed) and 5 mb (dotted). For (d), we show no absorption (solid), 1 mb octet/1 mb singlet (dashed), 3 mb octet/3 mb singlet (dot–dashed), and 5 mb octet/3 mb singlet (dotted). Right-hand side: The J/ψ dAu/*pp* ratio at 200 GeV for a growing octet with $\sigma_{\rm abs} = 3$ mb is compared for four shadowing parameterizations. We show the EKS98 (solid), FGSo (dashed), FGSh (dot–dashed) and FGSl (dotted) results as a function of rapidity.

absorption to be a stronger effect in central collisions. In Fig. 7.17, we show the inhomogeneous shadowing and absorption results for EKS98 and $\sigma_{\rm abs} = 3$ mb as a function of b/R_A for the dAu/*pp* ratio as a function of b relative to the minimum bias ratio on the left-hand side and the ratio dAu/*pp* as a function of the number of binary collisions, $N_{\rm coll}$, on the right-hand side. The ratios are shown for several values of rapidity to represent the behavior in the anti-shadowing (large negative y), shadowing (large positive y) and transition regions (midrapidity).

The (dAu(b)/*pp*)/(dAu/*pp*) ratios, denoted dAu(b)/dAu(ave) on the y-axis of the left-hand figure, are all less than unity for $b/R_A < 0.7$, with stronger than average shadowing and absorption, and rise above unity for large b/R_A, weaker than average shadowing and absorption. The right-hand side shows the dAu/*pp* ratios for the same rapidity values as a function of the number of collisions, $N_{\rm coll}$. The dependence of the ratios on $N_{\rm coll}$ is almost linear. We do not show results for $N_{\rm coll} < 1$, corresponding to $b/R_A > 1.3$ on the left-hand side, the point where those ratios begin to flatten out. The weakest $N_{\rm coll}$ dependence occurs where the shadowing effect itself is weakest, at $y = -2$ at RHIC, in the antishadowing region, as expected. The trends of the ratios as a function of $N_{\rm coll}$ are consistent with the PHENIX data from the north muon arm ($y = 2$) and the electron arms ($y = 0$) but the PHENIX results from the south arm ($y = -2$) are much stronger than our predictions.

Thus the combination of shadowing and absorption seems to be in good agreement with the PHENIX data from RHIC. It is more difficult to make predictions of shadowing for the CERN SPS since the average values of x at which the J/ψ is produced are much higher, $x \sim 0.16$ at $\sqrt{S_{NN}} = 20$ GeV. In this x region, the nuclear gluon shadowing ratio is either nearly crossing unity into the EMC region (EKS98) or assumed to be unity (FGS), see Fig. 7.15. Therefore we have only shown results for RHIC. At the LHC, the x values probed are significantly lower, leading to a stronger shadowing effect over all rapidity, see Ref. [91]. Combining J/ψ and Υ production results in dA collisions at RHIC and the LHC could help map out the nuclear gluon distribution in x and Q^2, both in minimum bias collisions and as a function of centrality.

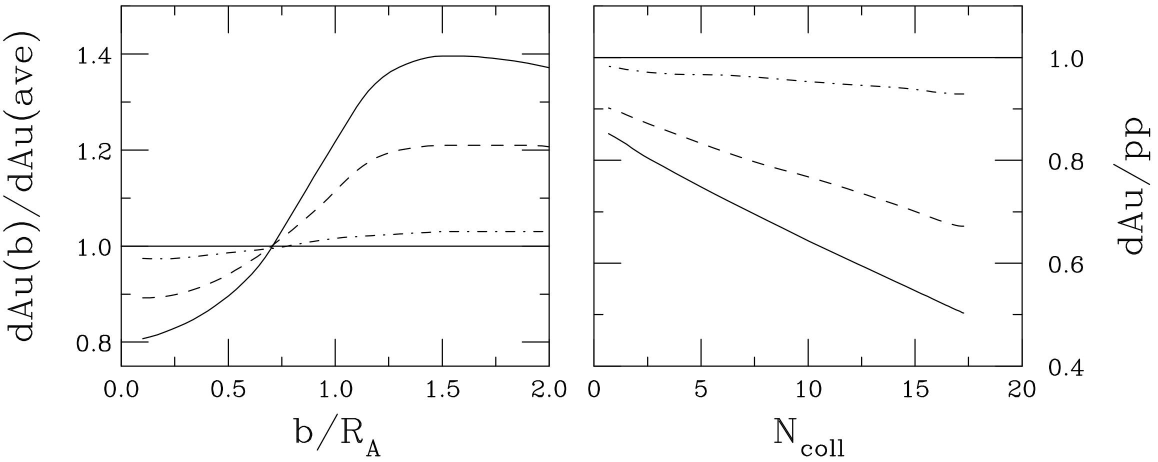

Fig. 7.17: Left-hand side: The J/ψ (dAu(b)/*pp*)/(dAu(ave)/*pp*) ratio as a function of b/R_A. Right-hand side: The ratio dAu/*pp* as a function of $N_{\rm coll}$. Results are shown for $y = -2$ (dot–dashed), $y = 0$ (dashed) and $y = 2$ (solid) at 200 GeV for a growing octet with $\sigma_{\rm abs} = 3$ mb and the EKS98 parameterization.

6 QUARKONIUM DISSOCIATION IN HOT QCD MATTER[7]

The use of heavy quarkonium suppression as a signature of deconfinement [1] requires understanding dissociation mechanisms in the confined and deconfined phases of QCD matter. In this section, we comment on the current calculations of quarkonium dissociation rates and possible ways to improve them.

In the confined hadron gas, the interactions of quarkonium are traditionally treated in a low-density approximation to the kinetic approach, where the survival probability is expressed through the quarkonium–hadron dissociation cross-sections. An overview of different approaches to calculating these cross-sections has been given previously. As discussed there, all of these approaches rely on certain assumptions and approximations, the accuracy of which is often difficult to assess *a priori*. Nonperturbative interactions of light hadrons are still beyond the reach of reliable theroretical calculations, so the hope is that the large heavy quark mass forming the quarkonium bound state can lead to simplifications.

Among the approaches discussed before, the short-distance QCD approach [2, 6] is based on the assumption that the heavy quark mass is sufficiently large, $m_q \gg \Lambda_{\rm QCD}$, and the corresponding bound state size, $R \sim 1/(m_q\alpha_s)$, is sufficiently small for interactions with light hadrons of size $\sim 1/\Lambda_{\rm QCD}$ can be treated by using the multipole, or operator product, expansion. In leading twist (or, in the more intuitive language of the QCD multipole expansion, in the leading electric dipole approximation), the cross-section is expressed through Wilson coefficients (for the leading electric dipole operator, they describe the electric polarizability of heavy quarkonium), and the gluon structure functions of light hadrons at the scale determined by the size of the $Q\overline{Q}$ state.

There are two main caveats to this approach. An analysis of the applicability of the multipole expansion shows that not only the quarkonium size should be small, $R \sim 1/(m_q\alpha_s) \ll \Lambda_{\rm QCD}$, but also the binding energy (which determines, by the uncertainty principle, the characteristic interaction time) has to be large, $\epsilon \sim m_q\alpha_s^2 \gg \Lambda_{\rm QCD}$. The latter inequality is only marginally justified for charmonium, at the borderline between the perturbative and nonperturbative regimes. The second caveat is the knowledge of the gluon structure function at large Bjorken x, corresponding to low energies and relatively small virtuality, $\sim \epsilon$. For the J/ψ, the binding energy is $\epsilon = 2M_D - M_{J/\psi} \simeq 0.64$ GeV. The gluon structure function is not well determined at such low scales. Nevertheless, at large x the gluon structure functions have to be relatively suppressed by quark counting rules which dictate at least a $\sim (1-x)^4$ suppression at $x \rightarrow 1$ since the valence quarks dominate the light hadron structure functions at large x.

---

[7] Author: D. Kharzeev

This naturally brings us to the possibility that the light quark exchanges, despite being suppressed in the heavy quark limit, become important in the dissociation of charmonium states — in fact, most of the approaches reviewed previously model such exchanges in different ways. At least in principle the picture can be clarified by a lattice calculation of the quarkonium matrix elements involving quark and gluon operators of different dimension. Such a calculation could establish a hierarchy of different mechanisms of quarkonium dissociation. It would also be important for understanding the dynamics of quarkonium production and decay. On the phenomenological side, many of the approaches can be tested in quarkonium decays, e.g., $\psi' \to \psi X$ (see e.g., Ref. [93] and references therein).

Apart from the magnitude of the quarkonium dissociation cross-section, one should also examine the validity of the low-density approximation in the kinetic approach. This approach leads to the quarkonium dissociation rate, $R = \sum_i v_i \sigma_i \rho_i$, where the sum runs over different hadron species with densities ρ_i and dissociation cross-sections σ_i and v_i are the corresponding relative quarkonium–hadron velocities. The survival probability of heavy quarkonium is then obtained by integrating over the time history of the hadron gas. For example, an isentropic longitudinal expansion yields (see e.g., Ref. [94])

$$S \sim \exp\left(- \sum_i v_i \sigma_i \rho_i \ln\left(\frac{\rho_i}{\rho_f}\right)\right) , \tag{7.43}$$

where ρ_f^i is a "freeze-out" density at which the system falls apart and ρ_i corresponds to the initial densities of the different hadron species.

Such treatment assumes the dominance of two-body interactions of the quarkonium and thus applies only at sufficiently low temperature. The dissociation process, by the uncertainty principle, takes place over a time inversely proportional to the binding energy, $\sim 1/\epsilon$. The typical time between subsequent thermal interactions at temperature T is $\sim 1/T$. The condition for the applicability of the low-density approximation is thus $\epsilon(T)/T \gg 1$. The binding energy can be modified in a thermal system and is thus a function of temperature. Lattice results presented in the previous sections, especially Section 3.3, indicate no substantial modification of the binding energy below T_c so that up to $T_c \sim 200$ MeV the ratio $\epsilon(T)/T \simeq 3$ is likely to be large enough to justify the kinetic approach.

In the deconfined phase, the original screening scenario can be seen to correspond to the opposite "weak coupling" limit of $\epsilon(T)/T \ll 1$. Indeed, the heavy quarkonium state binding energy vanishes when it is screened out of existence. The lattice results presented in Section 3 indicate that this does not happen for the J/ψ until $T \approx 1.5\,T_c$. Moreover, the previous lattice results indicate no significant change in the J/ψ mass up to these temperatures, suggesting that the weak coupling approach is not appropriate even for $T_c \leq T \leq 1.5\,T_c$. However, this does not mean that the quarkonia are not dissociated at temperatures below $1.5\,T_c$ since "ionization" of heavy quarkonia by gluons [2, 5] is still possible. An estimate of the dissociation rate in this regime was given in Ref. [7],

$$R_{\text{act}} = \frac{(LT)^2}{6\pi}\, m_q \, \exp(-\epsilon/T) \ . \tag{7.44}$$

Here L is the size of the $q\bar{q}$ system which is generally temperature dependent and can, in principle, exceed the typical hadronic size, $\sim 1/\Lambda_{\text{QCD}}$, in the deconfined phase. While this rate is moderate (at $T = 300$ MeV and $L = 1$ fm, we find $R_{\text{act}} \simeq 0.05\ \text{fm}^{-1}$), a medium with a lifetime of ≈ 10 fm can reduce the survival probability by factor of two. Thus, one cannot presently conclude from the lattice results that there is no J/ψ suppression in the deconfined phase below $1.5T_c$. A conclusive answer can be given by lattice calculations once a reliable extraction of the J/ψ width becomes possible.

Once the weak coupling limit of $\epsilon(T)/T \ll 1$ is reached, dissociation occurs very rapidly with a rate [7]

$$R_{\text{act}} = \frac{4}{L}\sqrt{\frac{T}{\pi m_q}} \ . \tag{7.45}$$

This expression is easy to understand once we recall that the thermal velocity of a free particle in three dimensions is $v_{\rm th}(T) = 4\sqrt{T/\pi m_q}$ where we recover the classical high-temperature limit for the thermal activation rate

$$R_{\rm act} = \frac{v_{\rm th}(T)}{L} \ . \tag{7.46}$$

An estimate of Eq. (7.45) gives a large rate, $R_{\rm act} \sim$ 1/fm suggesting that once the binding energy of quarkonium becomes small compared to the temperature, dissociation occurs very rapidly and should lead to strong suppression, as envisioned in the original scenario [1].

7 SECONDARY CHARMONIUM PRODUCTION AND CHARM–QUARK COALESCENCE[8]

In recent years, a new element has been added to charmonium production in heavy-ion collisions with the realization that $c\bar{c}$ bound states might be recreated in later stages of the reaction. In Refs. [95–99] secondary charmonium production was evaluated in the statistical model for hadron production, motivated by the success of this framework in the description of light hadron species [100]. Whereas in Ref. [95] the J/ψ abundance was calculated simply in terms of its thermal density at the hadronization temperature, T_c, yielding fair agreement with NA50 data [101, 102] at the SPS, Refs. [96–99] included the notion that the (rather heavy) charm quarks are exclusively produced in primordial (hard) nucleon–nucleon (NN) collisions. This constraint is implemented by introducing a charm–quark fugacity, $\gamma_c \equiv \gamma_{\bar{c}}$, to match the primordial number of $c\bar{c}$ pairs, $N_{c\bar{c}}$, to the total (hadronic) charm content in the fireball at hadronization,

$$N_{c\bar{c}} = \frac{1}{2} N_{\rm op} \, \frac{I_1(N_{\rm op})}{I_0(N_{\rm op})} \ + \ V_{FB}(T) \, \gamma_c(T)^2 \sum_{\Psi} n_\psi(T) \ . \tag{7.47}$$

Here $N_{\rm op} = V_{FB}(T) \, \gamma_c \, \sum_C n_C(T, \mu_B)$ and $C = D, \overline{D}, D^*, \overline{D}^*, \Lambda_c \ldots$, runs over all known open charm hadrons, V_{FB} denotes the (centrality-dependent) hadronic fireball volume covering an appropriate range in rapidity and $I_{0,1}$ are modified Bessel functions. The number of charmonium states ($\Psi = \eta_c$, J/ψ, $\psi' \ldots$) produced by "statistical coalescence" then follows as

$$N_\Psi^{\rm eq}(T, \gamma_c) = V_{FB}(T) \, d_\Psi \, \gamma_c^2 \int \frac{d^3q}{(2\pi)^3} f^\psi(m_\psi; T) \tag{7.48}$$

where d_Ψ is the spin-degeneracy. The statistical approach correctly reproduces the ψ' to J/ψ ratio [103] for sufficiently central Pb+Pb collisions ($N_{\rm part} \geq$ 200) at the SPS. However, to describe the absolute J/ψ and ψ' numbers in terms of statistical coalescence alone (implying that all primordially produced charmonium states are suppressed), an enhancement of total charm production over the standard expectation from NN collision-scaled pp cross-sections by a factor of $\sim$ 3 is necessary. This requirement, as well as the assumption of complete suppression of primordial charmonia, has been relaxed in the "two-component model" of Refs. [104, 105] where statistical charmonium production has been combined with a primordial component subject to suppression in both Quark–Gluon Plasma (QGP) and hadron gas phases. As a result, it has been found that the (moderately) suppressed primordial J/ψ component prevails as the major yield at SPS energies, whereas statistical recombination is the dominant source in central Au+Au collisions at RHIC, with interesting consequences for the excitation function, cf. the left-hand side of Fig. 7.18.

As discussed in Section 3, an important new insight from QCD lattice calculations is that low-lying charmonium states survive as resonance/bound states with finite width in the QGP up to temperatures of about $1.5 - 2\,T_c$. This implies that these charmonium states can be formed not only at the hadronization transition, but also in the QGP. Of course, at the same time, dissociation reactions are operative, and the evolution of the J/ψ number should be described by kinetic theory within a Boltzmann equation. In

---

[8] Author: R. Rapp

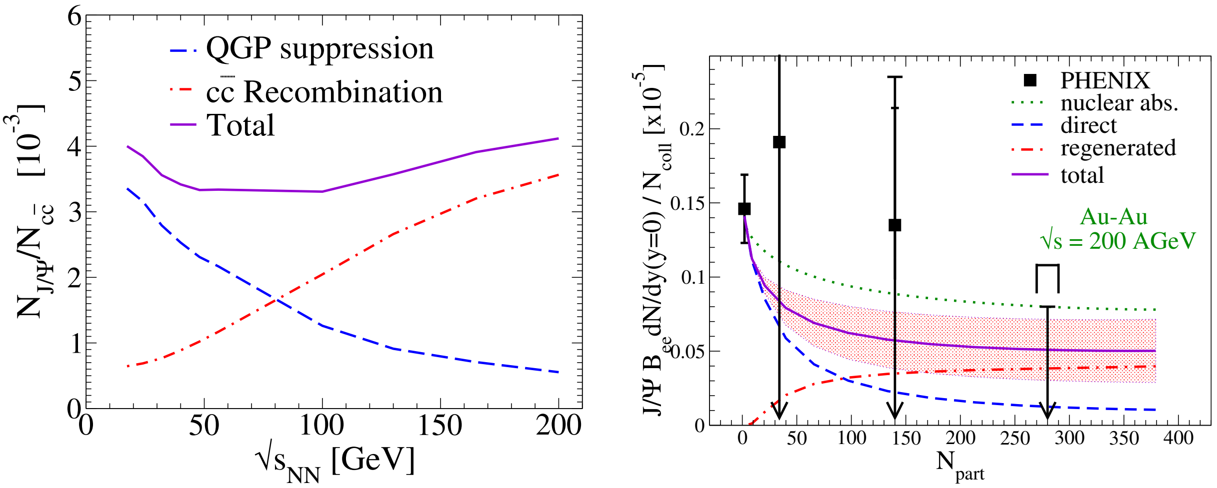

Fig. 7.18: Left-hand side: excitation function of the ratio of J/ψ's over $c\bar{c}$ pairs in central heavy-ion collisions ($N_{\rm part}$ = 360) from SPS to RHIC energies [104, 105] for the J/ψ yield from quark gluon plasma suppressed primordial production (dashed), secondary J/ψ production from $c\bar{c}$ coalescence (dot–dashed) and the sum (solid). Right-hand side: Centrality dependence of the J/ψ yield, normalized to the number of primordial NN collisions, in Au+Au collisions at RHIC within a kinetic theory framework including in-medium effects on both open and hidden charm states [108]. We show J/ψ suppression with only the loss term in Eq. (7.50) (dashed), secondary J/ψ production (dot–dashed), primordial J/ψ's subject to nuclear absorption only (dotted) while the band around the solid line, representing the full solution of the rate equation, indicates the uncertainty induced by varying the in-medium masses of open-charm hadrons.

simplified form, the latter can be written as

$$\frac{dN_\Psi}{d\tau} = -\hat{\Gamma}_D\, N_\Psi + \hat{\Gamma}_F\, N_c\, N_{\bar{c}} \tag{7.49}$$

where $\hat{\Gamma}_D$ and $\hat{\Gamma}_F$ are the charmonium dissociation and formation rates respectively. The inclusion of the backward reaction in inelastic charmonium interactions such as, $J/\psi + X_1 \leftrightharpoons X_2 + c + \bar{c}\,(D + \overline{D})$, is, in fact, mandated by the principle of detailed balance. A key question is then under which conditions regeneration becomes quantitatively relevant. First, the equilibrium number of J/ψ mesons should be comparable to initial production (after nuclear absorption). While at the SPS, where $N_{c\bar{c}} \simeq 0.2$ in central Pb+Pb collisions (based on binary NN collision scaling), this is not the case, the situation is more favorable at RHIC, where, according to current measurements [106, 107], $N_{c\bar{c}} \simeq 15 - 30$ in central Au+Au collisions. Also note that the higher QGP temperatures at RHIC presumably lead to stronger suppression of the primordial component. Second, the amount of regeneration depends on the momentum distributions of charm quarks. Thus, if the latter are in thermal equilibrium (along with gluons and light quarks) and as long as a well-defined J/ψ (resonance) state persists, Eq. (7.49) takes a particularly simple and instructive form,

$$\frac{dN_\Psi}{d\tau} = -\Gamma_\Psi(T)\left[N_\Psi - N_\Psi^{\rm eq}(T,\gamma_c)\right] \ . \tag{7.50}$$

An important point here is that the key ingredients to Eq. (7.50) are rather directly related to equilibrium in-medium properties of charm(onium) states, i.e., quantities which can be extracted from lattice QCD: (i) the reaction rate $\Gamma_\Psi(T)$ is the (inelastic) width of the Ψ spectral function; (ii) the equilibrium charmonium abundance, $N_\Psi^{\rm eq}$, given by Eq. (7.48), depends on the in-medium charmonium mass and, via γ_c in Eq. (7.47), on the spectrum of open-charm states (including their in-medium masses). A recent calculation including current knowledge from lattice QCD has been performed in Ref. [108]; results for RHIC are shown on the right-hand side of Fig. 7.18, indicating appreciable sensitivity to the in-medium open-charm threshold, mostly due to its impact on N_Ψ^{eq}. This investigation has also shown that most of the secondary J/ψ production occurs through resonance formation in the QGP. At full RHIC energy, relative chemical equilibrium is reached close to the hadronization temperature and frozen thereafter due to small reaction rates in hadronic matter, implying approximate agreement with the limiting case of statistical coalescence models applied at T_c, as discussed above.

The sensitivity of secondary production to the charm quark momentum distributions (i.e., deviations from thermal equilibrium) has been addressed in Refs. [109, 110], as well as in recent transport simulations [111, 112]: although the use of, e.g., primordial (perturbative QCD) charm quark distributions reduces the regenerated yield appreciably, it still remains significantly larger than expectations based on suppression scenarios alone. Measurements of elliptic flow of D-mesons at RHIC, testing their (early) thermalization, will therefore impose important constraints on models for charmonium regeneration. Similarly, since in coalescence approaches $N_\Psi^{\mathrm{eq}} \propto N_{c\bar{c}}^2$ (cf. Eqs. (7.47) and (7.48)), an accurate measurement of open-charm production will be essential for reliable predictions of charmonium yields and spectra. Finally, it will be of great interest to extend both experimental and theoretical investigations to the bottomonium sector.

8 QUARKONIUM PRODUCTION IN NUCLEAR COLLISIONS[9]

8.1 Charmonium suppression at the CERN SPS

The experimental study of charmonium production in collisions of light and heavy ions at ultrarelativistic energies was carried out at the CERN SPS over 15 years (1986–2000) by experiments NA38 (see Refs. [113, 114] for initial results and [115, 116] for the most recent ones) and NA50 (see Refs. [50, 117–120]). It is continuing with experiment NA60, taking data in 2003 and 2004.

In addition, NA51 provided a reference measurement of charmonium production in pp and pd collisions [121] while proton–nucleus, pA, reference data were collected by NA38 [116, 122] and, with higher statistics, by NA50 [123, 124].

The SPS energies, between 158 and 450 GeV per nucleon in a fixed target configuration, are well suited for charmonium studies since the J/ψ production cross-section in the forward hemisphere ($x_F >$ 0) in proton–proton interactions is between 50 and 100 nb/nucleon (see e.g., Ref. [125]), well above threshold. The high intensity experimental area at the SPS provides beam rates of about 10^7 Pb ions/s and 10^9 protons/s which, with a branching ratio $J/\psi \rightarrow \mu^+\mu^-$ of about 6% and a typical acceptance of 15%, resulted in samples of several tens of thousand of J/ψ collected for a given system. The statistics collected (see Tables 7.1 and 7.2) made it possible to perform detailed studies of J/ψ and ψ' production as a function of centrality in ion–ion collisions. The centrality was evaluated via the transverse energy, E_T, by NA38, as well as via the forward energy in the zero degree calorimeter, E_{ZDC}, and the charged multiplicity, N_{ch} by NA50.

The experimental program at the CERN SPS was developed in successive phases. At first, the pioneering experiment NA38 [113] collected data with light ions (oxygen and sulphur) at 200 GeV/nucleon and with proton beams at 450 GeV, using the NA10 dimuon spectrometer and an electromagnetic calorimeter as a centrality detector. Then, the second generation experiment NA50 [117] studied J/ψ production in lead–lead collisions at 158 GeV/nucleon with new or improved centrality detectors, and in proton–nucleus collisions with much higher statistics relative to NA38. Finally, experiment NA60 collected data with indium–indium collisions at 158 GeV/nucleon and proton–nucleus collisions at 400 GeV with a new silicon vertex spectrometer and a beam tracker (see next section).

In order to compare the hard production of charmonium states in different collisions ranging from pp to Pb+Pb, it is appropriate to define the cross-section per nucleon–nucleon collision, obtained by

---

[9] Section coordinator: M. Rosati; Authors: C. Lourenço, L. Ramello, M. Rosati, E. Scomparin

Table 7.1: Summary of proton–nucleus data collected by NA50.

Years	1996–1998	1998–2000	2000
Energy (GeV/nucleon)	450	450	400
Target thickness L/λ_I	26–39%	26–39%	26–39%
Targets	Be, Al, Cu, Ag, W	Be, Al, Cu, Ag, W	Be, Al, Cu, Ag, W, Pb
Beam intensity (p/s)	$(4-13)\times 10^8$	$(0.8-2.5)\times 10^8$	$(9-13)\times 10^8$
J/ψ ($\times 10^3$)	350–800	80–180	38–68

Table 7.2: Summary of S+U data and Pb+Pb data collected by NA38 and NA50.

Year	1992	1995	1996	1998	2000
Energy (GeV/nucleon)	200	158	158	158	158
Target thickness L/λ_I	20.5%	17%	30%	7%	9.3%
Beam–Target	S+U	Pb+Pb	Pb+Pb	Pb+Pb	Pb+Pb
Beam intensity (ions/5 s)	8×10^7	3×10^7	5×10^7	5.5×10^7	7×10^7
J/ψ ($\times 10^3$)	113	50	190	49	129

dividing the measured cross-section by the product of the mass numbers, AB, of the colliding nuclei. In the study of centrality, the measured Drell–Yan cross-section can replace AB since it has been verified experimentally (see e.g., Refs. [74, 118]) that the Drell–Yan cross-section is proportional to the number of nucleon–nucleon collisions.

The nuclear dependence of the charmonium cross-section is often parametrized as $\sigma_{pA} = \sigma_{pp}A^{\alpha}$, where $\alpha = 1$ is expected for a hard process in the absence of nuclear absorption effects. A more accurate description, valid also for light targets, is provided by the Glauber formalism [126]. A detailed description of such formalism applied to both pA and nucleus–nucleus collisions is given in Ref. [94]. The distribution of matter inside nuclei is described by 2-parameter or 3-parameter Woods–Saxon distributions from a compilation of electron scattering measurements [127]. When comparing the centrality evolution of different systems, a useful variable is the average path of the $c\bar{c}$ pair through nuclear matter, denoted by L.

The first NA38 results, obtained with 200 GeV/nucleon oxygen and sulphur beams, revealed [113, 114] that J/ψ production is suppressed in ion collisions, both relative to pU and as a function of the transverse energy, E_T. However, it was later found that the suppression pattern observed in S+U collisions was compatible with the extrapolation of the trend observed in pA collisions. NA38 then collected a significantly larger sample of S+U events (see Table 7.2), obtaining [115] absolute cross-sections for J/ψ, $B\sigma_{\psi} = 7.78 \pm 0.04 \pm 0.62$ μb, ψ', $B\sigma_{\psi'} = 59.1 \pm 6.2 \pm 4.7$ nb, and Drell–Yan in the mass window $2.9 < M < 4.5$ GeV, $\sigma_{\mathrm{DY}} = 310 \pm 10 \pm 25$ nb. Comparing the suppression pattern of the two resonances it was found that the ψ' is more suppressed than the J/ψ by at least a factor of two, even more so for central collisions. A global study of this result together with pp and pd results from NA51 [121] and pA results from NA38 [122] revealed (see Ref. [116], in particular Fig. 5) that J/ψ production exhibits a continuous decreasing pattern from pp to S+U reactions (including the centrality dependence observed in S+U interactions) which can be accounted for by normal nuclear absorption. On the other hand, the ψ' showed extra suppression in S+U interactions. Since the ψ' state is very loosely bound, it can be broken into a pair of open charm mesons by purely hadronic interactions, independent of whether the produced matter is confined or deconfined.

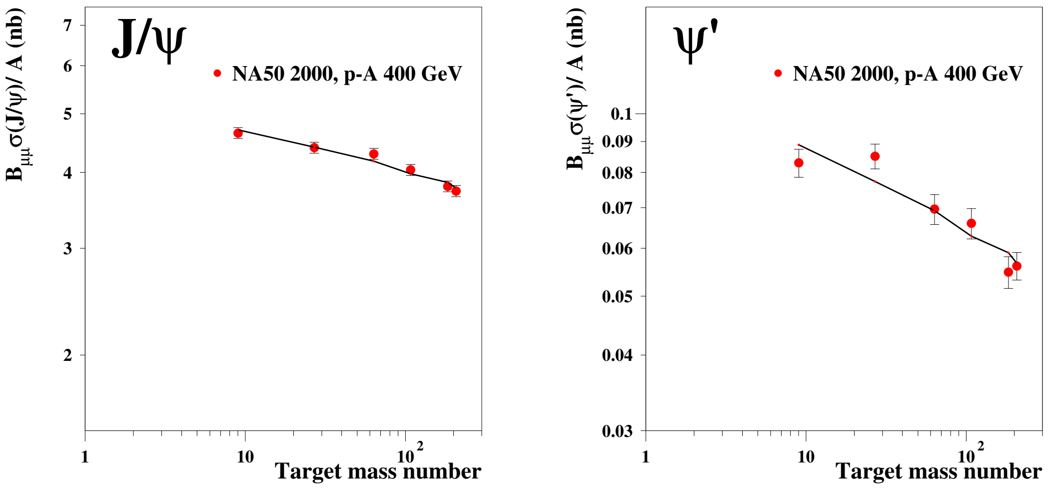

Fig. 7.19: The J/ψ (left) and ψ' (right) cross-sections in proton–nucleus collisions with six different targets at 400 GeV, measured by NA50, together with the result of the Glauber fits.

The understanding of the reference proton–nucleus data improved dramatically thanks to recent high statistics measurements by NA50, see Table 7.1. Figure 7.19 (see Ref. [74]) shows the absolute J/ψ and ψ' cross-sections, multiplied by the branching ratio to dimuons and divided by the target mass number A for the most recent pA data collected at 400 GeV. A fit using the Glauber formalism [94, 126], more accurate than the usual A^{α} parametrization, leads to absorption cross-sections $\sigma^{\psi}_{\text{abs}} = 4.2 \pm 0.5$ mb and $\sigma^{\psi'}_{\text{abs}} = 9.6 \pm 1.6$ mb. A difference between the J/ψ and ψ' absorption cross-sections is observed already in proton–nucleus collisions, thanks to higher statistics and improved systematics relative to NA38.

A more precise picture of normal nuclear absorption is obtained by combining the absolute cross-sections with the (J/ψ)/Drell–Yan ratios at all available beam energies. Using, in addition to the 400 GeV p–A data, also the NA50 data collected with a 450 GeV proton beam [123, 124] and the NA51 pp and pd results [121], a simultaneous Glauber fit gives [74] $\sigma^{\psi}_{\text{abs}} = 4.3 \pm 0.3$ mb. The NA38 S+U data at 200 GeV/nucleon have been reanalysed with the most recent techniques. By fitting the reanalyzed data to a centrality-dependent Glauber calculation for six different centrality regions (see Fig. 7.20 left), $\sigma^{\psi}_{\text{abs}} = 7.3 \pm 3.3$ mb is obtained, statistically compatible with the pA cross-section. A global fit to pp, pd, pA and S+U data, with separate normalizations for the three different (energy and rapidity) kinematical conditions, leads to $\sigma^{\psi}_{\text{abs}} = 4.3 \pm 0.3$ mb (see Fig. 7.20 right). An extrapolation from the 200 GeV/nucleon S+U to the 158 GeV/nucleon Pb+Pb kinematical conditions is then made in order to obtain the normal absorption curve against which the Pb+Pb results are compared.

The analysis of the Pb+Pb data collected in 1995, 1996 and 1998 (see Table 7.2) showed [117, 118] that J/ψ production, relative to Drell–Yan, is anomalously suppressed with respect to the normal nuclear absorption pattern. This integrated result was complemented by detailed studies of the J/ψ suppression pattern as a function of collision centrality [50, 119, 120], determined from E_T and E_{ZDC}, which suggests that this extra suppression sets in for semi-central collisions, with the transition occurring over a rather small range of centrality values. The suppression pattern, showing a departure from normal absorption and then no saturation at high E_T, is currently interpreted in the quark–gluon plasma scenario as the sequential suppression of two $c\bar{c}$ states, first the χ_c and then the J/ψ.

A more detailed analysis of Pb+Pb data revealed that the peripheral centrality data was affected by a considerable admixture of Pb–air interactions, especially in the multi-target configuration used in

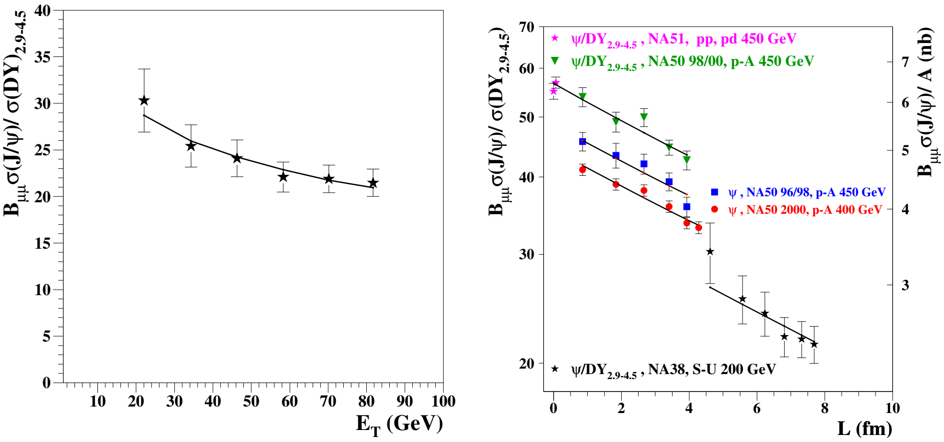

Fig. 7.20: Left-hand side: the (J/ψ)/Drell–Yan ratio as a function of centrality (determined by E_T) in S+U collisions. Right-hand side: the (J/ψ)/Drell–Yan as a function of L for several systems.

1996. Therefore, more data were collected by NA50 in 2000 with a single target under vacuum. The 2000 Pb+Pb J/ψ result is shown on the left-hand side of Fig. 7.21 together with the absorption curve derived from the analysis presented in Fig. 7.20. The departure from the ordinary nuclear absorption is still, in the new data set, a striking feature. The Pb+Pb data are compared to other systems on the right-hand side of Fig. 7.21.

A new result on ψ' production, recently obtained [75] from the 1998 and 2000 Pb+Pb data samples, analysed with the most recent procedures, is presented in Fig. 7.22. The left-hand side shows the relative suppression of the two $c\bar{c}$ bound states for several systems ranging from pBe to Pb+Pb, as a function of the product AB. As indicated above, the ψ' is more absorbed than the J/ψ already in pA collisions. Furthermore, a stronger ψ' suppression relative to the J/ψ is observed for the heavier S+U and Pb+Pb systems. On the right-hand side, ψ' suppression relative to Drell–Yan is presented as a function of centrality, expressed by the path length L. The ψ' suppression is the same in S+U and Pb+Pb interactions as a function of centrality and about three times stronger than in pA interactions.

In conclusion, experiments NA38, NA50 and NA51 provided valuable information on J/ψ and ψ' production with proton and ion beams at the SPS fixed target energies. A synthesis of the main result, the different suppression patterns of the two $c\bar{c}$ states, is presented in Fig. 7.23.

8.2 Recent studies of charmonium production in heavy-ion collisions at the SPS

Charmonium physics in ultrarelativistic nucleus–nucleus collisions is now being studied at the SPS by NA60. The experimental apparatus includes the muon spectrometer already used by NA50 and a vertex spectrometer, based on silicon pixel detectors, that allows an accurate determination of primary and secondary interaction vertices with a resolution better than 50 μm. By matching the muons measured in the muon spectrometer to tracks in the pixel telescope, simultaneously using coordinate and momentum information, it is possible to overcome the uncertainties introduced by the multiple scattering and energy loss fluctuations induced by the 5.5 m long hadron absorber positioned in front of the muon spectrometer. The consequent improvement in dimuon mass resolution is extremely impressive, and reaches a factor $\sim$ 4 for low mass dimuons ($M < 1$ GeV), where multiple scattering is quantitatively more important. In the charmonia mass region, NA60 reaches a mass resolution of $\approx$ 70 MeV as opposed to $\approx$ 105 MeV in NA50, particularly important for ψ' studies.

In 2003, NA60 collected more than 230 million dimuon triggers in In+In collisions at 158 GeV/nucleon. The choice of Indium, an intermediate mass nucleus, is particularly interesting for the study of

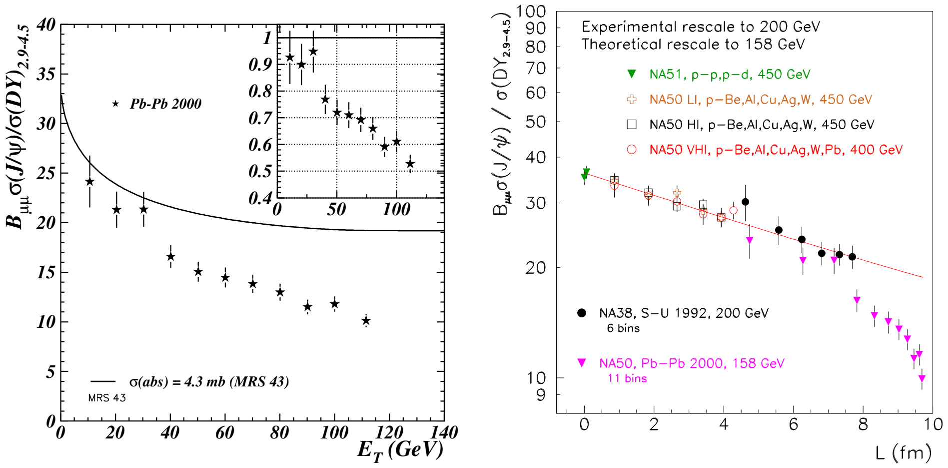

Fig. 7.21: Left-hand side: the (J/ψ)/Drell–Yan ratio as a function of centrality in Pb+Pb collisions at 158 GeV/nucleon. Right-hand side: the (J/ψ)/Drell–Yan ratio for several systems, from *pp* to Pb+Pb, as a function of L.

the anomalous J/ψ suppression observed by NA50 in Pb+Pb collisions. The onset of the anomalous J/ψ suppression occurs in semiperipheral Pb+Pb events, a region with potentially important systematic uncertainties due to the presence of out-of-target events. For the lighter In+In system, the anomaly should show up for comparatively more central events, thereby confirming this effect in a region where systematics are easier to control.

Furthermore, other useful insights into the suppression mechanisms can be obtained by studying the J/ψ yield as a function of centrality for both In+In and Pb+Pb, plotting the results as a function of centrality using several variables such as L, the thickness of nuclear matter traversed by the charmonium state, the number of participant nucleons, N_{part}, and the energy density, ϵ. In this way it may become possible to precisely identify the centrality variable that governs the anomalous suppression and, therefore, its origin. In particular, one could distinguish between the thermal (QGP) and geometrical (percolation) phase transitions, both resulting in the suppression of J/ψ production but as a function of different variables and with different thresholds in collision centrality.

Figure 7.24 shows the ratio between the J/ψ and the Drell–Yan production cross-sections measured in In–In collisions, in three centrality bins, either as a function of L (the distance of nuclear matter crossed by the J/ψ mesons after production) or N_{part}. On the right panel the J/ψ suppression pattern is divided by the normal nuclear absorption curve, defined by p–nucleus data. The J/ψ and Drell–Yan cross-sections are evaluated in the phase space window $2.92 < y_{\text{lab}} < 3.92$ and $-0.5 < \cos\theta_{\text{CS}} < 0.5$, where θ_{CS} is the polar decay angle of the muons in the Collins–Soper reference system. The Drell–Yan value is given in the 2.9–4.5 GeV/c^2 mass window. We see that, unlike what happens in the S–U collisions studied by NA38, the J/ψ production is suppressed in indium–indium collisions beyond the normal nuclear absorption. When the J/ψ over Drell–Yan ratio is plotted as a function of N_{part} the indium data points seem to agree with the suppression pattern measured in Pb–Pb. The two sets of data points *do not* overlap as a function of L. To clarify the origin of the anomalous J/ψ suppression, the statistical significance of the results must be increased and reference processes alternative to Drell–Yan are presently under study in NA60. Also the study as a function of the energy density is in progress.

8.3 Charmonium production in proton–nucleus collisions at 158 GeV

The NA60 experiment was proposed to clarify several physics questions resulting from specific experimental measurements made by previous SPS experiments, including the observation that J/ψ production

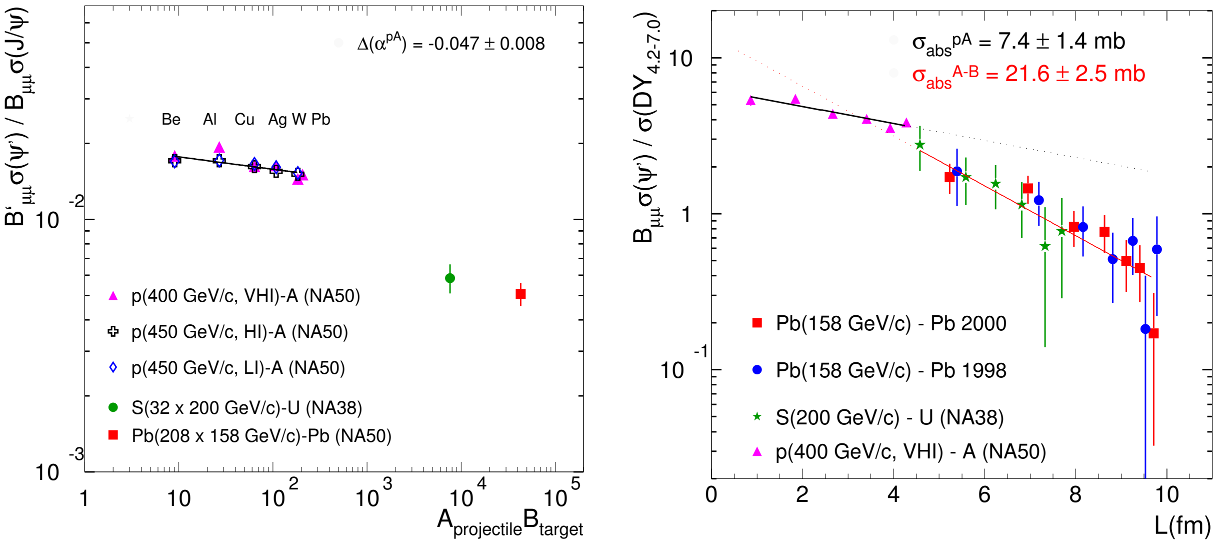

Fig. 7.22: Left-hand side: the ratio of ψ' to J/ψ in different collision systems as a function of AB. Right-hand side: the (ψ')/Drell–Yan ratio as a function of L.

is suppressed in heavy-ion collisions with respect to the yields extrapolated from proton–nucleus data. The NA60 In+In measurements have been made at the same energy as Pb+Pb to minimize systematic uncertainties in their comparison. However, to fully interpret the J/ψ production patterns observed in nuclear collisions as a function centrality, it is crucial to have a proper "reference baseline", to extract any "anomalous behaviour" specific to heavy ion collisions. Only with such a "normal nuclear absorption" curve we can look for signatures of quark–gluon plasma formation in the heavy-ion data. However, this reference has so far been based on proton–nucleus data collected at a rather different beam energies, 450 GeV (and a small data sample at 400 GeV). Figure 7.25 summarizes those results.

The NA50 collaboration has also made use of the S+U data set collected by NA38 at 200 GeV. While it is certainly true that the rescaling from 200 to 158 GeV is much more robust than from 450 GeV, this data set has been used making the extra assumption that there is nothing new happening between the proton–nucleus reference and the S+U collision system. We know, however, that the ψ' resonance is considerably suppressed in S+U collisions with respect to its "normal nuclear absorption" pattern, established by exclusively studying proton–nucleus interactions. Therefore, even though this assumption is based on the compatibility of the results obtained from p, O and S induced reactions, it remains nevertheless a questionable assumption which must be verified with a precise measurement. This problem does not prevent us from directly comparing the In and Pb data since both sets were taken at exactly the same energy, 158 GeV. However, the interpretation of the measured pattern in terms of "new physics" requires the comparison to an "expected" pattern, based on a purely conventional "normal nuclear absorption". Presently, this comparison is mostly limited by the accuracy with which we can rescale the measured proton–nucleus points to the energy and kinematical domain of the heavy-ion measurements.

In 2004 the NA60 experiment has collected three days of data to study J/ψ production in proton–nucleus collisions with a high intensity 158 GeV primary proton beam. This data sample will allow us to directly establish a normal nuclear absorption reference based on proton induced interactions, minimizing systematic uncertainties and model-dependent assumptions.

The normal nuclear absorption pattern can be determined by comparing the measured J/ψ production cross-sections (or production yield with respect to high mass Drell–Yan) in proton–nucleus collisions for several target nuclei with a calculation based on the Glauber scattering formalism. It can be approximately expressed as an exponential function of the average length of nuclear matter the produced

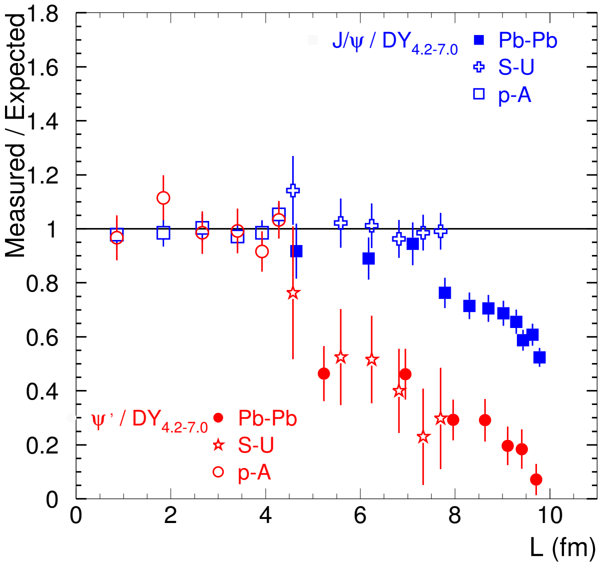

Fig. 7.23: The Measured/Expected ratio for J/ψ and ψ' in pA, S+U and Pb+Pb collisions at the CERN SPS.

charmonium state needs to traverse to get out of the nucleus, $\sigma_{pA}(L) = \sigma_{pp}\exp(-\rho_A L \sigma_{\text{abs}})$. This calculation uses the Woods–Saxon nuclear density profiles. We can describe the measured data points by adjusting a normalization coefficient and the absorption cross-section, σ_{abs}, to get the absorption rate.

A priori, it may very well happen that the absorption cross-section depends on the energy of the interactions. In fact, it is well known that the NA50 experiment measured stronger J/ψ absorption than E866, for the same x_{F} range (close to 0). The main difference is the proton beam energy: 800 GeV in E866 and 450 GeV in NA50. Expressed in terms of the simple A^{α} parameterization, E866 gives values of α around 0.95 while NA50 gives values closer to 0.92. If the difference is due to the change in energy, we can easily imagine that at 158 GeV, the energy of the In and Pb beams, the value of α would be even smaller, equivalent to having a higher normal nuclear absorption cross-section. Unfortunately, the energy is not the only difference between NA50 and E866 and the change of α is not understood well enough to extrapolate to lower energy. For instance, the J/ψ mesons produced at 800 GeV have, on average, higher values of p_T and the value of α increases with p_T (Cronin effect).

Figure 7.26 shows the ratio between the J/ψ and Drell–Yan (in the mass range $2.9 < M < 4.5$ GeV) production cross-sections, as a function of L, for the proton–nucleus and S+U data, collected either at 450 or 200 GeV. The fit of the 400 and 450 GeV data points leads to $\sigma_{\text{abs}} = 4.3 \pm 0.5$ mb. On the left-hand side, we show what happens if we impose this σ_{abs} when fitting the 200 GeV data points, leaving the normalization of the curve free. On the right-hand side the 200 GeV data were independently fitted, resulting in $\sigma_{\text{abs}} = 6.8 \pm 1.8$ mb. The dotted lines indicate the uncertainty band, including both the errors on σ_{abs} and on the normalization. These values indicate that the absorption cross-section seems to increase when the collision energy decreases, a tendency that would match the 800 GeV data collected by E866.

Besides the possible change of σ_{abs} from 450 to 158 GeV, another very important unknown is the normalization of the absorption curve at 158 GeV, needed to compare the In and Pb data. In principle, the energy dependence of the J/ψ production cross-section should be calculable so that it would be possible to estimate the normalization at 158 GeV from the 450 GeV data. In practice, however, such calculations are not unique and are severely limited by nonperturbative contributions. The accuracy we need can only be obtained from a measurement made at the same energy and in the same experiment that measured the nuclear data.

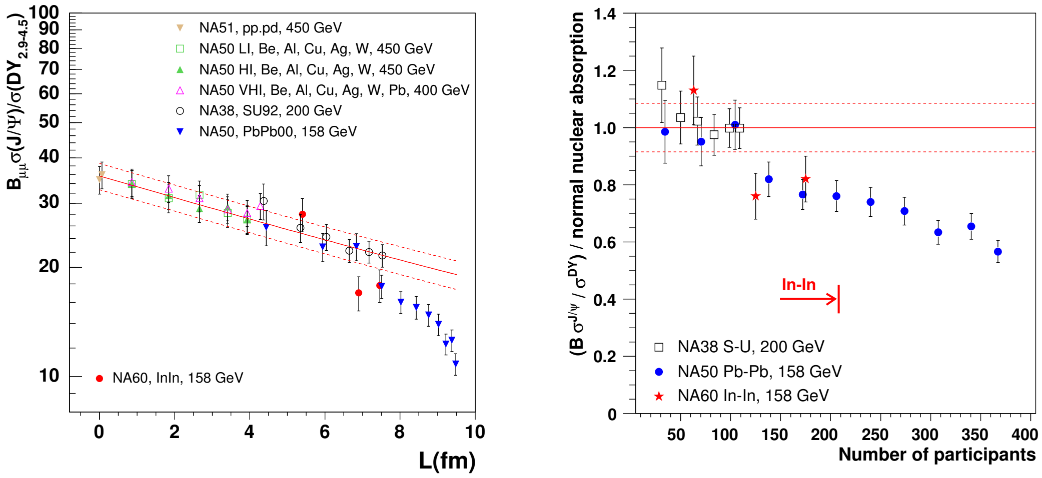

Fig. 7.24: The J/ψ suppression pattern versus L (left) and, after dividing by the normal nuclear absorption curve, versus N_{part} (right), including the NA60 indium–indium measurements.

Even if we assume that σ_{abs} is not energy dependent and use the value determined at 400 and 450 GeV, $\sigma_{\text{abs}} = 4.3 \pm 0.5$ mb, to build the nuclear absorption curve at 158 GeV, we still need to determine its normalization. The NA50 collaboration has taken the normalization value determined at 200 GeV, assuming that the S+U and pA data share the same σ_{abs} value, obtain the normalization at 158 GeV using the so-called "Schuler parameterization". This procedure has the big advantage that the energy difference is very small, thereby reducing the importance of the uncertainties on the energy dependence. However, it has the disadvantage of imposing the extra assumption that the σ_{abs} value is the same in proton–nucleus and S+U collisions (besides ignoring any energy dependence of σ_{abs}). If we accept that the S+U data does not need to be described by the σ_{abs} value derived from the pA data, we must start from the 450 GeV normalization and scale it down to 158 GeV, requiring accurate knowledge of the energy dependence of J/ψ production.

Since we are comparing data expressed as the ratio between the J/ψ and Drell–Yan cross-sections, the energy dependence of the Drell–Yan process also needs to be accurately known in the same phase space window to evaluate the scaling factor needed to normalize the 158 GeV data from 450 GeV. Different parton distribution functions may give somewhat different energy dependences although the calculations are more robust. Unfortunately, the statistics collected in a few days will not allow us to verify the energy dependence of the Drell–Yan production cross-section.

It should be clear by now that it is crucial to measure the J/ψ absolute production cross-section in proton–nucleus collisions at 158 GeV, if we want to fully understand J/ψ suppression. Such measurements started in 2004 but should be repeated in the near future, with much higher statistics, to ensure a proper baseline for ψ' and Drell–Yan production in heavy-ion collisions. We conclude by summarizing the issue:

- The 450 GeV data points alone are not enough to determine the normal nuclear absorption at 158 GeV since the energy rescaling factors are too uncertain.
- The existing 200 GeV data points are also not enough because of their poor precision.
- The 450 and 200 GeV data sets, used together, would solve the problem if the absorption cross-section is the same for the two sets, an assumption presently without solid experimental evidence.

Thus proton data at 158 GeV must be collected in order to establish a robust reference baseline with respect to which the In+In and Pb+Pb J/ψ suppression patterns can be directly compared to place the existence of "anomalous" effects in the heavy-ion data on more solid ground. The present systematic

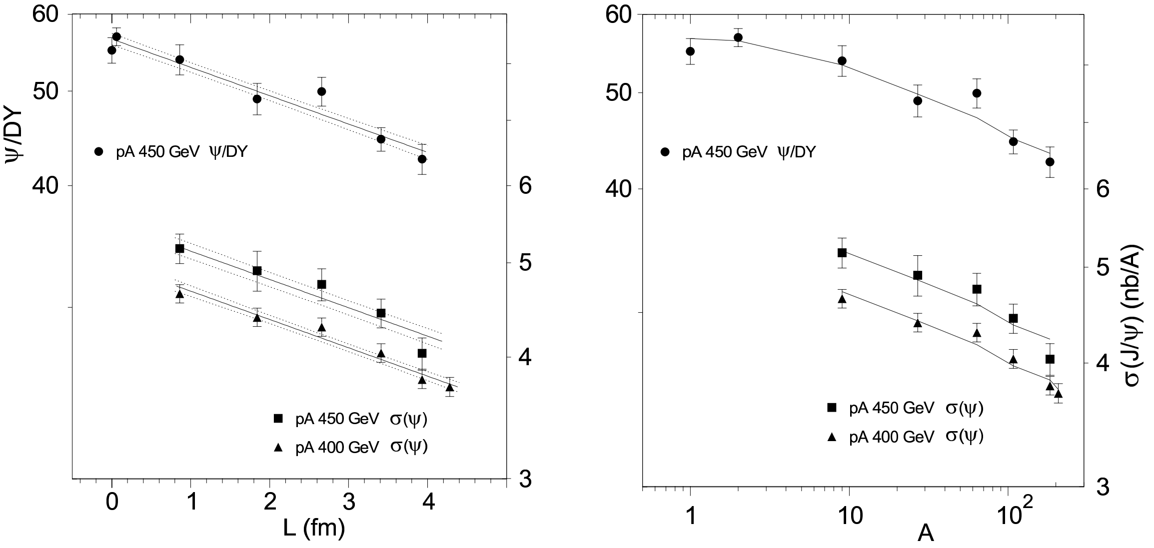

Fig. 7.25: The J/ψ production cross-sections in pA collisions at 400 and 450 GeV times the branching ratio to dimuons, in the phase space window of the measurements (right axis), or with respect to the yield of Drell–Yan dimuons in the mass range $2.9 < M < 4.5$ GeV (left axis). The data are plotted as a function of L (left-hand side) and of the mass number of the nuclei (right-hand side). The lines represent a fit in the framework of the Glauber nuclear absorption model, and result in a common absorption cross-section $\sigma_{\text{abs}} = 4.3 \pm 0.3$ mb. The uncertainties on the result of the fit are represented by the dotted lines on the left-hand side.

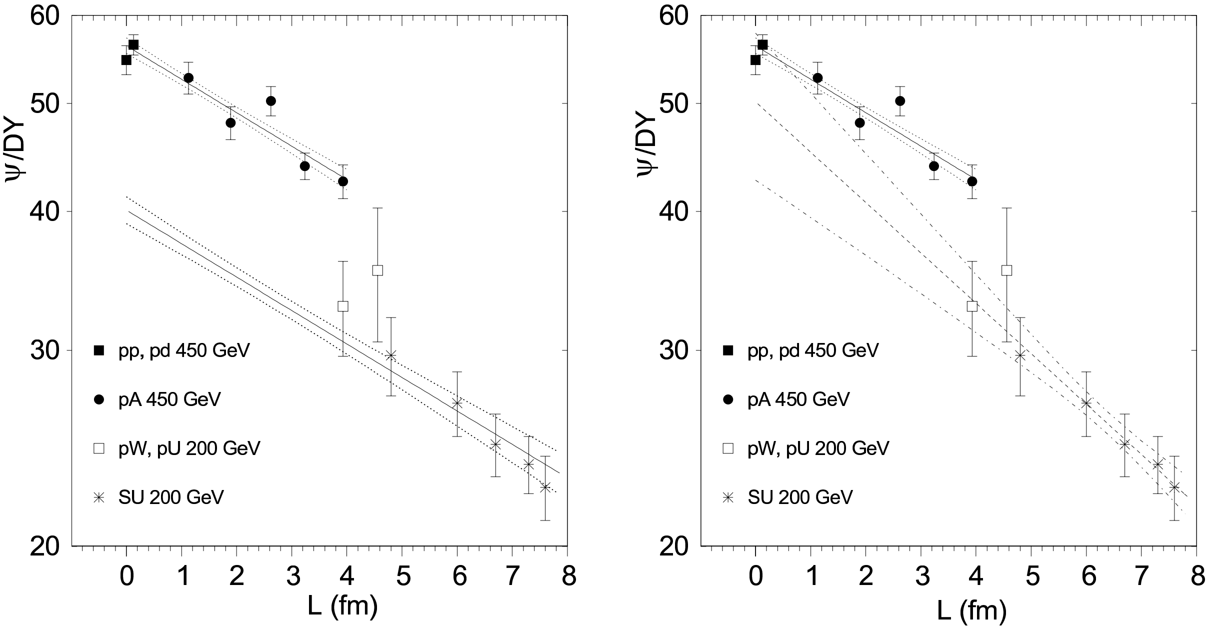

Fig. 7.26: Ratio of the J/ψ and Drell–Yan yields measured in pA and S+U collisions, as a function of L.

errors due to the energy (and phase space) corrections and to the absence of solid evidence that the absorption cross-section remains the same from 450 to 158 GeV, are the main sources of uncertainty in the interpretation of the data collected in nuclear collisions.

8.4 Charmonium production at RHIC

We review here the first results on charmonia produced in nuclear collisions at the Relativistic Heavy Ion Collider (RHIC). PHENIX is specifically designed to make use of high luminosity ion–ion, proton–ion, and proton–proton collisions at the RHIC to sample rare physics probes including the J/ψ and other heavy quarkonium states. The PHENIX experiment reported on J/ψ production in p–p, d–Au and Au–Au reactions at $\sqrt{s_{NN}} = 200$ GeV [128–130].

The PHENIX experiment is able to measure J/ψ's through their dilepton decay in four spectrometers: two central arms covering the mid-rapidity region of $|\eta| < 0.35$ and twice $\pi/2$ in azimuth and two forward muon arms covering the full azimuth and $1.2 < |\eta| < 2.4$ in pseudorapidity. The central spectrometers are comprised, from the inner radius outward, of a Multiplicity and Vertex Detector (MVD), Drift Chambers (DC), Pixel Pad Chambers (PC), Ring Imaging Cerenkov Counters (RICH), a Time-of-Flight Scintillator Wall (TOF), Time Expansion Chambers (TEC), and two types of Electromagnetic Calorimeters (EMC). This combination of detectors allows for the clean electron identification over a broad range of transverse momentum. Each forward spectrometer consists of a precision muon tracker (MuTr) comprised of three stations of cathode-strip readout chambers followed by a muon identifier (MuID) comprised of multiple layers of steel absorbers instrumented with low resolution planar drift tubes. Muons at the vertex must have a mean energy of at least 1.9 GeV to reach the MuID system. Further details of the detector design and performance are given in Ref. [131].

The data were recorded during the 2001/2002 and 2003 runs at $\sqrt{s} = 200$ GeV with 150 nb^{-1} and 350 nb^{-1} p–p collisions. Event samples were selected using online triggers and offline reconstruction criteria as described in Ref. [128]. Unlike-sign pairs and, for background estimation, like-sign pairs were combined to form invariant mass spectra. In Fig. 7.27, unlike-sign and like-sign invariant mass spectra from the entire Run2 pp data set are shown together. For electrons, the net yield in the mass region 2.8–3.4 GeV is 46, for muons in the range 2.71–3.67 GeV is 65.

The J/ψ cross-sections were determined from the measured yields using

$$B_{ll} \frac{d^2\sigma_{J/\psi}}{dy dp_T} = \frac{N_{J/\psi}}{(\int \mathcal{L}dt)\, \Delta y\, \Delta p_T} \frac{1}{A\,\epsilon} \tag{7.51}$$

where $N_{J/\psi}$ is the measured J/ψ yield, $\int \mathcal{L}dt$ is the integrated luminosity, B_{ll} is the branching fraction for the J/ψ to either e^+e^- or $\mu^+\mu^-$ pairs (PDG average value 5.9% [132]), and $A\,\epsilon$ is the acceptance times efficiency for detecting a J/ψ. The J/ψ rapidity distribution obtained by combining the dielectron and dimuon measurements is shown in Fig. 7.28 with the muon arm data divided into two rapidity bins. A fit to a shape generated with PYTHIA using the GRV94HO parton distribution functions is performed and gives a total cross-section, multiplied by the dilepton branching ratio, equal to:

$$\mathrm{BR} \times \sigma_{pp}^{J/\psi} = 159 \text{ nb} \pm 8.5\% \,(\text{fit}) \pm 12.3\% \,(\text{abs}) \tag{7.52}$$

where the first uncertainty comes from the fit and thus includes both the statistical and point-to-point systematics. The second uncertainty accounts for normalization systematic errors.

Preliminary analysis is now available of the data recorded during the 2003 run at $\sqrt{s} = 200$ GeV with 2.74 nb^{-1} d–Au collisions. In d–Au collisions, PHENIX is able to measure J/ψ production at forward, backward and central rapidity probing moderate to low x regions of the Au nucleus. The covered rapidity region spans the expected shadowing, antishadowing and no shadowing regions. The ratio between the J/ψ yields observed in d–Au and p–p collisions divided by 2 × 197 is shown in Fig. 7.29. Solid error bars represent statistical and point to point systematic uncertainties. The dashed

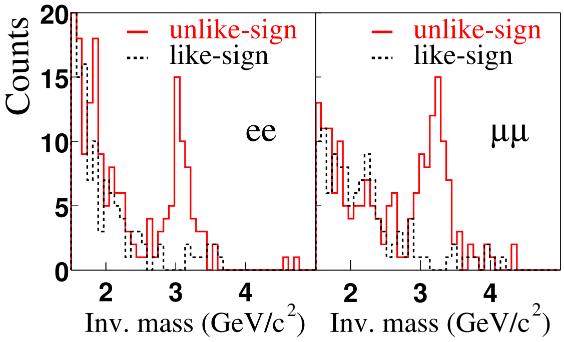

Fig. 7.27: The invariant mass spectra for dielectron and dimuon pairs in the Run 2 data sample. Unlike-sign pairs are shown as solid lines, like-sign pairs as dashed lines.

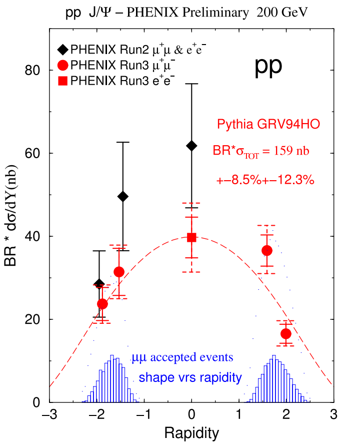

Fig. 7.28: J/ψ differential cross-section, multiplied by the dilepton branching ratio, versus rapidity as measured by the central and muon spectrometers.

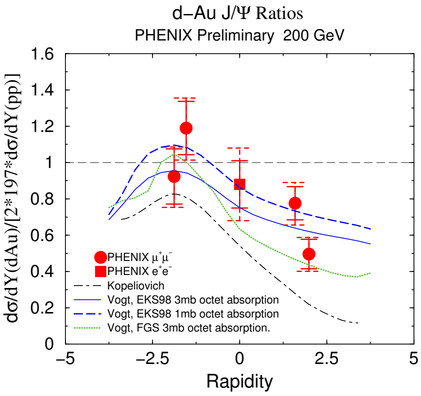

Fig. 7.29: Ratio between d–Au and p–p J/ψ differential cross-sections, divided by 2 × 197, versus rapidity.

error bars stand for the systematic uncertainties common to one spectrometer. An additional 13.4% global error bar is not displayed.

While this ratio is close to unity at backward rapidity, it is significantly lower at forward rapidity, where parton distributions are expected to be shadowed in a heavy nucleus. Theoretical predictions [133, 134] are displayed on the figure for comparison. The shape is consistent with shadowing at low x and less shadowing at larger x. Unfortunately, the statistical and systematic error bars make it difficult to distinguish among various shadowing models and models with various amounts of nuclear absorption.

The Au–Au data at $\sqrt{s_{NN}} = 200$ GeV used in this analysis were recorded during Run 2 at RHIC in the fall of 2001. For three exclusive centrality bins, 0–20%, 20–40%, and 40–90% of the total Au–Au cross-section, we determined the branching fraction of $J/\psi \to e^+e^-$ (B=5.93 ± 0.10 × 10^{-2} [132]) times the invariant yield at mid-rapidity $dN/dy|_{y=0}$.

In Fig. 7.30 we show the results from the three Au–Au centrality bins and the proton–proton data normalized per binary nucleon–nucleon collision as a function of the number of participating nucleons. Note that for proton–proton reactions, there are two participating nucleons and one binary collision. Despite the limited statistical significance of these first J/ψ results, we can address some important physics questions raised by the numerous theoretical frameworks in which J/ψ rates are calculated. The binary scaling expectations are also shown as a gray band. We also show a calculation of the suppression expected from "normal" nuclear absorption using a $\sigma_{\rm abs} = 4.4$ mb [123] and 7.1 mb [94]. We show the NA50 suppression pattern relative to binary scaling [119, 120], normalized to match our proton–proton data point at 200 GeV. The data disfavor binary scaling while they are consistent with "normal" nuclear absorption alone and also the NA50 suppression pattern measured at lower energies, within the large statistical errors.

One model calculation [104, 105] including just the "normal" nuclear and plasma absorption components at RHIC energies is shown in Fig. 7.31. The higher temperature (T) and longer time duration of the system at RHIC lead to a predicted larger suppression of J/ψ relative to binary collision scaling.

Many recent theoretical calculations also include the possibility for additional late stage re-creation or coalescence of J/ψ states. In Ref. [104,105], both break-up and creation reactions $D+\overline{D} \leftrightarrow J/\psi+X$ are included. At the lower fixed target CERN energies, this represents a very small contribution due to the small charm production cross-section. However, at RHIC energies, where in central Au–Au collisions around 10 $c\overline{c}$ pairs are produced, the contribution is significant.

The sum of the initial production, absorption, and re-creation is shown in Fig. 7.31.

A different calculation [135] assumes the formation of a quark–gluon plasma in which the mobility of heavy quarks in the deconfined region leads to increased $c\overline{c}$ coalescence. This leads to a very large enhancement of J/ψ production at RHIC energies for the most central reactions. The model considers the plasma temperature (T) and the rapidity width (Δy) of charm quark production as input parameters. Shown in Fig. 7.31 are the calculation results for T = 400 MeV and Δy = 1, 2, 3, and 4. The narrower the rapidity window in which all charm quarks reside, the larger the probability for J/ψ formation. All of these parameters within this model predict a J/ψ enhancement relative to binary collisions scaling, disfavored by our data.

Another framework for determining quarkonia yields is to assume a statistical distribution of charm quarks that may then form quarkonia. A calculation assuming thermal, but not chemical equilibration [99], is shown in Fig. 7.31.

Significantly larger data sets are required to address the various models that are still consistent with our first measurement. Key tests will be the p_T and x_F dependence of the J/ψ yield, and how these compare with other quarkonium states such as the ψ'.

9 QUARKONIUM PRODUCTION IN NUCLEAR COLLISIONS[10]

Quarkonium may be produced via photoproduction at hadron colliders. The electromagnetic field of a proton or ion projectile acts as a field of virtual photons. These photons may collide with an oncoming target nucleus to produce quarkonium. The photon flux is high enough to allow detailed studies of charmonium photoproduction. The cross-section is sensitive to the gluon content of the target. Photoproduction at the LHC reaches an order of magnitude higher energies than are possible at HERA. For ions, the advance beyond existing data is even larger which may allow the first real low-x measurements of gluon shadowing.

Photoproduction has traditionally been studied with fixed target photon beams and at electron–proton colliders. However, energetic hadrons also have significant electromagnetic fields and high energy pp, $\overline{p}p$ and AA colliders can be used to study photoproduction at photon energies higher than those currently accessible. These photoproduction reactions are of interest as a way to measure the gluon distribution in protons at low Feynman x. The Fermilab Tevatron, RHIC and the LHC (with both proton and ion beams) all produce significant quantities of heavy quarkonium. Indeed, J/ψ photoproduction may have already been seen by the CDF collaboration.

One unique aspect of photoproduction at hadron colliders is that the initial system is symmetric so that photoproduction can occur from either ion. Since these two possibilities are indistinguishable,

---

[10] Author: S. R. Klein

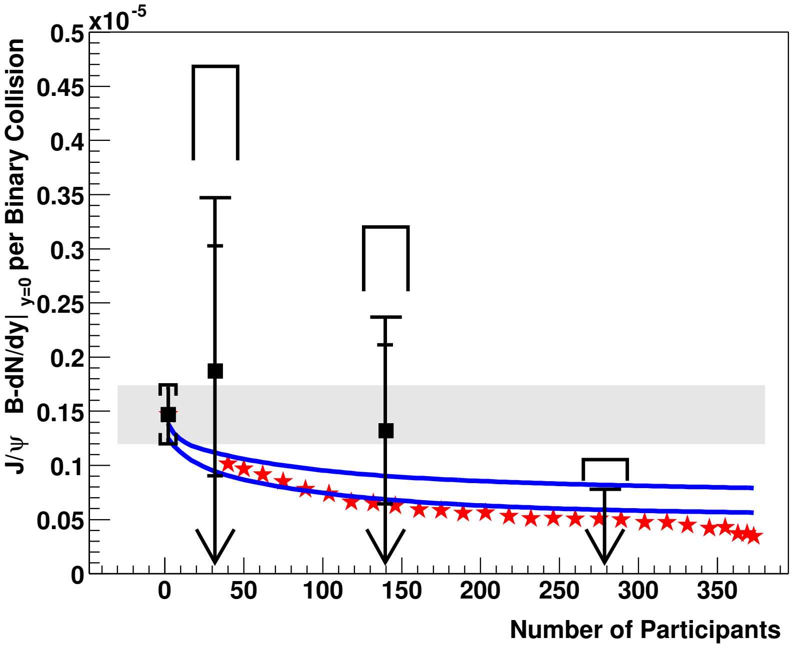

Fig. 7.30: The J/ψ yield per binary collision is shown from proton–proton reactions and three exclusive centrality ranges of Au–Au reactions all at $\sqrt{s_{NN}}$ = 200 GeV. The solid line is the theoretical expectation from "normal" nuclear absorption with $\sigma_{c\bar{c}-N}$ = 4.4 mb (upper curve) and 7.1 mb (lower curve) cross-section. The stars are the J/ψ per binary collision measured by the NA50 experiment at lower collision energy. In order to compare the shapes of the distribution, we have normalized the NA50 data to match the central value for our proton–proton results.

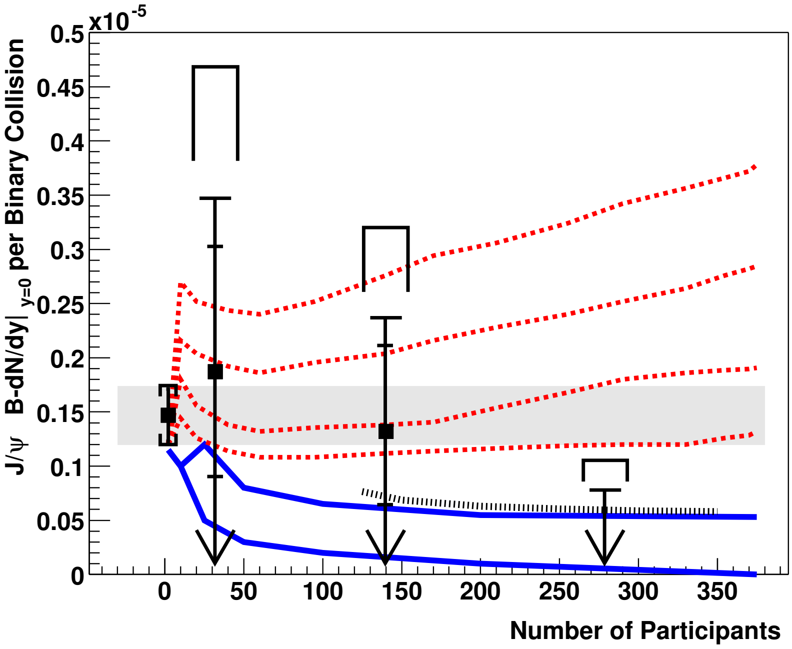

Fig. 7.31: The J/ψ yield per binary collision is shown from proton–proton reactions and three exclusive centrality ranges of Au–Au reactions all at $\sqrt{s_{NN}}$ = 200 GeV. The lowest curve is a calculation including "normal" nuclear absorption in addition to substantial absorption in a high temperature quark–gluon plasma [104, 105]. The curve above this is including backward reactions that recreate J/ψ. The statistical model [99] result is shown as a dotted curve for mid-central to central collisions just above that. The four highest dashed curves are from the plasma coalescence model [135] for a temperature parameter of T = 400 MeV and different charm rapidity widths.

the amplitudes must be added. This interference significantly affects the p_T spectrum of the produced quarkonium. The relative sign of the two amplitudes depends on the symmetry of the system. The symmetry is different for $p\overline{p}$ than pp and AA colliders, leading to significantly different p_T spectra for particle–particle and particle–antiparticle colliders.

9.1 Cross-section calculation

The cross-section for vector meson production is the convolution of the photon flux dn/dk for photon energy k with the photon–proton or photon–nucleus cross-sections $\sigma_{\gamma A}$ [136, 137]:

$$\sigma(A+A \to A+A+V) = 2\int_0^\infty \frac{dn}{dk}\,\sigma_{\gamma A}(k)\,dk\ . \tag{7.53}$$

Here, A refers to any ion, including protons. The ’2’ is because either nucleus can emit the photon or be the target. Interference between the two possibilities alters the p_T distribution but does not significantly affect the total cross-section.

The rapidity, y, of a produced state with mass M_V is related to the photon energy through $y = \ln(2k/M_V)$. Using this relation in Eq. (7.53) and differentiating gives

$$\frac{d\sigma}{dy} = k\frac{dn}{dk}\sigma_{\gamma A\to VA}(k)\ . \tag{7.54}$$

At mid-rapidity, $y = 0$, the photon energies for the two possibilies (as to which nucleus emitted the photon) are equal. However, away from mid-rapidity, the photon energies are different,

$$k_{1,2} = \frac{M_V}{2}\exp(\pm y) \tag{7.55}$$

so that the amplitudes for the two possibilities are also different.

We now consider the ingredients in the cross-section in turn. The photon flux from a relativistic hadron is given by the Weizsäcker–Williams formalism. One important detail is the form factor of the emitter.

For protons, the form factor was considered by Drees and Zeppenfield. They use a dipole form factor $F(Q^2) = 1/(1+Q^2/(0.71\,\mathrm{GeV}^2))^2$ for the proton, and found [138]:

$$\frac{dn}{dk} = \frac{\alpha}{2\pi k}\left[1+(1-z)^2\right]\left(\ln I - \frac{11}{6} + \frac{3}{I} - \frac{3}{2I^2} + \frac{1}{3I^3}\right) \tag{7.56}$$

where $z = W_{\gamma p}^2/s$, $A = 1 + (0.71\,\mathrm{GeV}^2)/Q^2_{\mathrm{min}}$ and $Q^2_{\mathrm{min}} \approx (k/\gamma)^2$. Here, $W_{\gamma p}$ is the γp centre of mass energy, and $\sqrt{s}$ is the proton–proton centre of mass energy. This photon spectrum is similar to that of a point charge with a minimum impact parameter of $b_{\mathrm{min}} = 0.7$ fm.

Drees and Zeppenfeld neglected the magnetic form factor of the proton which is important only at very high energies [139]. They also required that the proton remain intact. If the proton is allowed to be excited, the effective flux increases considerably [140]. However, in this case, one or both protons dissociate, producing hadronic debris. We will ignore this possibility here since the debris considerably complicates event selection.

For ion–ion collisions, the cutoff conditions are somewhat different. For a vector meson to be observable, the two nuclei must miss each other, with $b_{\mathrm{min}} = 2R_A$, where R_A is the nuclear radius. The effective photon flux from a charge Z nucleus is the flux striking an incoming nucleus subject to that constraint. This is within 15% of the flux integrated over the requirement $r > 2R_A$, given analytically by [141]

$$\frac{dn}{dk} = \frac{2Z^2\alpha}{\pi k}\left(XK_0(X)K_1(X) - \frac{X^2}{2}\left[K_1^2(X) - K_0^2(X)\right]\right) \tag{7.57}$$

where $X = kr/\gamma\hbar$. More detailed calculations find the photon flux numerically by determing the photon flux from one nucleus that interacts in another, subject to the criteria that the two nuclei do not interact hadronically.

As a check of the photon flux rates, we consider an alternate calculation that replaces the proton form factor with a hard cutoff, $b_{\rm min} = 1.0$ fm. This stricter requirement slightly decreases the effective photon flux.

The leading-order vector meson photoproduction cross-section for a vector meson with mass M_V is [142]

$$\left.\frac{d\sigma(\gamma p\rightarrow Vp)}{dt}\right|_{t=0} = \frac{\alpha_s^2\Gamma_{ee}}{3\alpha M_V^5}16\pi^3\left[xg(x,M_V^2/4)\right]^2 . \qquad (7.58)$$

More recent and more sophisticated calculations have considered the use of relativistic wave functions, off-diagonal parton distributions, and NLO contributions [143, 144]. Parton–hadron duality has also been used to study quarkonium production. Calculations give cross-sections ~30–50% larger than the pQCD results, depending on $W_{\gamma p}$ [144]. The QCD calculations are in reasonable agreement with data on J/ψ [145] and Υ [146] [147] production at HERA. The Υ data has limited statistics, and, consequently, significant uncertainties.

To assess the viability of photoproduction at hadron colliders, we use simple cross-section parameterizations to estimate the rates:

$$\sigma_{\gamma p}(W_{\gamma p}) = 1.5W_{\gamma p}^{0.8}\,{\rm pb} \qquad (7.59)$$

for J/ψ, and

$$\sigma_{\gamma p}(W_{\gamma p}) = 0.06W_{\gamma p}^{1.7}\,{\rm pb} \qquad (7.60)$$

for $\Upsilon(1S)$ where $W_{\gamma p}$ is in GeV. Both H1 and ZEUS estimate that roughly 70% of the signal is from the $\Upsilon(1S)$ state. The cross-section for the ψ' is expected to be about 15% of that for the J/ψ.

One drawback for this parameterization is that there is a significant discontinuity at threshold, $W_{\gamma p} = m_p + m_{J/\Psi}$. In this region, either better data or a more sophisticated calculation is needed.

For heavy mesons, the cross-section $\gamma A \rightarrow VA$ is not well measured. There is little data for the J/ψ and none on the Υ. The ion-target cross-sections depends on the square of the gluon density. Thus vector meson photoproduction can provide a sensitive measurement of gluon shadowing. At LHC, mid-rapidity production of the J/ψ and Υ corresponds to $x \approx 5\times10^{-4}$ and 1.7×10^{-3} respectively. In this region, shadowing will likely reduce the cross-sections by 30–50% for Pb+Pb collisions at the LHC.

Neglecting shadowing, the cross-section for vector meson photoproduction in a nucleus, $\gamma A \rightarrow VA$, may be determined using data on photoproduction off a proton target as input to a Glauber calculaton. However, because the cross-section for a $c\overline{c}$ or $b\overline{b}$ pair to interact in a nucleus is relatively small, multiple interactions are unlikely and the calculation simplifies so that the forward scattering cross-section scales with A^2 [137, 148]

$$\frac{d\sigma(\gamma A\rightarrow \Upsilon A)}{dt} = A^2\left.\frac{d\sigma(\gamma p\rightarrow \Upsilon p)}{dt}\right|_{t=0}|F(t)|^2 . \qquad (7.61)$$

A Woods–Saxon distribution can be used for the nuclear form factor $F(t)$. The total photonuclear cross-section is the integral of Eq. (7.61) over all momentum transfers, $t > t_{\rm min} = [M_\Upsilon^2/4k\gamma]^2$. For protons, $d\sigma/dt|_{t=0}$ is determined from HERA data. For the Υ, an exponential t-dependence is assumed with the same slope, 4 GeV^{-2}, as for J/ψ production, leading to a forward scattering amplitude about 5% lower than if the proton form factor had been used. With these ingredients, the ion–ion photoproduction cross-section may be calculated from Eq. (7.53).

This A^2 scaling applies for coherent production with $p_T < \hbar/R_A$. At significantly larger p_T, the scattering is incoherent and the cross-section should scale as A. The coherence leads to a large peak in the production at small p_T, providing a clean experimental signature which greatly simplifies the data analysis.

Table 7.3: Cross-sections and rates for production of the J/ψ and the Υ. The rates are for 10^7 s of running at the Tevatron, pp at the LHC and AA at RHIC, and 10^6 s of running with AA at the LHC and pp at RHIC.

Collider	Species	$\sqrt{s_{NN}}$	Luminosity	J/ψ		Υ	
		(GeV)	($\mathrm{cm}^{-2}\mathrm{s}^{-1}$)	σ (μb)	Rate	σ (nb)	Rate
RHIC	pp	500	10^{31}	0.007	7.0×10^4	0.012	120
RHIC	Au+Au	200	2×10^{26}	290	5.8×10^5	–	–
Tevatron	$p\overline{p}$	1960	2×10^{32}	0.023	4.6×10^7	0.12	2.4×10^5
LHC	pp	14000	10^{34}	0.120	1.2×10^{10}	3.5	3.5×10^8
LHC	Pb+Pb	5500	10^{27}	32000	3.2×10^6	170000	1.7×10^5

For lighter mesons, the interaction cross-section is larger and the Glauber calculation is required to determine the A scaling. The STAR collaboration has studied ρ photoproduction in Au+Au collisions [149] and has found that the cross-sections agree with a calculation based on Eq. (7.53) and a Glauber calculation.

Exclusive J/ψ photoproduction in pp interactions was also considered by Khoze *et al.* [150]. They use a very different approach, based on the proton energy lost.

9.2 Experimental prospects

We consider pp and AA collisions at RHIC, $p\overline{p}$ at the Tevatron, and pp and Pb+Pb the LHC. The cross-sections and rates, as well as the assumed energies and luminosities, are shown in Table 7.3. Since the LHC is primarily a pp collider, assume 10^7 s of pp and 10^6s of AA running per year. Because RHIC is primarily an ion collider, we reverse the two durations. We assume 10^7 s of Tevatron operation per year. Although it is interesting, we do not consider dA collisions at RHIC or pA or dA collisions at the LHC.

Figure 7.32 shows the rapidity distribution for vector meson production in pp and $\overline{p}p$ collisions. The solid histogram is with the dipole form factor discussed above. For the Υ, the shaded bands show the uncertainty in the production rates, based on the uncertainties in the HERA cross-sections but neglecting extrapolation uncertainties. The dashed line is an alternative calculation, with $b_{\mathrm{min}} = 1.0$ fm replacing the form factor. For the J/ψ, the abrupt dropoff at large $|y|$ is due to the discontinuity at threshold.

Figure 7.33 shows the rapidity distribution for Υ production in Si+Si collisions at RHIC (the Υ is below the effective threshold in Au+Au), and Pb+Pb collisions at the LHC. The solid histogram is for the dipole form factor, and the shaded bands show the uncertainty due to the uncertainties in the HERA cross-sections, but neglecting uncertainties due to the extrapolation.

Coherent Υ production at the LHC was also studied by Frankfurt *et al.* [151]. The result (solid curve in Fig. 7.33) is about 10% higher than their result for the impulse approximation (no shadowing). The difference may be due to the slightly different photon spectrum and slope of $d\sigma/dt$ in photon–proton interactions.

At the LHC, the cross-sections are very large for both pp and AA collisions, and obtaining good event samples should be relatively straightforward. For the Υ in pp collisions, production tends to be at large $|y|$. The rapid rise in cross-section, $\sigma \propto W^{1.7}$ outweighs the $dn/dk \propto 1/k$ photon spectrum. For the J/ψ, the $W_{\gamma p}$ dependence is smaller and nearly 'cancels' the photon spectrum, leading to a rather flat $d\sigma/dy$. In both cases, it should be easy to obtain good statistics, even with only a central detector.

At the Tevatron, the cross-sections are smaller. However, the CDF collaboration has already observed an apparent exclusive J/ψ signal which appears consistent with photoproduction [152]. With an appropriate trigger and more data, the Υ should be within reach.

Very roughly, the photoproduction cross-section is about 1/1000 of the equivalent hadroproduction cross-sections [153] with moderate variation depending on species and beam energy. Despite the small

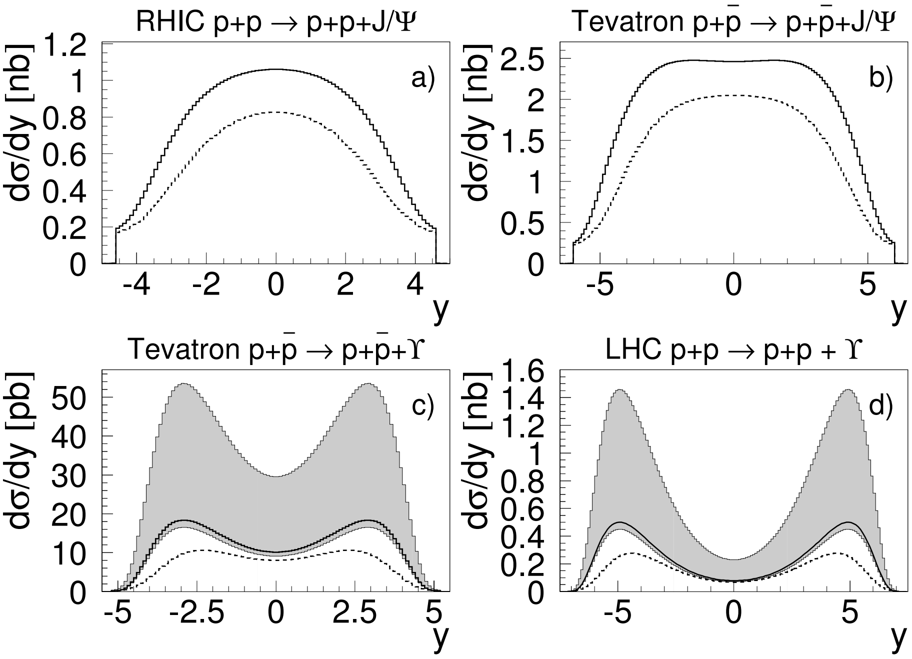

Fig. 7.32: Rapidity distributions for photoproduction of J/ψ and $\Upsilon(1S)$ mesons in pp and $p\overline{p}$ interactions at RHIC, the Tevatron, and the LHC [136]. The curves are explained in the text.

fraction, because of the very different event characteristics, clean separation of photoproduction seems possible.

Hadronically produced vector mesons have $p_T \sim M_V$. In contrast, almost all photoproduced mesons have $p_T < 1$ GeV (cf. Fig. 7.34). Such a cut eliminates about 94% of the hadroproduced Υ at the Tevatron [154] while retaining almost all of the photoproduction.

As long as both protons remain intact, the vector meson will not be accompanied by any other particles in the same event. In contrast, in hadronic events, additional particles are distributed over the available phase space. A moderate requirement for two rapidity gaps around the vector meson should remove most of the remaining hadronic background [153], even at RHIC energies. The Fermilab results on exclusive J/ψ production appear to bear this out.

For heavy-ion collisions, the situation is even simpler since most of the coherent vector meson production is at $p_T < 100$ MeV/c. In addition, the ions can be required to remain intact and/or rapidity gaps can be required. These techniques were effective in isolating the ρ^0 in STAR [149]. In 2004, the RHIC experiments collected a large data sample of Au+Au collisions at $\sqrt{s_{NN}} = 200$ GeV. Thus large experiments should be able to observe J/ψ photoproduction and measure gluon shadowing in the region $x \approx 0.015$.

9.3 Interference and the p_T spectrum

Photoproduction in pp and $p\overline{p}$ collisions differs from production in ep or eA collisions in that either projectile can act as photon source or target. For small meson p_T, the two possibilities are indistinguishable so that the amplitudes add [155]. The vector meson production is well localized to in or near (within 1 fm of) the two sources, giving a cross-section of

$$\sigma = \left|A_1(y) \mp A_2(y) \exp i(\vec{p}_T \cdot \vec{b})\right|^2 \tag{7.62}$$

where $A_1(y)$ and $A_2(y)$ are the amplitudes for photoproduction at the two sources and the propagator, $\exp i(\vec{p}_T \cdot \vec{b})$, accounts for the ion–ion separation. The relative sign of the two amplitudes depends

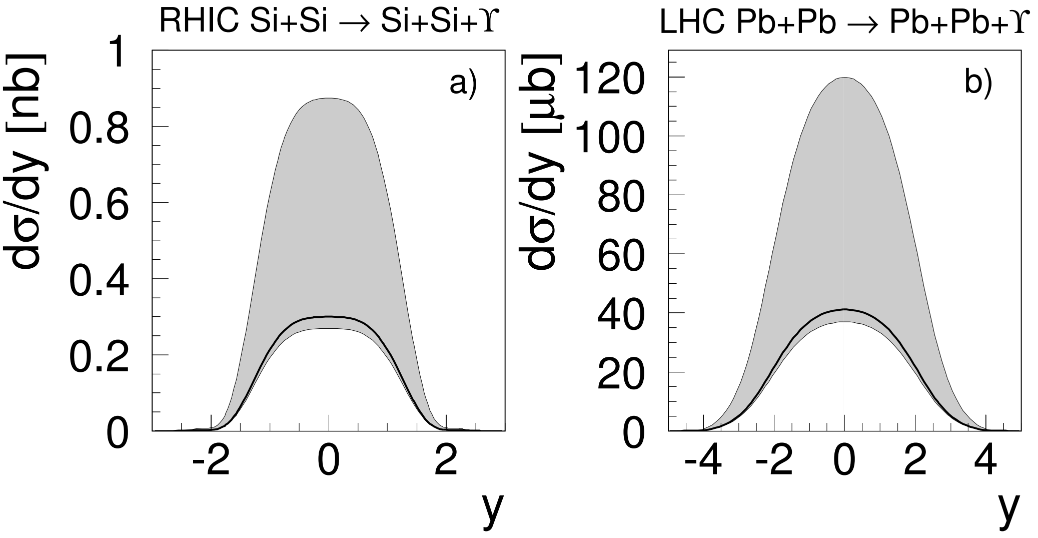

Fig. 7.33: Rapidity distributions of Υ mesons produced in coherent photonuclear interactions at RHIC and the LHC [136]. The solid curves correspond to the parameterization $\sigma_{\gamma p}(W_{\gamma p}) = 0.06 W_{\gamma p}^{1.7}$ (pb) and the grey bands show the uncertainty in $\sigma_{\gamma p}$

on the symmetry of the system. For pp and AA collisions, transforming from nucleus 1 emitting a photon which interacts with nucleus 2, to nucleus 2 emitting a photon which interacts with nucleus 1 is a parity transformation. Vector mesons are negative parity, so the sign is negative. For $p\overline{p}$ collisions, the transformation is CP, positive for vector mesons, giving a positive sign.

At mid-rapidity, $A_1 = A_2$ and

$$\sigma = \sigma_0 \left(1 \mp \cos\left(\vec{p}_T \cdot \vec{b}\right) \right) \tag{7.63}$$

where σ_0 is the cross-section without interference. The interference depends on the unknown impact parameter which must be integrated over.

Without interference, the p_T spectrum is that for production off a single (anti)proton. This spectrum is the convolution of the photon transverse momentum spectrum with the spectrum of transverse momentum transfers from the target [155]. For $p_T > \hbar/\langle b \rangle$, $\cos(\vec{p}_T \cdot \vec{b})$ oscillates rapidly as b varies, giving a zero net contribution to the integral. For small transverse momenta, however, $\vec{p} \cdot \vec{b} < \hbar$ for all relevant impact parameters and interference alters the spectrum. This alteration has been observed in ρ^0 production at RHIC [156].

Figure 7.34 compares $d^2\sigma/dydt$ with and without interference at RHIC and the Tevatron. Figure 7.34 includes a $b_{min} = 1.0$ fm cut which has a small effect on the spectrum. The interference is large for $t < 0.05$ GeV^2/c^2. The different sign of the interference in pp and $p\overline{p}$ is clearly visible.

Photoproduction of other final states should also be accessible at existing and future $p\overline{p}$ and pp colliders. Open charm, bottom and even top quark production should be accessible [157] in ion–ion and deuterium–ion collisions and could be used to measure the charge of the top quark as well as determine the nuclear gluon distributions. These events would have only a single rapidity gap but the experimental techniques should be similar. Because of the large rates, at least for ion–ion collisions, the signal to noise ratios should be high.

To summarize, we have calculated the heavy vector meson photoproduction cross-sections in pp and $p\overline{p}$ collisions. The cross-sections are large enough for this reaction channel to be observed experimentally. The $d\sigma/dt$ distribution is distinctly different in pp and $p\overline{p}$ collisions because of the interference between the production sources. The cross-section for producing Υ mesons in coherent photonuclear

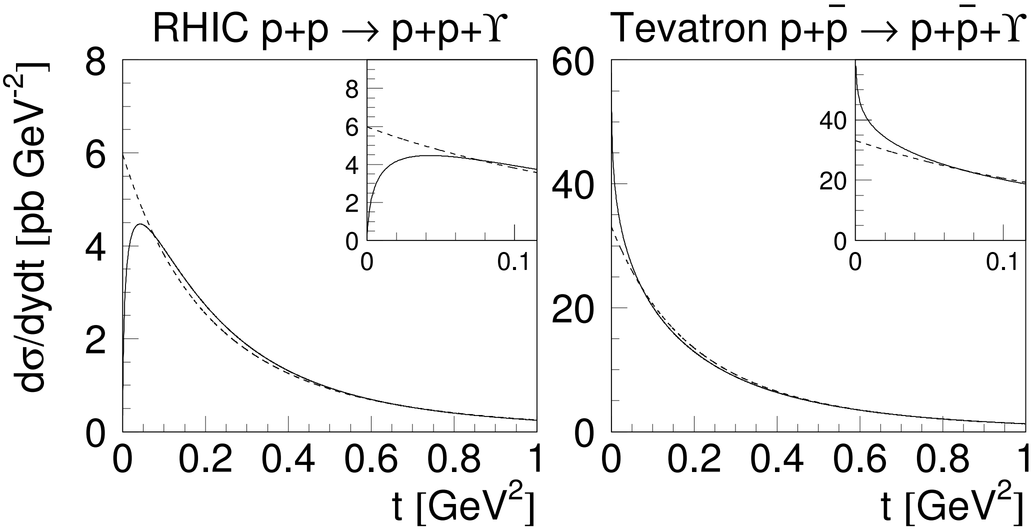

Fig. 7.34: The $\Upsilon(1S)$ photoproduction cross-section, $d\sigma/dydt$, at mid-rapidity in pp and $p\overline{p}$ collisions at RHIC and the Tevatron [136]. The inset has an expanded t scale.

Pb+Pb interactions at the LHC is large. Because of the distinctive experimental signature, these reactions should be easy to detect.

10 OUTLOOK[11]

Recent advances in lattice and analytical calculations described in this Chapter have significantly improved the theoretical understanding of heavy quarkonium dynamics in hot QCD matter. In fact, since many of the recent results came as a surprise, they still need to be analyzed, improved upon, and clarified.

The list of open issues which can be addressed by theory and experiment in the near future includes:

- Lattice QCD at finite temperature:
  What is the critical temperature at which different quarkonium states dissociate? What is the influence of temperature on the masses, dispersion relations, and widths of quarkonia? How big is the influence of light quarks? What are the properties of strongly interacting matter in the vicinity of the deconfining transition and how do they compare with phenomenological models?
- Lattice QCD at zero temperature:
  What are the matrix elements of different gluon and quark operators of various dimension which are related to quarkonium dissociation?
- Analytic theoretical calculations at zero temperature:
  Analyze the expressions for quarkonium dissociation amplitudes, and relate them to the matrix elements which can be computed on the lattice. Apply and test theoretical approaches developed for the studies of quarkonium dissociation to exclusive quarkonium decays and quarkonium production; understand the range of validity of various approaches.
- Analytic theoretical calculations at finite temperature:
  Understand the properties of Quark–Gluon Plasma in the vicinity of the deconfinement phase transition; identify the dynamical degrees of freedom and apply this knowledge to understanding the lattice results at finite T. Try to develop a quantitative theory of quarkonium interactions with hot QCD matter.

---

[11] Authors: D. Kharzeev, M. P. Lombardo, C. Lourenço, M. Rosati, H. Satz

- Experiment:
  Collect data on the nuclear dependence of the production of different quarkonium states, including the χ family, in pA collisions in a broad range of x_F (rapidity), and different energies. Refine the data on quarkonium suppression in nucleus–nucleus collisions at SPS energy; improve statistics on quarkonium suppression in Au+Au (and some other, lighter, AA system) collisions at RHIC; prepare for the LHC. Measure photoproduction cross-sections to determine the nuclear gluon density.

To summarize, impressive progress in the physics of quarkonium interactions with QCD media has been made in recent years. It has already become clear that the physics of heavy quark bound states in QCD media is a rich and promising field of theoretical and experimental studies. Nevertheless, even a brief examination of the list above shows that a lot more has to be done before one can claim an understanding of quarkonium interactions in media.

REFERENCES

[1] T. Matsui and H. Satz, Phys. Lett. B **178** (1986) 416.

[2] D. Kharzeev and H. Satz, Phys. Lett. B **334** (1994) 155

[3] D. Kharzeev and H. Satz, arXiv:hep-ph/9505345.

[4] X. M. Xu, D. Kharzeev, H. Satz and X. N. Wang, Phys. Rev. C **53** (1996) 3051

[5] E. V. Shuryak, Phys. Lett. B **78** (1978) 150

[6] G. Bhanot and M. E. Peskin, Nucl. Phys. B **156** (1979) 391.

[7] D. Kharzeev, L. D. McLerran and H. Satz, Phys. Lett. B **356** (1995) 349

[8] C. Y. Wong, Phys. Rev. C **65** (2002) 034902

[9] D. Kharzeev, Nucl. Phys. A **610** (1996) 418c

[10] S. Digal, P. Petreczky and H. Satz, Phys. Rev. D **64**, 094015 (2001)

[11] G. Röpke, D. Blaschke and H. Schulz, Phys. Rev. D **38** (1988) 3589.

[12] F. Karsch, M. T. Mehr and H. Satz, Z. Phys. C **37** (1988) 617.

[13] T. Hashimoto, K. Hirose, T. Kanki and O. Miyamura, Z. Phys. C **38** (1988) 251.

[14] T. Umeda, K. Nomura and H. Matsufuru, arXiv:hep-lat/0211003.

[15] S. Datta, F. Karsch, P. Petreczky and I. Wetzorke, arXiv:hep-lat/0208012.

[16] S. Digal, S. Fortunato, P. Petreczky and H. Satz, Phys Lett. B **549**, 101 (2002); J. P. Blaizot, M. Dinh and J. Y. Ollitrault, Phys. Rev. Lett. **85**, 4012 (2000).

[17] M. Bedjidian *et al.*, in *Hard Probes in Heavy Ion Collisions at the LHC*, CERN-2004-009, p. 247.

[18] F. Karsch and E. Laermann, in Hwa, R.C. (ed.) *et al.*:*Quark gluon plasma* pag. 1, arXiv:hep-lat/0305025

[19] M. A. Stephanov, Prog. Theor. Phys. Suppl. **153** (2004) 139

[20] J. Kapusta, *Finite Temperature Field Theory*, Cambridge University Press, 1994.

[21] F. Karsch, Lect. Notes Phys. **583**, 209 (2002) [arXiv:hep-lat/0106019].

[22] For pedagogical presentation in QED see Landau and Lifshitz, *Quantum Electrodynamics*; for QCD see e.g., W. Lucha, F. F. Schoberl and D. Gromes, Phys. Rept. **200** (1991) 127.

[23] L. McLerran, B. Svetitsky, Phys. Rev D **24** (1981) 450

[24] J. Brown, E. Weisberger, Phys. Rev. D **20** (1979) 3239

[25] S. Nadkarni, Phys. Rev. D **34** (86) 3904

[26] O. Philipsen, Phys. Lett. B **535** (2002) 138

[27] O. Jahn, O. Philipsen, Phys. Rev. D **70** (2004) 074504

[28] O. Kaczmarek *et al.*, Phys.Lett. B **543** (2002) 41

[29] O. Kaczmarek *et al.*, Nucl.Phys. B (Proc. Suppl.) **129** (2004) 560

[30] O. Kaczmarek *et al.*, Phys. Rev. D **70** (2004) 074505

[31] S. Necco, R. Sommer, Phys. Lett. B **523** (2001) 135

[32] S. Necco, R. Sommer, Nucl. Phys. B **622** (2002) 328

[33] M. Peter, Nucl. Phys. B **501** (1997) 471

[34] Y. Schröder, Phys. Lett. B **447** (1999) 321

[35] M. Le Bellac, *Thermal Field Theory*, Cambridge, 1996

[36] T. Hatsuda and T. Kunihiro, Phys. Rev. Lett. **55**, 158 (1985); Phys. Rept. **247**, 221 (1994).

[37] E. Braaten,, R. D. Pisarski and T. C. Yuan, Phys. Rev. Lett. **64** (1990) 2242.

[38] F. Karsch, E. Laermann, P. Petreczky and S. Stickan, Phys. Rev. D **68**, 014504 (2003)

[39] S. Datta, F. Karsch, P. Petreczky and I. Wetzorke, Phys. Rev. D **69** (2004) 094507

[40] M. Asakawa and T. Hatsuda, Phys. Rev. Lett. **92** (2004) 012001

[41] T. Umeda et al, Eur. Phys. J. C **39S1** (2005) 9.

[42] M. Asakawa, T. Hatsuda and Y. Nakahara, Prog. Part. Nucl. Phys. **46** (2001) 459

[43] M. Jarrel and J.E. Gubernatis, Phys. Rep. **269**, 133 (1996).

[44] T. Yamazaki et al (CP-PACS), Phys. Rev. D **65**, 014501 (2002).

[45] R. K. Bryan, Eur. Biophys. J. **18**, 165 (1990)

[46] Talks by M. Asakawa, S. Datta and H. Matsufuru in the RIKEN BNL workshop on "Lattice QCD ar Finite Temperature and Density", Feb 8-12, 2004; see proceedings.

[47] T. Umeda $etal.$, Int. J. Mod. Phys. A **16**, 2215 (2001).

[48] M. Oevers, C. Davies and J. Shigemitsu, Nucl. Phys. Proc. Suppl. **94** (2001) 423

[49] B. Alessandro *et al.* (NA50 Coll.), Nucl. Phys. **A715**, 679c (2003).

[50] M.C. Abreu *et al.* (NA50 Collaboration), Phys. Lett. B 450 (1999) 456.

[51] J.W. Chen and M.J. Savage, Phys. Rev. D **57** (1998) 2837; E. Shuryak and D. Teaney, Phys. Lett. B **430** (1998) 37; K.L. Haglin and C. Gale, Phys. Rev. C **63** (2001) 065201; nucl-th/0002029; C.Y. Wong, E.S Swanson and T. Barnes, nucl-th/0002034; K.L. Haglin, nucl-th/0205049; C.Y. Wong, T. Barnes, E.S. Swanson and H.W. Crater, nucl-th/0112023; S.H. Lee and Y. Oh, J. Phys. G **28** (2002) 1903; R.S. Azevedo and M. Nielsen, nucl-th/0407080; Y. Oh, T. Song, S.H. Lee and C.Y. Wong, J. Korean Phys. Soc. **43** (2003) 1003; Y. Oh, T. Song, S.H. Lee, Phys. Rev. C **63** (2001) 034901.

[52] M. Peskin, Nucl. Phys. B **156** (1979) 365; G. Bhanot and M. Peskin, Nucl. Phys. B **156** (1979) 391; D. Kharzeev and H. Satz, Phys. Lett. B **334** (1994) 155.

[53] D. Kharzeev, H. Satz and G. Zinovjev, Phys. Lett. B **389** (1996) 595; S.H. Lee and Y. Oh, J. Phys. G **28** (2002) 1903; F. Arleo, P.B. Gossiaux, T. Gousset and J. Aichelin, Phys. Rev. D **65** (2002) 014005; Y. Oh, S. Kim and S.H. Lee, Phys. Rev. C **65** (2002) 067901.

[54] K. Martins, D. Blaschke and E. Quack, Phys. Rev. C **51** (1995) 2723.

[55] C.Y. Wong, E.S. Swanson and T. Barnes, Phys. Rev. C **62** (2000) 045201; Phys. Rev. C **65** (2002) 014903, Erratum C **66** (2002) 029901; C.Y. Wong, Phys. Rev. C **65** (2002) 034902; G.R.G. Burau, D.B. Blaschke and Y.L. Kalinovsky, Phys. Lett. B **506** (2001) 297; V.V. Ivanov, Y.L. Kalinovsky, D.B. Blaschke and G.R.G. Burau, hep-ph/0112354.

[56] F.S. Navarra, M. Nielsen, R.S. Marques de Carvalho and G. Krein, Phys. Lett. B **529** (2002) 87; F.O. Duraes, S.H. Lee, F.S. Navarra and M. Nielsen, Phys. Lett. B **564** (2003) 97; F.O. Duraes, H. Kim, S.H. Lee, F.S. Navarra and M. Nielsen, Phys. Rev. C **68** (2003) 035208.

[57] S.G. Matinyan and B. Müller, Phys. Rev. C **58** (1998) 2994.

[58] K.L. Haglin, Phys. Rev. C **61** (2000) 031902; Z. Lin and C.M Ko, Phys. Rev. C **62** (2000) 034903; Z. Lin and C.M. Ko, Nucl. Phys. A **715** (2003) 533; Y. Oh, T. Song and S.H. Lee, Phys. Rev. C

63 (2001) 034901; H. Kim and S.H. Lee, Eur. Phys. J. C **22** (2002) 707; W. Liu, C.M. Ko and Z. Lin, Phys. Rev. C **65** (2002) 015203; A. Sibirtsev, K. Tsushima and A.W. Thomas, Phys. Rev. **63** (2001) 044906; F.S. Navarra, M. Nielsen and M.R. Robilotta, Phys. Rev. C **64** (2001) 021901; K.L. Haglin and C. Gale, J. Phys. G **30** (2004) S375; R.S. Azevedo and M. Nielsen, Braz. J. Phys. **34** (2004) 272; R.S. Azevedo and M. Nielsen, Phys. Rev. C **69** (2004) 035201; R.S. Azevedo and M. Nielsen, nucl-th/0407080.

[59] F.S. Navarra, M. Nielsen, M.E. Bracco, M. Chiapparini and C.L. Schat, Phys. Lett. B **489** (2000) 319; F.S. Navarra, M. Nielsen, M.E. Bracco, Phys. Rev. D **65** (2002) 037502; R.D. Matheus, F.S. Navarra, M. Nielsen and R. Rodrigues da Silva, Phys. Lett. B **541** (2002) 265; M.E. Bracco, M. Chiapparini, A. Lozea, F.S. Navarra and M. Nielsen, Phys. Lett. B **521** (2001) 1; R.D. Matheus, F.S. Navarra, M. Nielsen and R. Rodrigues da Silva, hep-ph/0310280.

[60] F.O. Duraes, H. Kim, S.H. Lee, F.S. Navarra and M. Nielsen, Phys. Rev. C **68** (2003) 035208.

[61] T. Barnes, nucl-th/0306031.

[62] L. Maiani, F. Piccinini, A.D. Polosa, V. Riquer, Nucl. Phys. A **741** (2004) 273.

[63] L. Maiani, F. Piccinini, A.D. Polosa, V. Riquer, hep-ph/0408150.

[64] R. Hagedorn, Nuovo Cim. Suppl. **3** (1965) 147.

[65] A. Deandrea, N. Di Bartolomeo, R. Gatto, G. Nardulli and A.D. Polosa, Phys. Rev. D **58**, 034004 (1998); See also A.D. Polosa, "The CQM Model", Riv. Nuovo Cim. Vol. **23**, N. 11 (2000).

[66] D. Ebert, T. Feldmann, R. Friedrich and H. Reinhardt, Nucl. Phys. B **434** (1995) 619; D. Ebert, T. Feldmann and H. Reinhardt, Phys. Lett. B **388** (1996) 154.

[67] A. Deandrea, G. Nardulli and A.D. Polosa, Phys. Rev. D **68** (2003) 034002

[68] A. Manohar and H. Georgi, Nucl. Phys. B **234** (1984) 189.

[69] M.A. Ivanov, J.G. Korner and P. Santorelli, Phys. Rev. D **70** (2004) 014005.

[70] M.A. Ivanov, M.P. Locher and V.E. Lyubovitskij, Few Body Syst. **21** (1996) 131; M.A. Ivanov and V.E. Lyubovitskij, Phys. Lett. B **408** (1997) 435.

[71] M.A. Ivanov and P. Santorelli, Phys. Lett. B **456** (1999) 248; M.A. Ivanov, J.G. Körner and P. Santorelli, Phys. Rev. D **63** (2001) 074010; A. Faessler, T. Gutsche, M.A. Ivanov, J.G. Körner and V.E. Lyubovitskij, Eur. Phys. J. **C4** (2002) 18; A. Faessler, T. Gutsche, M.A. Ivanov, V.E. Lyubovitskij and P. Wang, Phys. Rev. D **68** (2003) 014011.

[72] J. Bjorken, Phys. Rev. D **27** (1983) 140.

[73] http://na50.web.cern.ch/NA50/

[74] G. Borges *et al.* (NA50 Collaboration), J. Phys. G: Nucl. Part. Phys. **30** (2004) S1351.

[75] H. Santos *et al.* (NA50 Collaboration), J. Phys. G: Nucl. Part. Phys. **30** (2004) S1175.

[76] J. Letessier and J. Rafelski, "*Hadrons and Quark Gluon Plasma*", Cambridge Monogr. Part. Phys. Nucl. Phys. Cosmol. **18** (2002).

[77] N. Cabibbo and G. Parisi, Phys. Lett. **59B** (1975) 67.

[78] J.J. Aubert *et al.*, Nucl. Phys. B **293** (1987) 740; M. Arneodo, Phys. Rep. **240** (1994) 301.

[79] V. Emel'yanov, A. Khodinov, S.R. Klein and R. Vogt, Phys. Rev. C **61** (2000) 044904.

[80] T. Kitagaki *et al.*, Phys. Lett. B **214** (1988) 281.

[81] B.L. Combridge, Nucl. Phys. B **151** (1979) 429.

[82] R.V. Gavai, D. Kharzeev, H. Satz, G. Schuler, K. Sridhar and R. Vogt, Int. J. Mod. Phys. A **10** (1995) 3043; G.A. Schuler and R. Vogt, Phys. Lett. B **387** (1996) 181.

[83] C.W. deJager, H. deVries, and C. deVries, Atomic Data and Nuclear Data Tables **14** (1974) 485.

[84] D. Kharzeev, E.M. Levin and M. Nardi, hep-ph/0212316; L. Hulthen and M. Sagawara, in *Handbüch der Physik*, **39** (1957).

[85] A.D. Martin, R.G. Roberts, and W.J. Stirling, and R.S. Thorne, Phys. Lett. B **443** (1998) 301.

[86] M. Glück, E. Reya, and A. Vogt, Z. Phys. C **53** (1992) 127.

[87] K.J. Eskola, V.J. Kolhinen and P.V. Ruuskanen, Nucl. Phys. B **535** (1998) 351.

[88] K.J. Eskola, V.J. Kolhinen and C.A. Salgado, Eur. Phys. J. C **9** (1999) 61.

[89] L. Frankfurt, V. Guzey and M. Strikman, arXiv:hep-ph/0303022.

[90] H.L. Lai *et al.*, Eur. Phys. J. C **12** (2000) 375.

[91] S.R. Klein and R. Vogt, Phys. Rev. Lett. **91** (2003) 142301.

[92] R. Vogt, Nucl. Phys. A **700** (2002) 539.

[93] H. Fujii and D. Kharzeev, Phys. Rev. D **60**, 114039 (1999)

[94] D. Kharzeev, C. Lourenço, M. Nardi and H. Satz, Z. Phys. C **74**, 307 (1997)

[95] M. Gazdzicki and M. I. Gorenstein, Phys. Rev. Lett. **83**, 4009 (1999) [arXiv:hep-ph/9905515].

[96] P. Braun-Munzinger and J. Stachel, Phys. Lett. B **490**, 196 (2000) [arXiv:nucl-th/0007059].

[97] M. I. Gorenstein, A. P. Kostyuk, H. Stöcker and W. Greiner, Phys. Lett. B **509**, 277 (2001) [arXiv:hep-ph/0010148].

[98] A. P. Kostyuk, M. I. Gorenstein, H. Stocker and W. Greiner, Phys. Lett. B **531**, 195 (2002) [arXiv:hep-ph/0110269].

[99] A. Andronic, P. Braun-Munzinger, K. Redlich and J. Stachel, Phys. Lett. B **571**, 36 (2003) [arXiv:nucl-th/0303036].

[100] P. Braun-Munzinger, K. Redlich and J. Stachel, arXiv:nucl-th/0304013.

[101] M. C. Abreu *et al.* [NA50 Collaboration], Phys. Lett. B **450**, 456 (1999).

[102] M. C. Abreu *et al.* [NA50 Collaboration], Phys. Lett. B **477**, 28 (2000).

[103] H. Santos *et al.* [NA50 Collaboration], J. Phys. G **30**, S1175 (2004) [arXiv:hep-ex/0405056].

[104] L. Grandchamp and R. Rapp, Phys. Lett. B **523**, 60 (2001) [arXiv:hep-ph/0103124].

[105] L. Grandchamp and R. Rapp, Nucl. Phys. A **709**, 415 (2002) [arXiv:hep-ph/0205305].

[106] J. Adams *et al.* [STAR Collaboration], arXiv:nucl-ex/0407006.

[107] S. S. Adler *et al.* [PHENIX Collaboration], arXiv:nucl-ex/0409028.

[108] L. Grandchamp, R. Rapp and G. E. Brown, Phys. Rev. Lett. **92**, 212301 (2004) [arXiv:hep-ph/0306077].

[109] R. L. Thews, arXiv:hep-ph/0206179.

[110] V. Greco, C. M. Ko and R. Rapp, Phys. Lett. B **595**, 202 (2004) [arXiv:nucl-th/0312100].

[111] B. Zhang, C. M. Ko, B. A. Li, Z. W. Lin and S. Pal, Phys. Rev. C **65**, 054909 (2002) [arXiv:nucl-th/0201038].

[112] E. L. Bratkovskaya, W. Cassing and H. Stocker, Phys. Rev. C **67**, 054905 (2003) [arXiv:nucl-th/0301083].

[113] C. Baglin *et al.* (NA38 Collaboration), Phys. Lett. B **220** (1989)471.

[114] C. Baglin *et al.* (NA38 Collaboration), Phys. Lett. B **255** (1991)459.

[115] M.C. Abreu *et al.* (NA38 Collaboration), Phys. Lett. B **449** (1999) 128.

[116] M.C. Abreu *et al.* (NA38 Collaboration), Phys. Lett. B **466** (1999) 408.

[117] M.C. Abreu *et al.* (NA50 Collaboration), Phys. Lett. B **410** (1997) 327.

[118] M.C. Abreu *et al.* (NA50 Collaboration), Phys. Lett. B **410** (1997) 337.

[119] M.C. Abreu *et al.* (NA50 Collaboration), Phys. Lett. B **477** (2000) 28.

[120] M.C. Abreu *et al.* (NA50 Collaboration), Phys. Lett. B **521** (2001) 195.

[121] M.C. Abreu *et al.* (NA51 Collaboration), Phys. Lett. B **438** (1998) 35.

[122] M.C. Abreu *et al.* (NA38 Collaboration), Phys. Lett. B **444** (1998) 516.

[123] M.C. Abreu *et al.* (NA50 Collaboration), Phys. Lett. B **553** (2003) 167.

[124] B. Alessandro *et al.* (NA50 Collaboration), Eur. Phys. J. C **33** (2004) 31.

[125] R. Vogt, Phys. Rep. **310** (1999) 197.

[126] R.J. Glauber, *Lectures in Theoretical Physics*, NY, 1959, Vol. 1, 315.

[127] C.W. de Jager *et al.*, Atomic Data and Nuclear Data Tables 14(1974) 479.

[128] S. S. Adler *et al.* [PHENIX Collaboration], Phys. Rev. Lett. **92**, 051802 (2004)

[129] R. G. de Cassagnac [PHENIX Collaboration], J. Phys. G **30**, S1341 (2004)

[130] S. S. Adler *et al.* [PHENIX Collaboration], Phys. Rev. C **69**, 014901 (2004)

[131] K. Adcox *et al.* [PHENIX Collaboration], Nucl. Instrum. Meth. A **499**, 469 (2003).

[132] Particle Data Group, Phys. Rev. D **66**, 010001 (2002)

[133] S. R. Klein and R. Vogt, Phys. Rev. Lett. **91**, 142301 (2003)

[134] B. Kopeliovich, A. Tarasov and J. Hufner, Nucl. Phys. A **696**, 669 (2001)

[135] R. L. Thews, M. Schroedter and J. Rafelski, Phys. Rev. C **63**, 054905 (2001)

[136] S. Klein and J. Nystrand, Phys. Rev. Lett. **92**, 142003 (2004)

[137] S. Klein and J. Nystrand, Phys. Rev. C **60**, 014903 (1999); A. J. Baltz, S. R. Klein and J. Nystrand, Phys. Rev. Lett. **89**, 012301 (2002)

[138] M. Drees and D. Zeppenfeld, Phys. Rev. D **39**, 2536 (1989).

[139] B. A. Kniehl, Phys. Lett. B **254**, 267 (1991).

[140] J. Ohnemus, T. F. Walsh and P. M. Zerwas, Phys. Lett. B **328**, 369 (1994).

[141] G. Baur *et al.*, Phys. Rep. **364**, 359 (2002).

[142] M. G. Ryskin, Z. Phys. C **57**, 89 (1993).

[143] L. L. Frankfurt, M. F. McDermott and M. Strikman, JHEP **9902**, 002 (1999).

[144] A. D. Martin, M. G. Ryskin and T. Teubner, Phys. Lett. B **454**, 339 (1999).

[145] J. A. Crittenden, *Exclusive Production of Neutral Vector Mesons at the Electron-Proton Collider HERA*, Springer-Verlag, 1997.

[146] C. Adloff *et al.* [H1 Collaboration], Phys. Lett. B **483**, 23 (2000).

[147] J. Breitweg *et al.* [ZEUS Collaboration], Phys. Lett. B **437**, 432 (1998).

[148] L. Frankfurt, M. Strikman and M.Zhalov, Phys. Lett. **B540**, 220 (2002).

[149] C. Adler *et al.* [STAR Collaboration], Phys. Rev. Lett. **89**, 272302 (2002).

[150] V. A. Khoze, A. D. Martin and M. G. Ryskin, Eur. Phys. J. C **24**, 459 (2002).

[151] L. Frankfurt, V. Guzey, M. Strikman and M. Zhalov, JHEP **0308**, 043 (2003).

[152] Angela Wyatt, presented at “Small-x and Diffraction 2003,” Sept. 17-20, 2003, Fermilab, IL. Transparencies are available at http://conferences.fnal.gov/smallx/new_program.htm.

[153] S. Klein and J. Nystrand, hep-ph/0310223, presented at “Small-x and Diffraction 2003,” Sept. 17-20, 2003, Fermilab, IL.

[154] F. Abe *et al.* [CDF Collaboration], Phys. Rev. Lett. **75**, 4358 (1995).

[155] S. R. Klein and J. Nystrand, Phys. Rev. Lett. **84**, 2330 (2000); Phys. Lett. A **308**, 323 (2003).

[156] S. Klein (STAR Collaboration), nucl-ex/0310020.

[157] N. Baron and G. Baur, Phys. Rev. C **48**, 1999 (1993); M. Greiner *et al.*, Phys. Rev. C **51**, 911 (1995); S. Klein, J. Nystrand and R. Vogt, Phys. Rev. C **60**, 044906; S. R. Klein, J. Nystrand and R. Vogt, Eur. Phys. J. C **21**, 563 (2001).